

12-2010

## Retrieval of Aerosol Mass Concentration from Elastic Lidar Data

Christian C. Marchant  
*Utah State University*

Follow this and additional works at: <https://digitalcommons.usu.edu/etd>



Part of the Environmental Engineering Commons

---

### Recommended Citation

Marchant, Christian C., "Retrieval of Aerosol Mass Concentration from Elastic Lidar Data" (2010). All Graduate Theses and Dissertations. 812.  
<https://digitalcommons.usu.edu/etd/812>

This Dissertation is brought to you for free and open access by the Graduate Studies at DigitalCommons@USU. It has been accepted for inclusion in All Graduate Theses and Dissertations by an authorized administrator of DigitalCommons@USU. For more information, please contact [digitalcommons@usu.edu](mailto:digitalcommons@usu.edu).



RETRIEVAL OF AEROSOL MASS CONCENTRATION FROM ELASTIC LIDAR  
DATA

by

Christian C. Marchant

A dissertation submitted in partial fulfillment  
of the requirements for the degree

of

DOCTOR OF PHILOSOPHY

in

Electrical Engineering

Approved:

---

Dr. Todd K. Moon  
Major Professor

---

Dr. Jacob H. Gunther  
Committee Member

---

Dr. Scott E. Budge  
Committee Member

---

Dr. Vladimir V. Zavyalov  
Committee Member

---

Dr. Gail E. Bingham  
Committee Member

---

Dr. Byron R. Burnham  
Dean of Graduate Studies

UTAH STATE UNIVERSITY  
Logan, Utah

2010

Copyright © Christian C. Marchant 2010

All Rights Reserved

## Abstract

Retrieval of Aerosol Mass Concentration from Elastic Lidar Data

by

Christian C. Marchant, Doctor of Philosophy

Utah State University, 2010

Major Professor: Dr. Todd K. Moon

Department: Electrical and Computer Engineering

Agricultural aerosol sources can contribute significantly to air pollution in many regions of the country. Characterization of the aerosol emissions of agricultural operations is required to establish a scientific basis for crafting regulations concerning agricultural aerosols. A new lidar instrument for measuring aerosol emissions is described, as well as two new algorithms for converting lidar measurements into aerosol concentration data. The average daily aerosol emission rate is estimated from a dairy using lidar.

The Aglite Lidar is a portable scanning lidar for mapping the concentration of particulate matter from agricultural and other sources. The instrument is described and performance and lidar sensitivity data are presented. Its ability to map aerosol plumes is demonstrated, as well as the ability to extract wind-speed information from the lidar data.

An iterative least-squares method is presented for estimating the solution to the lidar equation. The method requires *a priori* knowledge of aerosol relationships from point sensors. The lidar equation is formulated and solved in vector form. The solution is stable for signals with extremely low signal-to-noise ratios and for signals at ranges far beyond the boundary point.

Another lidar algorithm is also presented as part of a technique for estimating aerosol concentration and particle-size distribution. This technique uses a form of the extended

Kalman filter, wherein the target aerosol is represented as a linear combination of basis-aerosols. For both algorithms, the algorithm is demonstrated using both synthetic test data and field measurements of biological aerosol simulants. The estimated particle size distribution allows straightforward calculation of parameters such as volume-fraction concentration and effective radius.

Particulate matter emission rates from a dairy in the San Joaquin Valley of California were investigated during June 2008. Vertical particulate matter concentration profiles were measured both upwind and downwind of the facility using lidar, and a mass balance technique was used to estimate the average emission rate. Emission rates were also estimated using an inverse modeling technique coupled with the filter-based measurements. The concentrations measured by lidar and inverse modeling are of similar magnitude to each other, as well as to those from studies with similar conditions.

(158 pages)

To my wonderful wife....

## Acknowledgments

I would like to acknowledge the invaluable guidance of Drs. Gail Bingham, Vladimir Zavyalov, Thomas Wilkerson, Randal Martin, and Michael Wojcik, whose support was essential in performing this research. This dissertation is a product of the Aglite program of the Energy Dynamics Laboratory, part of the Utah State University Research Foundation, under USDA Agreement number 58-3625-4-121 with Dr. Jerry Hatfield, the director of the National Soil Tilth Laboratory in Ames, Iowa, who provided valuable direction to the Aglite development team, along with Richard Pfeiffer and John Prueger. Any opinions, findings, conclusions, or recommendations expressed in this publication are those of the authors and do not necessarily reflect the view of the USDA.

I would further like to thank the faculty of the USU Department of Electrical and Computer Engineering. In particular, I would like to recognize my advisor, Dr. Todd Moon, as well as Drs. Jacob Gunther and Scott Budge. They provided much valuable education and advice to me in my educational career and in the completion of this dissertation. It would be ungrateful not to mention the contributions given by my colleagues Kori Moore, Doug Ahlstrom, William Bradford, Derek Jones, Tanner Jones, Richard Larsen, Jan Marie Andersen, Cordell Wright, and Scott Cornelsen.

Finally, I must extend deserved recognition to my family, and in particular my loving wife, for their encouragement and support. Without them, this dissertation would not have been possible. My parents have provided me with valuable advice and support, and I am so grateful for my loving wife, Hanna. I am entirely dependent on her support and patience.

Christian C. Marchant

## Contents

	Page
<b>Abstract</b> . . . . .	<b>iii</b>
<b>Acknowledgments</b> . . . . .	<b>vi</b>
<b>List of Tables</b> . . . . .	<b>ix</b>
<b>List of Figures</b> . . . . .	<b>x</b>
<b>Acronyms</b> . . . . .	<b>xii</b>
<b>1 Introduction</b> . . . . .	<b>1</b>
1.1 Project Background and Relevance . . . . .	1
1.2 Literature Survey . . . . .	3
1.3 Research Overview . . . . .	10
References . . . . .	14
<b>2 Aglite Description and Operation</b> . . . . .	<b>19</b>
2.1 Application . . . . .	19
2.2 Aglite Lidar Description . . . . .	21
2.2.1 Hardware Design . . . . .	22
2.2.2 Eye-Safety . . . . .	26
2.3 Lidar Data and Calibration . . . . .	28
2.4 Example Data and Discussion . . . . .	32
2.4.1 Aerosol Detection Capability . . . . .	32
2.4.2 Fixed Direction Lidar Measurement . . . . .	34
2.4.3 Crosswind Scans for Aerosol Flux Measurements . . . . .	35
2.5 Aerosol Traced Wind Motion . . . . .	36
2.5.1 Wind Velocity from Lidar “Stares” . . . . .	36
2.5.2 Vertical Scans for Cross-Sections of Moving Plumes . . . . .	38
2.6 Conclusion . . . . .	41
References . . . . .	43
<b>3 An Iterative Least Square Approach to Elastic-Lidar Retrievals for Well-Characterized Aerosols</b> . . . . .	<b>48</b>
3.1 Background . . . . .	48
3.2 Well Characterized Local Aerosol . . . . .	53
3.3 State Vector Formulation . . . . .	57
3.4 Linearization . . . . .	59
3.5 Laser Pulse Shape and Geometric Form Factor . . . . .	64
3.6 Solution Error . . . . .	66
3.7 Simulations . . . . .	68

3.7.1	Background Retrieval . . . . .	70
3.7.2	Plume Retrieval . . . . .	71
3.8	Experimental Data . . . . .	73
3.9	Conclusion . . . . .	77
	References . . . . .	79
<b>4</b>	<b>Estimation of Aerosol Effective Radius by Multi-Wavelength Elastic Lidar . . . . .</b>	<b>81</b>
4.1	Background . . . . .	81
4.2	EKF Formulation . . . . .	82
4.2.1	Forward Model . . . . .	82
4.2.2	State-Space Signal Model . . . . .	84
4.2.3	State-Vector Augmentation . . . . .	87
4.3	Simulation . . . . .	89
4.4	Experimental Measurements . . . . .	94
	References . . . . .	99
<b>5</b>	<b>Estimation of Dairy PM Emission Rates by Lidar and Inverse Modeling</b>	<b>101</b>
5.1	Application . . . . .	101
5.2	Methodology . . . . .	102
5.2.1	Site Description . . . . .	103
5.2.2	Setup . . . . .	104
5.2.3	Inverse Modeling . . . . .	106
5.2.4	Elastic Lidar . . . . .	108
5.3	Measurements . . . . .	111
5.3.1	Point Samplers . . . . .	111
5.3.2	Aglite Measurements . . . . .	112
5.3.3	Calculated Emission Rates . . . . .	113
5.4	Conclusion . . . . .	115
	References . . . . .	117
<b>6</b>	<b>Concluding Remarks . . . . .</b>	<b>119</b>
6.1	Elastic Lidar Applications . . . . .	119
6.2	Lidar Design Tradeoffs . . . . .	120
6.3	Wavelength and Component Aerosol Selection . . . . .	121
6.4	Information Retrieval from Lidar Returns . . . . .	122
6.5	Research Context . . . . .	123
6.6	Future Work . . . . .	124
<b>Appendices . . . . .</b>	<b>126</b>	
Appendix A	Construction of Lidar Equation Matrices . . . . .	127
Appendix B	Derivation of Covariance Matrices . . . . .	130
Appendix C	Publication Release Forms . . . . .	133
<b>Vita . . . . .</b>	<b>146</b>	

## List of Tables

Table	Page
2.1 Aglite lidar system parameters. . . . .	27
2.2 Representative eye-safety distances for Aglite lidar. . . . .	28
3.1 Aerosol optical and mass characteristics. . . . .	70
3.2 Average retrieval error comparison. . . . .	73
4.1 Simulant properties and conditions. . . . .	96
5.1 Average calculated mass conversion factors ( $\pm 95\%$ CI) for each measurement period, June 2008. . . . .	113
5.2 Average temperature, wind velocity, estimated emission rates, and $\pm 95\%$ confidence interval (g/day/AU) for each period, estimated by inverse modeling and lidar. . . . .	115
5.3 Emission rates estimated by inverse modeling, lidar measurements, and previous studies. . . . .	117

## List of Figures

Figure	Page
2.1 Aglite lidar instrument in deployment configuration. . . . .	23
2.2 Aglite lidar conceptual arrangement and layout of optical bench components. . . . .	23
2.3 Aglite geometric form factor as a function of range. . . . .	30
2.4 Example return power signal and signal variance from Aglite. . . . .	31
2.5 Two examples of SNR values observed by Aglite under field conditions. . . . .	31
2.6 Typical “stare” image of range-normalized IR channel intensity. . . . .	33
2.7 Example retrieval showing measured signal, estimated backscatter, mode radius, and PM <sub>10</sub> concentration. . . . .	35
2.8 Examples of typical horizontal and staple scans by Aglite. . . . .	37
2.9 Local wind patterns shown in a time series of lidar returns at different ranges. . . . .	39
2.10 Returns from an 8-minute horizontal stare at 20 m height during light and variable wind conditions. . . . .	39
2.11 Series of 30-second vertical scans showing the movement of plumes toward the lidar. . . . .	40
2.12 Distortion of the aerosol image due to simultaneous motion of wind and lidar scan. . . . .	42
2.13 Wind-blown plumes of clay dust in Nevada. . . . .	42
3.1 Illustration of Aglite measuring an atmosphere that consists of a baseline component plus a mixture of varying components. . . . .	51
3.2 Comparison of synthesized data with the estimated solution for measured power (left column) and PM <sub>10</sub> concentration (right column) of (a,b) average continental, (c,d) polluted continental, and (e,f) urban type homogeneous atmospheres. . . . .	62
3.3 Flowchart illustrating the operation of the iterative least-squares method. . . . .	63

3.4	(a) Laser pulse shape convolved with the integration window, and (b) its frequency response. . . . .	66
3.5	Estimated PM <sub>10</sub> mean concentration and standard deviation compared to actual values for synthesized data representing (a,b) average continental, (c,d) polluted continental, (e,f) and urban type plumes. . . . .	72
3.6	Estimated values for (a,b) returned power, (c,d) emission component amplitude, and (e,f) PM concentration from swine facility measurement, assuming one component aerosol (left column) and two component aerosols (right column). . . . .	76
3.7	Comparison of the stability of estimated PM <sub>10</sub> concentration from the NLS and Klett methods under the conditions of (a) 25% error in the boundary point backscatter coefficients, and (b) 50% error in the baseline extinction values. . . . .	78
4.1	Backscatter coefficients of a (a) single-component, and (b) two-component aerosol as a function of range. (c) The particle volume distributions of the two components. . . . .	91
4.2	Illustration of the performance of an EKF filter on a synthetic data set, including (a) the estimated returned power, (b) SNR, (c) component amplitude, (d) retrieved component bias, (e) volume concentration, and (f) effective radius. . . . .	93
4.3	Images of the estimated (a) PM <sub>10</sub> volume-fraction concentration, and (b) effective radius for the MS2 simulant. . . . .	97
4.4	Measured (symbols) and estimated (lines) average return power and estimated effective radius for (a,b) Btk, (c,d) ARD, and (e,f) MS2 type simulants. . . . .	98
5.1	Map of instrumentation locations. . . . .	107
5.2	Average PM <sub>10</sub> concentration ( $\mu\text{g}/\text{m}^3$ ) of (a) a vertical scan measured by lidar at 94 and 98 degrees azimuth, and (b) a horizontal map estimated by AERMOD, overlaid on the dairy footprint. . . . .	114

## Acronyms

AERMOD	American Meteorological Society Regulatory Model
APD	avalanche photo-diode
AU	animal unit
CMP	conservation management practice
EKF	extended Kalman filter
EKS	extended Kalman smoother
EPA	Environmental Protection Agency
FOV	field of view
GFF	geometric form factor
IR	infrared lidar channel (1064 nm)
ISCST3	Industrial Source Complex Short Term Model, Ver. 3
MCF	mass conversion factor
NAAQS	national ambient air quality standards
ND	neutral density
NLS	nonlinear least squares
OPC	optical particle counter
PM	particulate matter
PMT	photo-multiplier tube
PSD	particle-size distribution
PST	Pacific Standard Time
SNR	signal-to-noise ratio
TSP	total suspended particulate
UDP	user datagram protocol
USDA	United States Department of Agriculture
UV	ultra-violet lidar channel (355 nm)
V	visible lidar channel (532 nm)

# Chapter 1

## Introduction

### 1.1 Project Background and Relevance

The impact of agricultural operations on air-quality is a subject of interest to society and an area of active research. Economic growth, increased demand for food and energy, and the movement of urban populations into rural areas have resulted in increasing exposure of people to emissions from these operations, which generate aerosols that impact both the environment and human health.

Elastic lidar operates using the radar principle to detect Rayleigh and Mie scattering from atmospheric gas and aerosols. These types of scattering are characterized by the deflection of a photon by a gas molecule or dust particle in an elastic collision, meaning that the energy of the photon is conserved. It has the ability to map aerosol concentration in the atmosphere and to determine aerosol particle size [1]. This makes lidar an enormously useful tool for investigating air-quality, both generally and in the context of agricultural operations in particular. In fact, the use of lidar to map particulate matter (PM) concentration and estimate aerosol emission rates from an agricultural facility has been demonstrated previously, and lidar has been proven to be a versatile tool for investigating atmospheric aerosols and a useful means of characterizing and monitoring the air-quality impact of industrial and agricultural operations [2].

This dissertation is generated as part of the Ag program of the Energy Dynamics Laboratory of the Utah State University Research Foundation, whose mission is to measure the air-quality impact of industrial and agricultural facilities. The Ag program uses the portable Aglite lidar with supporting instruments for mapping aerosol concentration from agricultural sources.

This dissertation includes four papers, two of which have already been peer-reviewed

and published, and the other two have been submitted for publication. Chapter 2 comes from “Aglite Lidar: A Portable Elastic Lidar System for Investigating Aerosol and Wind Motions at or Around Agricultural Production Facilities” [3], which describes the hardware and operational procedure of the Aglite instrument, as well as demonstrating its application to measuring wind speed by tracking dust plume movement and image morphology. My specific contributions to this paper included writing the majority of the text, performing the software modeling of the expected performance of the instrument the development, and coding the retrieval algorithm based on Klett’s method. In addition, I developed the process for calibrating lidar signals using point sensors, assisted in the data collection, and performed all of the data processing.

Chapter 3 comes from “An Iterative Least Square Approach to Elastic-Lidar Retrievals for Well-Characterized Aerosols” [4]. This paper describes the minimum least-squares algorithm outlined above, and demonstrates its performance using both synthetic and experimental data. In addition to writing nearly all of the text of the paper, my contributions included developing the method of representing an aerosol as a linear combination of basis aerosols, applying Newton’s method to iteratively linearize and solve the lidar equation, and incorporating image-restoration into the retrieval process. Additionally, I wrote the software code to implement the algorithm, created the synthetic data used to verify it, and performed all of the data processing.

Chapter 4 has been submitted for publication by the journal *IEEE Transactions on Geoscience and Remote Sensing* as “Estimation of Aerosol Effective Radius by Multi-Wavelength Elastic Lidar,” which describes a novel form of the extended Kalman filter (EKF) estimator, where the filter is applied to the lidar signal over range and directly estimates lidar concentration, whereas other lidar EKF estimators were applied over time and only retrieved optical coefficients. The algorithm uses an augmented state vector, making it a type of EKF called an extended Kalman smoother (EKS). It also demonstrates the estimation of effective particle radius from an aerosol release experiment at Dugway Proving Grounds [5]. I also wrote nearly all of the text in this paper and my other contributions

included the formulation of the extended Kalman filter as applied to lidar data and the development of a systematic method for forming basis aerosols. Additionally, I wrote the software code to implement the algorithm, created the synthetic data used to verify it, and performed all of the data processing.

Chapter 5 has been submitted for publication by the journal *Transactions of the ASABE* as “Estimation of Dairy Particulate Matter Emission Rates by LIDAR and Inverse Modeling,” and describes the application of the EKS lidar retrieval method to estimate the PM<sub>10</sub> emission rate from a dairy facility [6]. This paper demonstrates the first application of lidar to estimate aerosol emissions from a dairy and adds to the very small set of existing baseline data on dairy aerosol emission rates in the literature. My specific contributions to this paper included writing the majority of the text, processing all of the lidar data, and assisting in developing the algorithm used by the software models for estimating emission rates.

## 1.2 Literature Survey

The most common early use of lidar for meteorological purposes was to measure cloud and vertical aerosol profiles of the atmosphere. Early examples of applying the optical radar principle to meteorological measurements used pulses of incoherent white light to measure cloud heights as early as 1938 [7, 8]. The development of lidar, or laser radar, shortly followed the invention of the Q-switched laser in 1962 [9]. The first use of a laser transmitter, with its highly collimated beam, narrow spectral bandwidth, and narrow temporal pulse width, enabled a dramatic increase in sensitivity and resolution. The initial application of lidar to meteorological measurements was performed by Fiocco and Smullin in 1963 to investigate aerosol layers in the upper stratosphere [10]. Other work by Fiocco investigated residual stratospheric aerosol from meteors, and the upper boundary layer of the troposphere [11, 12]. Important early work was also performed by Collis, and included probing clouds, stratospheric aerosol layers, mapping dust plume morphology generated by subterranean nuclear detonations, and studying waves in the lower troposphere aerosol boundary layer [13–16]. Collis also published an important early paper outlining the

new emerging field of lidar and demonstrating the earliest analytical technique: the slope method [17].

Early applications of elastic lidar to the problem of air quality used lidar to validate parametric emission models by mapping emission plume size and height, including work by Hamilton to capture vertical profiles of emissions from power plant smokestacks. Whereas earlier work in probing the atmosphere with lidar normally used a stationary 90 degree vertical stare, this work used a vertical scan composed of a series of measurements at varying elevation angles, enabling the lidar to capture the morphology of an emission plume in a 2-D cross-section. The measured height of the plume was used to verify predictions of a parametric model of the emission process [18, 19]. Hamilton also described the use of a remarkable real-time 2-D analog display of these vertical scans of the emission profile intensity in 1969 [20]. Barrett and Ben-Dov used lidar to probe atmospheric pollutants, including a smoke plume and smog layer, and notably demonstrated the retrieval of quantitative particulate mass concentration values from this data [21]. Johnson demonstrated the measurement of morphology and dynamics of emission plumes from a smokestack [22, 23].

As pointed out by Reagan, lidar's potential is greatest when used in conjunction with supplemental instruments, such as point sensors [24]. These instruments can be used both to calibrate the lidar and to constrain estimates made using lidar data, enabling quantitative analysis of lidar data. Fernald demonstrated the use of coincident data from a solar radiometer in the form of total optical thickness to constrain the analysis of lidar data and retrieve both backscatter and extinction coefficients from a single channel [25]. Grams demonstrated a method for retrieving complex index of refraction from vertical profile lidar measurements of ash in the atmosphere by constraining it with independent measurements of particle size distribution (PSD), which was measured using a jet impactor to collect particles onto microscope slides, which were analyzed using a micro-photographic technique [26, 27]. Reagan performed a comparison of aerosol mass concentration measurements between an ordinary monostatic elastic lidar, a bistatic elastic lidar, and in-situ instruments mounted on an aircraft. The measurements from the monostatic lidar were constrained using data from

the bistatic lidar and a solar radiometer. The estimated aerosol mass concentration from the monostatic lidar data was compared with simultaneously measured in-situ data from an aircraft, whose instruments included an optical particle counter (OPC), an integrating nephelometer, a particle mass monitor, a condensation nucleus counter, and a cascade impactor [28].

An elastic lidar can also be significantly enhanced through the addition of a non-elastic Raman scattering channel. A Raman channel enables independent measurement of extinction alone, which can then be used as *a priori* information for retrieving backscatter values from the elastic channel [29]. Bistatic and multiple-field-of-view lidars are also able to give more information than a standard monostatic elastic lidar by measuring aerosol sidescatter in addition to backscatter [30, 31].

Lidar has also been applied specifically to investigating agricultural activities. Cooper used a Raman lidar capable of measuring spatially coherent water vapor structures in order to investigate the mass-energy exchange between the ground and the atmosphere over the canopy of an orchard [32]. Stoughton used an elastic lidar to map the dispersion of pesticide applied by an airplane over a section of forest, with both horizontal and vertical lidar scanning patterns. These lidar measurements tracked the drift range of the pesticide plumes and were used to verify the accuracy of two different parametric spray drift models [33]. Holmén demonstrated the measurement of mass concentration values of emissions from tillage activities. This lidar data was compared with mass concentration values measured by point samplers in order to verify plume height and dispersion coefficients from a parametric model [34–36]. Hiscox also demonstrated the use of an elastic lidar to map particulate mass concentration from tillage activities, and compared them with mass concentration measurements from point-sensors [37]. Eichinger used an elastic lidar to estimate heat flux emitted from crop-fields by measuring the height and width of the entrainment zone, the boundary layer between aerosols near the surface of the ground and cleaner air above. These estimates were input into a boundary layer model, which generated an estimate of surface heat flux [38].

Initial techniques for quantitative analysis of lidar data focused on retrieving the aerosol optical properties of backscatter and extinction. This is a difficult problem both because the equation describing an elastic lidar signal is nonlinear and also because the problem is ill-posed; two optical coefficients must be estimated for every single channel. Many of these techniques employed for processing lidar data are analytical in nature, attempting to solve the partial differential form of the lidar equation. There are also some examples of algorithms for analyzing lidar data from an optimization perspective. The task of quantitative analysis of lidar data is complicated by the difficulty in achieving accurate absolute calibration of a lidar instrument. Many early attempts at quantitative analysis relied on representing the lidar signal as relative backscatter magnitude by range-correcting the observed signal and normalizing by its minimum value [14]. If the following assumptions are satisfied, that the minimum value corresponds to a section of the atmosphere with negligible aerosol scattering, and if the extinction in the other portions of the signal are also negligible (i.e. optically thin), then a measured range-corrected signal is proportional to the ratio of backscatter from aerosols to backscatter from atmospheric gases. In this case, the supposedly pure section of atmosphere essentially calibrates the lidar signal. Barrett extended this method to estimating aerosol mass concentration by assuming a PSD for the aerosol and numerically calculating a linear relationship between backscatter and mass concentration [21]. Collis proposed the slope method, an analytical method for measuring extinction without calibrating the lidar signal [17]. This method relies on the assumption that the atmosphere is homogeneous over some range. In this case, the slope of the logarithmic range-corrected returned power is determined by the extinction coefficient of the atmosphere. Another related method of analyzing lidar signals is the slant method proposed by Sandford [39]. This method assumes that the backscatter and extinction coefficients of the atmosphere are constant at any given height. The lidar takes a series of measurements at different pointing elevation angles, and uses the measured power from a given height as a function of angle to determine the extinction coefficient at that height. Methods were also proposed that relied on *a priori* estimates of extinction, either as a function of range [40] or of total transmittance [41].

There is a group of analytical solutions for retrieving backscatter as a function of range from the lidar signal that rely on the partial differential equation form of the lidar equation, which is of the same form as the Bernoulli equation [25, 42–46]. These methods all have similar analytical form and rely on a known fixed relationship between extinction and backscatter, as well as a calibration point, which is the boundary condition at some range where the extinction value is known. These analytical solutions are the most popular means of retrieving extinction and backscatter from lidar data, and most techniques in use today for quantitative analysis of lidar data use them as an intermediate step, after which further algorithms are used to convert backscatter and extinction coefficients of an aerosol to its PSD. The analytical solution has two serious drawbacks. First, it has a pole located on the far side of the calibration point, which makes the solution unstable at far ranges. Second, the method has no means of accounting for noise in the signal when calculating the solution.

Although less popular than analytical methods, algorithms based on the principle of optimization have also been proposed. The minimum cross-entropy method is an important and under-recognized method proposed by Yee for estimating extinction coefficients [47]. This method uses the ellipsoid algorithm, an iterative optimization algorithm that seeks to calculate the minimum norm solution that corresponds to a lidar signal within a given distance of the measured signal. Several algorithms have been proposed that are forms of the EKF. Rocadenbosch proposed a formulation of the EKF that estimates both extinction and backscatter coefficients as a function of range using a single channel [48, 49]. The state vector consists of down-sampled backscatter and extinction coefficients, allowing the algorithm to trade spatial resolution for the ability to independently recover both backscatter and extinction from a single channel. For this formulation, the state vector represents the state of the atmosphere over all measured range values at any given time and the computational cost of propagating the state vector can become quite large. Dias proposed a form of the extended Kalman smoother that describes the lidar signal using a semi-causal filter [50]. The state vector propagates over range and is composed of only a small number of extinction and optical thickness coefficients of neighboring data points. An algorithm was also proposed

by Warren for use with multi-wavelength lidar data that consists of two estimators coupled together. The first is a Kalman filter for estimating particle concentration, whose output is fed into a maximum-likelihood estimator of backscatter coefficients [51].

A lidar retrieval algorithm is typically used to retrieve the intermediate values of extinction and backscatter. However, often the parameter of interest is the PSD of the aerosol or other parameters that can be derived from it, such as mass concentration or mode radius. Much work has been done to demonstrate methods of estimating PSDs from multi-wavelength backscatter and extinction data. A simple method for discriminating aerosol types from multiple backscatter channels was demonstrated by Sasano [52]. A power-law relationship is assumed between the backscatter values of the different channels. The exponent parameter is measured from lidar data and compared to a pre-computed table of known aerosols. Retrieval of the PSD has also been demonstrated by assuming the PSD is of a known form, i.e. a power-law distribution or a log-normal distribution, and estimating the parameters of the distribution [53–55].

More sophisticated techniques for estimating the PSD from multi-wavelength measurements of an unknown aerosol involve approximating it as a linear combination of component functions. Heintzenberg proposed an iterative least-square estimator that represented the PSD as a discrete set of rectangle functions and approximates the measured optical properties as linear combinations of the particle size distribution component functions [56]. It calculates the optimal amplitude of each individual component function one at a time, while using a condition check to enforce constraints of smoothness and non-negativity. This allows it to estimate a PSD function using a greater number of components than measured channels. Qing suggested a similar approach that uses smoother B-spline functions instead of the rectangle component functions [57]. Significantly, he also suggested minimizing a cost function that included a Lagrange multiplier with a smoothing matrix. Donovan proposed choosing the component functions of the PSD as orthogonal functions determined using principal component analysis [58]. He also proposed that since the PSD could be calculated as a linear function of measured optical coefficients, parameters such as total volume or

surface area concentration could be calculated directly as linear functions of the optical coefficients, which he demonstrated using data from a 4 channel lidar, including one Raman channel. Böckmann proposed a retrieval method that uses B-spline component functions and projection onto a subspace by means of truncated singular value decomposition in order to estimate a smooth PSD using only four channels [59].

There are important deficiencies in the previously demonstrated algorithms for converting lidar data into aerosol concentration and estimating aerosol size concentration. Many of these algorithms, including the popular Klett method [44, 46], give unstable results and in general these methods fail to perform adequately under low signal-to-noise ratio (SNR) conditions or under conditions of significant calibration error, which are common under field conditions.

With lidar, there is an inherent trade-off between both the spatial and temporal resolution and the SNR of a measurement. At the same time, due to the range-squared falloff of a lidar signal, it is difficult to construct a lidar instrument that can measure over a wide span of range values at good SNR levels. As a result of these limitations, there is naturally a strong desire by lidar operators to operate in a low SNR regime, either to increase the resolution of a measurement or to extend the range over which data can be collected. The algorithms described in this dissertation allow the retrieval of aerosol concentration from lidar measurements with low SNR values, which in turn enables the instrument to scan the atmosphere at a much higher sample rate and over greater distances than would be otherwise possible.

Aglite is regularly used under novel and non-ideal conditions, as often occur during field campaigns. In previous work mapping aerosol concentration with Aglite, it was found that existing elastic lidar retrieval algorithms were not sufficiently robust under these conditions. This motivated the development of new algorithms for retrievals. Aglite has been used to measure emission rates from various agricultural operations, and to compare the effectiveness of conservation practices.

### 1.3 Research Overview

This dissertation presents two novel algorithms. Previous algorithms only estimate optical coefficients and have had unstable performance under low SNR conditions. In addition to optical coefficients, the new algorithms are able to estimate aerosol PSD and give stable results under low SNR conditions. They estimate both the PSD and concentration of aerosols from elastic lidar data. This dissertation also describes the estimation of aerosol emission rates from an entire dairy facility using lidar, which has never been done before. In connection with this, it also presents a description of the Aglite lidar and other supporting instruments, the procedure for using them to make measurements, and example results of mapping aerosols and estimating net emission rates from a facility.

The ability of the techniques to generate accurate estimates has been verified using computer-generated data. Additionally, the performance of the techniques on real data has been demonstrated using measurements from field campaigns. Finally, estimation of aerosol emission rates from a dairy has been demonstrated using one of the techniques, and displayed alongside emission rates estimated using conventional sensors and an inverse modeling technique.

The first algorithm operates as an iterative minimum least-squares estimator, and demonstrates its stability and functionality in retrieving aerosol concentration from both synthetic and real lidar signals [4]. The technique formulates the lidar equation as a nonlinear matrix operation and the aerosol concentration as a vector over the entire range of interest. The lidar equation is iteratively linearized and a least-squares solution to the aerosol concentration vector is calculated using the Newton-Raphson method. This method converges quickly if the initial guess is close to the desired solution, but it has poor global convergence. Consequently, for atmospheres with large optical depths, other methods may be more effective, such as a modified form of Newton's method or the Levenberg-Marquardt method [60]. By choosing an appropriate weighting matrix, the solution approximates a maximum-likelihood solution to the lidar equation for the case of Gaussian noise.

Both algorithms describe the atmosphere as a linear combination of assumed aerosol

components, and retrieves the coefficients of these components in the form of an estimated state vector  $\mathbf{x}$ . The lidar equation describes the measured returned power  $P$  as a function of range  $z$ , as well as two optical coefficients, backscatter  $\beta(z)$  and extinction  $\sigma(z)$ , also functions of range.

$$P(z) = f \{ \beta(z), \sigma(z) \} = K \frac{\beta(z)}{z^2} \exp \left( -2 \int_0^z \sigma(z') dz' \right) \quad (1.1)$$

Estimation of both of these optical coefficients is normally an ill-posed problem, unless a relationship between them is assumed. Most currently popular algorithms assume a power-law relationship between backscatter  $\beta$  and extinction  $\sigma$  coefficients of each individual lidar channel.

$$\beta = k\sigma^r \quad (1.2)$$

The expressions  $k$  and  $r$  are constants. Unfortunately, this approach ignores any dependency that may exist between channels of a multi-wavelength lidar. Since the ultimate science goal of an elastic lidar is often the estimation and characterization of aerosols themselves, rather than their optical properties, it is reasonable to formulate both backscatter and extinction as functions of aerosol concentration  $n$ . For the case of a multi-wavelength lidar measuring an atmosphere with multiple components, this can be represented in vector form by (1.3).

$$\boldsymbol{\beta}_z = f_\beta \{ \mathbf{n}(z) \} \quad \boldsymbol{\sigma}_z = f_\sigma \{ \mathbf{n}(z) \} \quad (1.3)$$

The elements of  $\boldsymbol{\beta}_z$  and  $\boldsymbol{\sigma}_z$  are the optical coefficients of the individual wavelengths and the elements of  $\mathbf{n}$  are the amplitudes of the individual component aerosols at range  $z$ . As a result, the measured returned power over multiple wavelengths can be modeled as a nonlinear function of multiple aerosol components.

$$\mathbf{P}_z = f \{ \mathbf{n}(z) \} \quad (1.4)$$

Formulating the lidar equation as a function of multiple aerosol components both prevents the problem from being ill-posed, and allows the retrieval algorithms described in this dissertation to take full advantage of any dependency between the measured lidar channels.

In practice, lidar signals have measurement noise added to them and the lidar equation is nonlinear. The algorithms formulate a linear approximation of the lidar equation using Newton's method. The linear approximation of (1.4) is shown by (1.5).

$$f \{ \mathbf{n}(z) \} \approx (\nabla f \{ \mathbf{n}(z) \} - \nabla f \{ \mathbf{n}_0(z) \}) \mathbf{n}_0(z) + f \{ \mathbf{n}_0(z) \} \quad (1.5)$$

The linearization requires an *a priori* estimate of the solution. By iteratively using (1.5) to linearize the lidar equation, applying the standard weighted minimum least-squares solution [61], and feeding it back into the linearization equation, the retrieved solution will converge to a point close to the desired solution. The weighting matrix should be chosen to account for the noise levels of the individual measurement channels.

The second algorithm is an example of an EKS [5]. This algorithm is demonstrated to estimate the effective particle radius from both synthetic and real lidar signals. The algorithm is similar to the algorithm proposed by Dias [50]. By selecting an appropriate state vector, the lidar signal can be represented by a state-update matrix and a nonlinear observation function. Additionally, this technique assumes that the change in aerosol concentration as a function of range is a random variable, whose covariance is known beforehand. This technique has also been developed from the perspective of optimization, while also incorporating additional *a priori* knowledge and is of lower order computational complexity than the first technique.

Like the previous algorithm, this algorithm composes the state vector using component aerosol amplitude. Inspection of (1.1) shows that the measured power of a lidar signal at a given range is a function of the backscatter at that range and the sum of the extinction coefficients between the lidar and that range. However, it is possible to represent the lidar signal as a Markov process by substituting the cumulative extinction with a new variable. Dias composes the state vector  $\mathbf{x}$  in the form shown in (1.6).

$$\mathbf{x}_z = \begin{bmatrix} \beta_z \\ \gamma_z \end{bmatrix} \quad \gamma_z = \sum_{z'=0}^z \sigma_{z'} \quad (1.6)$$

Whereas (1.6) describes the state vector using optical coefficients for a single wavelength, in the multi-wavelength case an alternative form for the state vector can be composed of two vectors, describing both the current component aerosol amplitude and the cumulative component aerosol amplitude.

$$\mathbf{x}_z = \begin{bmatrix} \mathbf{n}_z \\ \gamma_z \end{bmatrix} \quad \gamma_z = \sum_{z'=0}^z \mathbf{n}_{z'} \quad (1.7)$$

Using this state vector, the process of the lidar measurement can be described using a system including a state-update equation and an observation equation.

$$\mathbf{x}_{z+1} = \begin{bmatrix} \mathbf{0} & \mathbf{0} \\ \mathbf{1} & \mathbf{1} \end{bmatrix} \mathbf{x}_z + \mathbf{w}_t \quad \text{cov}(\mathbf{w}_z) = \begin{bmatrix} \text{cov}(\mathbf{n}_z) & \mathbf{0} \\ \mathbf{0} & \mathbf{0} \end{bmatrix} \quad (1.8)$$

$$\mathbf{P}(z) = \mathbf{k} \cdot \frac{f_\beta(\mathbf{n}_z)}{z^2} \cdot \exp(-2\Delta_z f_\sigma(\gamma_z)) + \boldsymbol{\nu}_z \quad \text{cov}(\boldsymbol{\nu}_z) = R$$

These equations may be implemented as an extended Kalman filter by linearizing the observation equation using Newton's method. This algorithm has much better computational performance than the previously described one due to its much reduced state vector size. Whereas the state vector of the first technique is proportional to the number of range bins in the lidar signal, the state vector of the second technique is proportional to the lidar pulse width in bins. Furthermore, it can be implemented as a fixed-lag EKS by augmenting the state vector with aerosol concentration coefficients over a set window size.

## References

- [1] C. C. Marchant, “Algorithm development of the Aglite-lidar instrument,” Master’s thesis, Utah State University, Logan, UT, 2008.
- [2] G. E. Bingham, C. C. Marchant, V. V. Zavyalov, D. Ahlstrom, K. D. Moore, D. Jones, T. D. Wilkerson, L. Hipps, R. S. Martin, J. L. Hatfield, J. H. Prueger, and R. L. Pfeiffer, “Lidar based emissions measurement at the whole facility scale: Method and error analysis,” *Journal of Applied Remote Sensing*, vol. 3, p. 033510, 2009.
- [3] C. C. Marchant, T. D. Wilkerson, G. E. Bingham, V. V. Zavyalov, J. M. Andersen, C. B. Wright, S. S. Cornelsen, R. S. Martin, P. J. Silva, and J. L. Hatfield, “Aglite lidar: a portable elastic lidar system for investigating aerosol and wind motions at or around agricultural production facilities,” *Journal of Applied Remote Sensing*, vol. 3, p. 033511, 2009.
- [4] C. C. Marchant, T. K. Moon, and J. H. Gunther, “An iterative least square approach to elastic-lidar retrievals for well-characterized aerosols,” *IEEE Transactions on Geoscience and Remote Sensing*, vol. 48, pp. 2430–2444, 2010.
- [5] C. C. Marchant, M. D. Wojcik, and W. J. Bradford, “Estimation of aerosol effective radius by multi-wavelength elastic lidar,” *IEEE Transactions on Geoscience and Remote Sensing*, submitted for publication, 2010.
- [6] C. C. Marchant, K. D. Moore, M. D. Wojcik, R. S. Martin, J. L. Hatfield, J. H. Prueger, and R. L. Pfeiffer, “Estimation of dairy particulate matter emission rates by lidar and inverse modeling,” *Transactions of the ASAE*, submitted for publication, 2010.
- [7] R. Bureau, *Météorologie*, vol. 3, p. 292, 1946.
- [8] S. S. Friedland, J. Katzenstein, and M. R. Zatzick, “Pulsed searchlighting the atmosphere,” *Journal of Geophysical Research*, vol. 61, pp. 415–434, 1956.
- [9] F. J. McClung and R. W. Hellwarth, “Giant optical pulsations from ruby,” *Journal of Applied Physics*, vol. 33, pp. 828–829, 1962.
- [10] G. Fiocco and L. D. Smullin, “Detection of scattering layers in the upper atmosphere (60-140 km) by optical radar,” *Nature*, vol. 199, pp. 1275–1276, 1963.
- [11] G. Fiocco and G. Colombo, “Optical radar results and meteoric fragmentation,” *Journal of Geophysical Research*, vol. 69, pp. 1795–1803, 1964.
- [12] G. Fiocco and G. Grams, “Observations of the aerosol layer at 20 km by optical radar,” *Journal of Atmospheric Science*, vol. 21, pp. 323–324, 1964.
- [13] R. T. H. Collis, “Lidar observation of cloud,” *Science*, vol. 149, pp. 978–981, 1965.
- [14] R. T. H. Collis and M. G. H. Ligna, “Note on lidar observations of particulate matter in the stratosphere,” *Journal of Atmospheric Science*, vol. 23, p. 255, 1966.

- [15] R. T. H. Collis and J. Oblanas, "Project Pre-Gondola II. Airborne lidar observations," Stanford Research Institute Aerophysics Lab., 1968.
- [16] R. T. H. Collis, F. G. Fernald, and J. E. Alder, "Lidar observation of Sierra-wave conditions," *Journal of Applied Meteorology*, vol. 7, pp. 227–233, 1968.
- [17] R. T. H. Collis, "Lidar: A new atmospheric probe," *Quarterly Journal of the Royal Meteorological Society*, vol. 92, pp. 220–230, 1966.
- [18] P. M. Hamilton, "The use of lidar in air pollution studies," *Air and Water Pollution*, vol. 10, pp. 427–434, 1966.
- [19] P. M. Hamilton, "Plume height measurements at northfleet and tilbury power stations," *Atmospheric Environment*, vol. 1, p. 379, 1967.
- [20] P. M. Hamilton, "The application of a pulsed-light rangefinder (lidar) to the study of chimney plumes," *Philosophical Transactions of the Royal Society of London*, vol. 265, pp. 153–172, 1969.
- [21] E. W. Barrett and O. Ben-Dov, "Appliation of the lidar to air pollution measurements," *Journal of Applied Meteorology*, vol. 6, pp. 500–515, 1967.
- [22] W. B. Johnson, "Lidar observations and the diffusion and rise of stack plumes," *Journal of Applied Meteorology*, vol. 8, pp. 443–449, 1969.
- [23] W. B. Johnson, "Lidar applications in air pollution research and control," *Journal of the Air Pollution Control Association*, vol. 19, pp. 176–180, 1969.
- [24] J. A. Reagan, M. P. McCormick, and J. D. Spinhirne, "Lidar sensing of aerosols and clouds in the troposphere and stratosphere," *Proceedings of the IEEE*, vol. 77, pp. 433–448, 1989.
- [25] F. G. Fernald, B. M. Herman, and J. A. Reagan, "Determination of aerosol height distributions by lidar," *Journal of Applied Meteorology*, vol. 11, pp. 482–489, 1972.
- [26] G. W. Grams, J. I. H. Blifford, B. G. Schuster, and J. J. D. Luisi, "Complex index of refraction of airborne fly ash determined by laser radar and collection of particles at 13 km," *Journal of Atmospheric Science*, vol. 29, pp. 900–905, 1972.
- [27] G. W. Grams, J. I. H. Blifford, D. A. Gillette, and P. B. Russell, "Complex index of refraction of airborne soil particles," *Journal of Applied Meteorology*, vol. 13, pp. 459–471, 1974.
- [28] J. A. Reagan, J. D. Spinhirne, and D. M. Byrne, "Atmospheric particulate properties inferred from lidar and solar radiometer observations compared with simultaneous in situ aircraft measurements: A case study," *Journal of Applied Meteorology*, vol. 16, pp. 911–928, 1977.
- [29] A. Ansmann, M. Riebesell, and C. Weitkamp, "Measurement of atmospheric aerosol extinction profiles with a Raman lidar," *Optics Letters*, vol. 15, pp. 746–748, 1990.

- [30] J. A. Reagan, D. M. Byrne, and B. M. Herman, "Bistatic LIDAR: A tool for characterizing atmospheric particulates: Part II - The inverse problem," *IEEE Transactions on Geoscience and Remote Sensing*, vol. GE-20, pp. 236–243, 1982.
- [31] L. R. Bissonnette and D. L. Hutt, "Multiply scattered aerosol lidar returns: Inversion method and comparison with in situ measurements," *Applied Optics*, vol. 34, pp. 6959–6975, 1995.
- [32] D. I. Cooper, W. E. Eichinger, D. E. Hof, D. Seville-Jones, R. C. Quick, and J. Tiee, "Observations of coherent structures from a scanning lidar over an irrigated orchard," *Agricultural and Forest Meteorology*, vol. 67, pp. 239–252, 1994.
- [33] T. E. Stoughton, D. R. Miller, X. Yang, and K. M. Ducharme, "A comparison of spray drift predictions to lidar data," *Agricultural and Forest Meteorology*, vol. 88, pp. 15–26, 1997.
- [34] B. A. Holmén, W. E. Eichinger, and R. G. Flocchini, "Application of elastic lidar to PM10 emissions from agricultural nonpoint sources," *Environmental Science Technology*, vol. 32, pp. 3068–3076, 1998.
- [35] B. A. Holmén, T. A. James, L. L. Ashbaugh, and R. G. Flocchini, "Lidar-assisted measurement of PM10 emissions from agricultural tilling in California's San Joaquin Valley, part I: Lidar," *Atmospheric Environment*, vol. 35, pp. 3265–3277, 2001.
- [36] B. A. Holmén, D. R. Miller, A. L. Hiscox, W. Yang, J. Wang, T. Sammis, and R. Bottoms, "Near-source particulate emissions and plume dynamics from agricultural field operations," *Journal of Atmospheric Chemistry*, vol. 59, pp. 117–134, 2008.
- [37] A. L. Hiscox, D. R. Miller, B. A. Holmén, W. Yang, and J. Wang, "Near-field dust exposure from cotton field tilling and harvesting," *Journal of Environmental Quality*, vol. 37, pp. 551–556, 2008.
- [38] W. E. Eichinger, H. E. Hodder, D. I. Cooper, L. E. Hipps, R. Knight, W. P. Kustas, J. Nichols, and J. H. Prueger, "Lidar measurement of boundary layer evolution to determine sensible heat fluxes," *Journal of Hydrometeorology*, vol. 6, pp. 941–953, 2005.
- [39] M. C. W. Sandford, "Laser scatter measurements in the mesosphere and above," *Journal of Atmospheric and Terrestrial Physics*, vol. 29, pp. 1657–1662, 1967.
- [40] P. B. Russell, T. J. Swissler, and M. P. McCormick, "Methodology for error analysis and simulation of lidar aerosol measurements," *Applied Optics*, vol. 18, pp. 3783–3797, 1979.
- [41] S. A. Young, "Analysis of lidar backscatter profiles in optically thin clouds," *Applied Optics*, vol. 34, pp. 7019–7031, 1995.
- [42] W. Viezee, E. E. Uthe, and R. T. H. Collis, "Lidar observations of airfield approach conditions: An exploratory study," *Journal of Applied Meteorology*, vol. 8, pp. 274–283, 1969.

- [43] P. A. Davis, “The analysis of lidar signatures of cirrus clouds,” *Applied Optics*, vol. 8, pp. 2099–2102, 1969.
- [44] J. D. Klett, “Stable analytical inversion solution for processing lidar returns,” *Applied Optics*, vol. 20, pp. 211–220, 1981.
- [45] F. G. Fernald, “Analysis of atmospheric lidar observations: some comments,” *Applied Optics*, vol. 23, p. 652, 1984.
- [46] J. D. Klett, “Extinction boundary value algorithms for lidar inversion,” *Applied Optics Letters*, vol. 22, pp. 514–515, 1983.
- [47] E. Yee, “Information-theoretic method for the inversion of the lidar equation,” *Applied Optics*, vol. 28, pp. 1628–1637, 1989.
- [48] F. Rocadenbosch, C. Soriano, A. Comeron, and J. Baldasano, “Adaptive filter solution for processing lidar returns: optical parameter estimation,” *Applied Optics*, vol. 37, pp. 7019–7034, 1998.
- [49] F. Rocadenbosch, C. Soriano, A. Comeron, and J. Baldasano, “Lidar inversion of atmospheric backscatter and extinction-to-backscatter ratios by use of a Kalman filter,” *Applied Optics*, vol. 38, pp. 3175–3189, 1999.
- [50] J. M. B. Dias, J. M. N. Leitao, and E. S. R. Fonseca, “Reconstruction of backscatter and extinction coefficients in lidar: a stochastic filtering approach,” *IEEE Transactions on Geoscience and Remote Sensing*, vol. 42, pp. 443–456, 2004.
- [51] R. E. Warren, R. G. Vanderbeek, A. Ben-David, and J. L. Ahl, “Simultaneous estimation of aerosol cloud concentration and spectral backscatter from multiple-wavelength lidar data,” *Applied Optics*, vol. 47, pp. 4309–4320, 2008.
- [52] Y. Sasano, “Light scattering characteristics of various aerosol types derived from multiple wavelength lidar observations,” *Applied Optics*, vol. 28, pp. 1670–1679, 1989.
- [53] M. D. Guasta, M. Morandi, L. Stefanutti, B. Stein, and J. P. Wolf, “Derivation of Mount Pinatubo stratospheric aerosol mean size distribution by means of a multiwavelength lidar,” *Applied Optics*, vol. 33, pp. 5690–5697, 1994.
- [54] K. Rajeev and K. Parameswaran, “Iterative method for the inversion of multiwavelength lidar signals to determine aerosol size distribution,” *Applied Optics*, vol. 37, pp. 4690–4700, 1998.
- [55] G. von Cossart, J. Fiedler, and U. von Zahn, “Size distributions of NLC particles as determined from 3-color observations of NLC by ground-based lidar,” *Geophysical Resources Letters*, vol. 26, pp. 1513–1516, 1999.
- [56] J. Heintzenberg, H. Muller, H. Quenzel, and E. Thomalla, “Information content of optical data with respect to aerosol properties: numerical studies with a randomized minimization-search-technique inversion algorithm,” *Applied Optics*, vol. 20, pp. 1308–1315, 1981.

- [57] P. Qing, H. Nakane, Y. Sasano, and S. Kitamura, "Numerical simulation of the retrieval of aerosol size distribution from multiwavelength laser radar measurements," *Applied Optics*, vol. 28, pp. 5259–5265, 1989.
- [58] D. P. Donovan and A. I. Carswell, "Principal component analysis applied to multiwavelength lidar aerosol backscatter and extinction measurements," *Applied Optics*, vol. 36, pp. 9406–9424, 1997.
- [59] C. Böckmann, "Hybrid regularization method for the ill-posed inversion of multiwavelength lidar data in the retrieval of aerosol size distributions," *Applied Optics*, vol. 40, pp. 1329–1342, 2001.
- [60] W. Press, S. Teukolsky, W. Vetterling, and B. Flannery, *Numerical Recipes in C*. New York: Prentice Hall, 1971.
- [61] T. K. Moon and W. C. Stirling, *Mathematical Methods and Algorithms for Signal Processing*. Upper Saddle River: Prentice Hall, 2000.

## Chapter 2

### Aglite Description and Operation<sup>1</sup>

#### **2.1 Application**

Agricultural aerosol sources can contribute a significant component to air pollution in many regions of the country. Characterization of the aerosol emissions of agricultural operations is required to determine best management practices for controlling agricultural aerosol emissions and to establish a scientific basis for crafting regulations concerning agricultural aerosols. For regulatory purposes, aerosol mass concentration is measured in terms of PM, specifically PM<sub>2.5</sub> and PM<sub>10</sub>, both of which are pollutants regulated by the National Ambient Air Quality Standards [1, 2].

Examples of agricultural sources of PM include “fugitive dust” from soil tillage, aerosols generated from crop processing, and chemical precipitate from vapors emitted by manure. Agricultural aerosol sources differ from industrial aerosol sources in that the source is often spread out over a significant area, resulting in a highly dispersed aerosol plume and a variable rate of emission over time.

In the past, conventional methods for measuring and characterizing aerosol sources have used point sensors and software models of atmospheric dispersion. Using these tools, measurements are made by deploying a limited number of point sensor instruments around the site of interest and using software models to interpolate and extrapolate aerosol concentration values around the entire site. These methods offer low spatial resolution due to the sparse number of instruments used. Additionally, these methods rely on assumptions of Gaussian diffusion of aerosols and are therefore reliable only over relatively long periods of time.

---

<sup>1</sup>C. C. Marchant, T. D. Wilkerson, G. E. Bingham, V. V. Zavyalov, J. M. Andersen, C. B. Wright, S. S. Cornelsen, R. S. Martin, P. J. Silva, and J. L. Hatfield, Reproduced by permission of SPIE as: “Aglite lidar: A portable elastic lidar system for investigating aerosol and wind motions at or around agricultural production facilities,” *J. Appl. Remote Sens.*, vol. 3, 033511, 2009.

Attempts have also been made to measure emissions from soil tillage operations by placing instruments directly on a tractor implement [3–6].

The deficiency of these conventional techniques is that they are unable to make measurements over the volume of a dispersed aerosol plume. A sparse distribution of instruments is unable to cover the entire area of the aerosol source, and the point sensors cannot take measurements higher than the towers upon which they are mounted. As a result, these techniques are insufficient for characterizing the emission rate of the whole plume.

This deficiency can be addressed using lidar technology, which provides a means to measure the distribution of aerosols over large areas with high spatial and temporal resolution. Previous applications of lidar technology to measuring agricultural aerosols have demonstrated this capability by measuring the height and morphology of dust plumes generated by field preparation [7,8]. Mapping of aerosol concentration by lidar has been demonstrated in agricultural settings [9,10]. The interaction of lidar scan patterns and moving aerosols provides valuable information on the wind structures responsible for aerosol transport. In particular, certain types of scans permit the visualization of wind velocity, variability of wind speed over large areas, and shapes of aerosol plumes. Buttler et al. reviewed lidar wind velocity measurements, principally those based on cross-correlations between successive positions of aerosol clouds, with the lidar direction oriented along the wind or cross-wind [11]. They compared wind data collected with radiosondes, remote laser Doppler profiles, and elastic backscatter lidar profiles. Good agreements were demonstrated between these instruments, indicating that wind observations with elastic lidar afford valuable data on the transport within the planetary boundary layer [11]. Kovalev and Eichinger provide a comprehensive review of backscatter correlation methods and Doppler-based lidar techniques in both the time and frequency domains, and point out the many types of atmospheric observations in which wind lidar technology can now play an important role [12]. Pioneering work on correlations was carried out by Derr and Little, Zuev, and Eloranta [13–15]. Sasano et al. corrected the 2-D aerosol patterns for their motion during the lidar scan, and found that the correlation-based wind velocities agreed with the wind

data from co-located meteorology towers [16].

3-D volume-imaging scans have been developed for wind profile measurements [17–19]. The lofting of aerosol plumes from a farm due to a combination of wind and convection has been shown by Eichinger [20]. The development of holographic scanning lidars has led to new methods of cross-beam wind analysis using aerosol and cloud tracking [21–25]. The work reported here is based on simple, straightforward analyses of (1) 1-D plume motion as a function of time, and (2) the visualization of 2-D plumes by time-dependent lidar scans across the plume shape.

The Energy Dynamics Laboratory at Utah State University teamed with researchers from the Department of Agriculture, Agriculture Research Service to build Aglite, an elastic lidar system plus an array of point source instruments and software for measuring the emission rate of agricultural aerosol sources. In addition to measuring the 3-D structure of an agricultural aerosol plume over a large volume, the Aglite system is able to measure the concentration of PM<sub>2.5</sub> and PM<sub>10</sub>. These data are used in conjunction with data on wind speed and direction to characterize the emission rate of the source [26].

The design of the Aglite lidar is described here and its ability to map the aerosol concentration and dynamics of aerosol plumes with high resolution is demonstrated. Aglite's ability to measure wind velocity by means of aerosol tracking is also demonstrated.

## 2.2 Aglite Lidar Description

The primary system requirements of the Aglite lidar were to (1) make the system eye-safe at the operating range; (2) make the system sufficiently robust and portable to be deployed at an agricultural site; and (3) make the scanning and data logging sufficiently fast to capture the dynamics and structure of an entire plume.

The Aglite instrument is a portable lidar mounted in a small trailer and utilizing a fixed vertical telescope with a steering mirror used as an azimuth-elevation beam director. Figure 2.1 shows the Aglite lidar instrument in its trailer housing deployed at a farm. The lidar has a measurement rate as fast as 1/10 of a second, with a minimum range resolution of 6 m. Its maximum practical range is roughly 3 km, depending on environmental conditions.

Aglite's steering mirror and fast response time enable it to map aerosol concentration in units of PM<sub>2.5</sub> and PM<sub>10</sub> over a large volume of air in a relatively short amount of time, with a single 2-D scan taking less than a minute. This speed also enables Aglite to capture plume dynamics with good temporal resolution.

### 2.2.1 Hardware Design

The requirement to make Aglite eye-safe drove the decision to make Aglite a micropulse lidar. This mitigates eye-safety issues because of the lower pulse energy. Additionally, the high pulse rate potentially allows for an extremely high measurement rate. As a consequence of the low pulse-energy, photon-counting detection is used. The lidar has a narrow field of view (FOV) and uses narrow-band filters to limit background noise from solar radiation. The design concepts for Aglite and its component layout are shown in fig. 2.2, and are based in part on the design by McGill et al. for the Cloud Physics lidar [27].

The transmitter chosen for Aglite is a solid-state Nd:YAG laser from Photonics Industries International, Inc. (Photonics Industries International, Inc, 390 Central Avenue, Bohemia, NY 11716). (The instruments and manufacturers named herein were used in the research experiments described; however, their use does not constitute an endorsement or preferential treatment by the project researchers or sponsors.) The laser generates three wavelengths: 1064, 532, and 355 nm using doubling and tripling crystals. These three wavelengths define the measurement channels of the lidar and are called the infrared (IR), visible (V), and ultra-violet (UV) channels, respectively. The laser operates at 10 KHz and is diode-pumped. The laser head is vertically mounted on the optical bench of the lidar and is coupled to the diodes and the power supply, which are located in the electronics rack. The laser is water-cooled and is coupled to a separate chiller. Immediately after leaving the laser head, the beam passes first through a 7x beam expander, at which point the beam far-field full divergence angles are 0.37, 0.30, and 0.27 mrad, respectively. Average output powers employed are 4.35, 0.48, and 0.93 W, respectively, yielding pulse energies of 435, 50, and 93  $\mu$ J. The beam is directed through a neutral density (ND) filter station, which allows for controlled attenuation of the beam (20 to 100% power) as desired over the lidar's operating



Fig. 2.1: Aglite lidar instrument in deployment configuration.

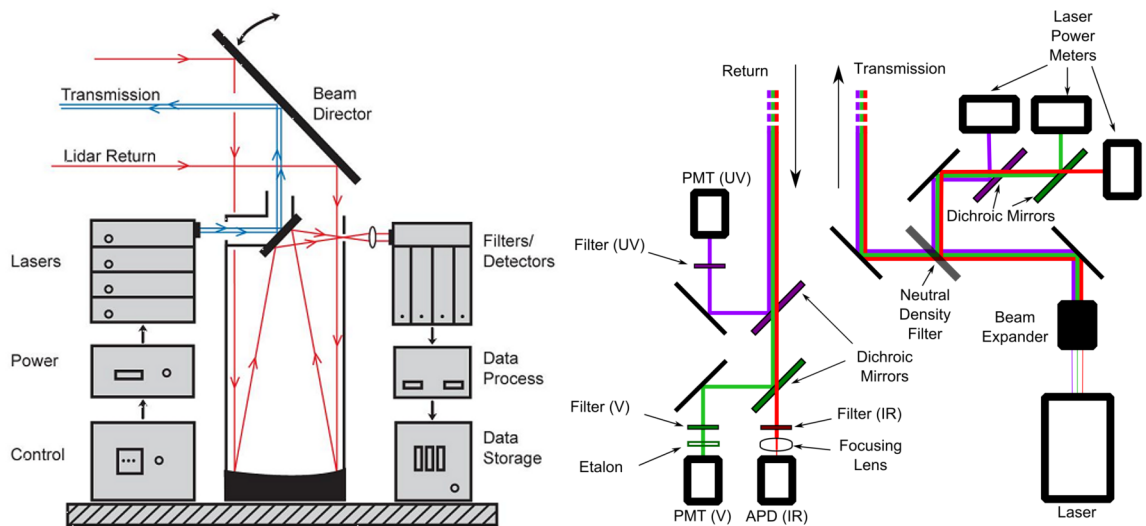


Fig. 2.2: Aglite lidar conceptual arrangement and layout of optical bench components.

range on grounds of eye safety. Reflection from the ND filter is separated into its component wavelengths using dichroic reflectors and fed into power sensors to monitor laser output strength, as shown in fig. 2.2. After passing through the ND filter, the beam is directed onto a mirror mounted on the central obstruction of the telescope, at which point the laser is co-aligned with the receiver telescope.

Aglite uses a simple Newtonian telescope with a 28-cm diameter primary mirror (fig. 2.2). The mirror has a focal length of 0.91 meters. A field stop confines the telescope's full field-of-view to 0.45 mrad. After the laser beam reflects off the telescope's central obstruction, a pointing mirror directs the beam and collects the returned signal. At this point, the outgoing beam and returned signal are coaxially aligned. Movement of the pointing mirror controls the direction the lidar looks, but does not change the relative alignment of the outgoing beam and return signal. The pointing mirror actuators have a pointing knowledge resolution of 1 mrad and pointing repeatability of 5 mrad.

As shown in fig. 2.2, the signal is collected by the telescope and separated into its component wavelengths using dichroic mirrors. Each channel then passes through a narrow-band interference filter made by Barr Associates, Inc. (Barr Associates, Inc, 2 Lyberty Way, Westford, Massachusetts 01886.) The 532 nm channel then passes through an etalon made by TecOptics (TecOptics, 1760 Grand Avenue, Merrick, NY 11566.) The 1064 nm channel is focused onto an avalanche photo-diode (APD), while the remaining two channels pass into photo-multiplier tubes (PMT). The APD is model SPCM-AQR-14 made by PerkinElmer (PerkinElmer, 44370 Christy Street, Fremont, California 94538), having a quantum efficiency of 2%. The PMTs are model 9954A made by Electron Tubes (Electron Tubes, 100 Forge Way, Unit F, Rockaway, New Jersey 07866), with quantum efficiencies of 14% and 27% at 532 and 355 nm, respectively. The choice of detectors for Aglite was based on the generally superior signal-to-noise ratio for PMTs in the visible and ultraviolet wavelengths, given sufficient filtering of the green intensity maximum of sunlight, and the infrared sensitivity of the APD. This conclusion has also been confirmed by Agishev et al. [28]. A commercial high speed, multichannel photon counting interface (APCS, ASRC Aerospace, Greenbelt, MD)

was used to log and record the photon counts for each channel. The electronic system for operating the entire Aglite system and recording the multichannel data has been described in detail by Cornelsen [29].

For example, the Fabry-Perot etalon inside Aglite on the 532 nm channel is not temperature controlled, as is sometimes done in lidar instrumentation. The Aglite system compensates for temperature induced instrument changes by periodic (every 20 min) re-calibration of the lidar return signal magnitude against an OPC placed in the field. It is important that the instrument not fluctuate during the course of a single 20-minute scan. The etalon discussed here is an air spaced etalon constructed of Class 0 Zerodur with a nominal mirror spacing of 4.011 mm. The coefficient of thermal expansion of Zerodur is 0.002 ppm/K. During a typical 10-hour day of field experiments, the temperature inside of the lidar enclosure can change as much as 25 K, corresponding to an etalon spacing change of 0.5 ppm, or 2 nm. The transmission change due to a 2-nm spacing increase is < 1%, and the peak shift of the transmission fringe is < 0.25 pm. Therefore the transmission changes over any given 20-minute scan are limited to temperature effects of a single Kelvin or less, and so are on the order of 0.05% transmission changes. Either way, the transmission changes due to temperature effects are well within the 37 pm wavelength bandwidth of the etalon and also that of the laser. Therefore, systematic temperature induced transmission changes do not contribute significantly to the observed noise threshold for the entire instrument.

The actual range resolution of this lidar lies in the range of 12-18 m for wavelengths between 355 and 1064 nm, owing to the data system's time bins of 40 nsec, the respective laser pulse lengths, and the pulse discrimination times of the detectors. The repetition rate of the laser sets the lidar's maximum range at 15 km; in practice, the maximum useful range can be as close as 1.5 km due to high solar background radiation or unfavorable atmospheric conditions.

The laser head, transmission optics, and receiver optics are all mounted on a single optical bench, vertically oriented in a 6-point vibration-isolated frame along with the telescope. The optical path is housed under light-tight aluminum covers that also serve to

keep the optics clean. The entire frame is covered with removable panels. An important component of the lidar is an external air-blower. This draws air from outside of the trailer through a filter, conditions it, and blows it into the lidar housing to maintain positive pressure in the optical system and minimize flying insect intrusion. This is essential to mitigate the risks of contamination from dust and insects during a campaign because the receiver telescope is exposed to the outside environment.

The beam director is computer controlled by a rack-mounted PC, with scan control points established using the visible camera and a joystick controller. Azimuth and elevation control were achieved using Newport RV series and BG series precision motorized stages. It can direct the beam with an azimuth range of 270 degrees and an elevation range between -10 degrees to +45 degrees, and is retracted hydraulically inside the trailer for travel. A video camera looks at the director mirror to provide the operator a 5 degrees field of view along the beam path for safety monitoring. Data from the lidar can be linked by WiFi network to other sites and bring environmental data to the operator. Table 2.1 summarizes the system parameters of the lidar.

### 2.2.2 Eye-Safety

For safe field operation the lidar beam should be eye-safe at the facility under investigation, and a buffer area around the lidar where the beam strength is not eye-safe should be guaranteed off-limits to personnel. The most demanding eye-safety criterion for Aglite is the green light at 532 nm near the peak sensitivity of the human eye. While certain other lidar groups have preferred to operate at “eye safe” infrared wavelengths such as 1555 nm [30], the Nd:YAG-derived triplet (355, 532, 1064 nm) was chosen for Aglite on the basis of good control over the field test environment and the three wavelength capability for discriminating between aerosol types. For Aglite the requirement is that the operating distance of the lidar from the facility must meet or exceed the eye-safety range for 532 nm, which is approximately 450 meters using 20% of the laser power. Calculations of the value of the Nominal Optical Hazard Distance,  $R_{NOHD}$ , for eye exposure are carried out in accordance with ANSI Laser Safety Standard Z136.1 [31]. The ophthalmic basis for these

Table 2.1: Aglite lidar system parameters.

Laser Type	Solid-State Nd:YAG	Data Time Resolution	0.1 s		
Laser Repetition Rate	10 kHz	Steering Resolution	5 $\mu$ rad		
Telescope Type	Newtonian	Telescope Diameter	28 cm		
Telescope FOV	450 $\mu$ rad (full angle)	Etolon Free Spectral Range	37 pm		
Etolon Reflectivity Finesse	6.1	Etolon Peak Transmission	$\geq 98.4\%$		
Wavelengths	Laser Output Energy	Detector Efficiency	Filter Efficiency	Filter Bandwidth	Range Resolution
355 nm	93 $\mu$ J	27%	76%	150 pm	18 m
512 nm	50 $\mu$ J	14%	70%	120 pm	12 m
1064 nm	435 $\mu$ J	2%	70%	150 pm	18 m

standards has most recently been treated by Delori et al. [32].

The minimum distance for safe eye exposure to  $N$  laser pulses at a given wavelength is given by (2.1).

$$R_{NOHD} = \frac{1}{\Theta} \sqrt{\frac{4\Phi}{\pi} MPE(N)} \quad (2.1)$$

The expression  $\Theta$  is the full divergence angle of the transmitted laser pulse (mrad),  $\Phi$  is the pulse energy (J), and  $MPE(N) = MPE_P \cdot N^{-1/4}$ , where  $MPE_P$  is the maximum permissible exposure per pulse ( $J/cm^2$ ) at the human cornea for each wavelength. Table 2.2 provides representative values for  $R_{NOHD}$  for the range of laser output powers of Aglite, based on a standard blink response criterion of 0.25 seconds. At an operating distance of 600 meters and reduced optical power, Aglite is “eye-safe” at all wavelengths. The equivalent ranges for other exposure durations are readily calculated using recognized standards [31, 33, 34]. Table 2.2 shows a conservative analysis of eye-safety distances based on 100% optical efficiency of laser transmission, for a “blink” exposure of 1/4 second at laser pulse repetition frequency of 10 kHz.

Table 2.2: Representative eye-safety distances for Aglite lidar.

$\lambda(\text{nm})$	$MPE_p(\text{J/cm}^2)$	$\Phi(\mu\text{J})$	$R_{NOHD}(\text{m})$ 20% output	$R_{NOHD}(\text{m})$ 100% output
355	5.6e-3	100	6.7	15
532	5.0e-7	50	450	1000
1064	5.0e-6	500	360	810

### 2.3 Lidar Data and Calibration

The information content of the lidar return is summarized by the well-known lidar equation (2.2), which describes the lidar return signal as a function of range  $z$  for wavelength  $\lambda$ .

$$P_\lambda(z) = P_0 L \frac{c\tau}{2} A_\lambda(z) \frac{\beta_\lambda(z)}{z^2} \exp \left( -2 \int_0^z \sigma_\lambda(z') dz' \right) \quad (2.2)$$

The term  $P_\lambda(z)$  is the measured reflected power for distance  $z$  and is measured in photon counts.  $P_0$  is the output power of the lidar,  $L$  is the lidar coefficient, which represents the combined efficiency of the transmitter optics, receiver optics, and detectors,  $c$  is the speed of light,  $\tau$  is the pulse width of the lidar, and  $A_\lambda(z)$  is the receiver efficiency at range  $z$ .  $A_\lambda(z)$  is defined as  $GFF \cdot A$ , where  $A$  is the geometric area of the telescope and  $GFF$  is the geometric form factor (GFF) or overlap function defined by the geometry of the transmitter and telescope.  $\beta_\lambda(z)$  is the atmospheric backscatter coefficient, and  $\sigma_\lambda(z)$  is the atmospheric extinction coefficient.

The backscatter and extinction coefficients both depend upon molecular scattering, as well as on the characteristics of the background and emission aerosols. The solution of (2.2) requires knowledge of the optical parameters of both the background and source aerosols, as well as the contribution of molecular scattering; these need to be measured at one or more reference points in order to interpret lidar return intensity in terms of particle concentration, and to extract aerosol information [35].

The geometric form factor is an effect caused by mismatch between the transmitter and receiver cones of sight. Its magnitude and shape are highly sensitive to the alignment of

the lidar optics. The expected value of the GFF is approximately 80% at the lidar range of 650 m (fig. 2.3), as modeled using the optical design parameters of the lidar [36].

Experimentally derived values for the GFF were found to be within 10% of the modeled GFF for ranges greater than 650 m [37]. Because of the sensitivity of the GFF to misalignment of the optics, the lidar system is aligned before measurements are taken. This is done using a target at distances greater than 1 km; the lidar is directed at the target, and the optics are adjusted to maximize the magnitude of the signal reflected by the target.

To calibrate the aerosol density detected by Aglite, the local particulate concentrations in the lidar's FOV was determined using both optical and aerodynamic mass fraction sensors. These sensors include real time OPCs that utilize a laser to count and size particles into eight user-specified size bins (OPC Model 9722, Met One Instruments, Inc., Grants Pass, OR). The aerodynamic particulate impactors are portable, self-contained, filter-based particulate samplers containing Teflon filters that are weighed pre- and post-exposure (MiniVol, Airmetrics, Eugene, OR.) By co-locating AirMetric samplers and OPC instruments, the relationship between mass concentration and aerosol backscatter was established. Aerosol parameters are developed for lidar characterization and calibration by directing the lidar beam past the AirMetric/OPC instrument pair [35].

It is expected that photon-counting measurements by the Aglite system are Poisson-distributed random variables, and this is confirmed by inspection of Aglite data. Figure 2.4(a) shows the average measured signal from a 10-minute data set from a measurement campaign at an Almond orchard, where Aglite was used to observe harvesting operations. This particular data set was taken with Aglite staring continuously in one direction horizontally through the atmosphere. Figure 2.4(b) shows a comparison of the average power measured at 600 m range with the ensemble variance values over a range of varying period lengths. The variance of the signal is either comparable to or greater than the average measured power. Figure 2.4(c) illustrates the relationship between the average measured power and variance at each range of the lidar signal for the UV channel. Figure 2.4(d) shows a particle normalized histogram of the measured lidar signal at 600 m, together with the probability

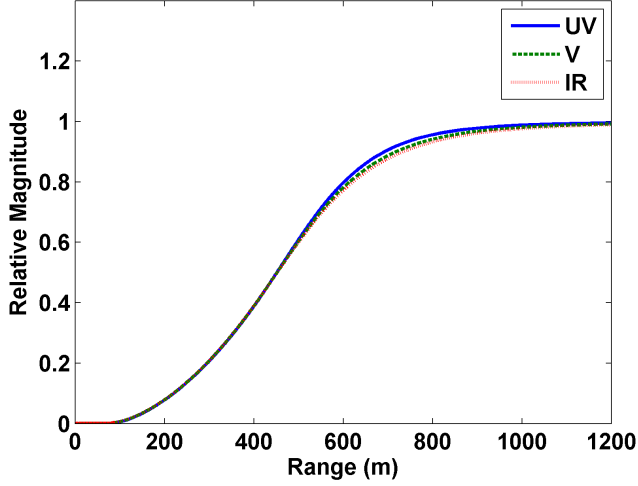


Fig. 2.3: Aglite geometric form factor as a function of range.

mass functions of the Poisson distributions that most closely approximate them. A major source of noise in Aglite data is photon-counting noise. Background solar radiation also contributes significantly to the signal, which increases the expected total number of photons measured by the detectors and hence increases the expected variance of the signal.

Representative plots of the SNR of the retrieved backscatter for each of the three wavelengths as a function of distance are shown in fig. 2.5. In this case, SNR is defined as the ratio of the mean aerosol backscatter amplitude over the standard-deviation of the aerosol backscatter. Both graphs show the SNR measured from data taken near a cotton gin operation. Figure 2.5 was taken during daylight operation at approximately 7:30 in the evening, when the  $\text{PM}_{10}$  level was approximately  $7 \mu\text{g}/\text{m}^3$ . Figure 2.5(b) shows the SNR at approximately 9:30 in the evening, when background levels of  $\text{PM}_{10}$  had risen slightly to  $8 \mu\text{g}/\text{m}^3$ . The improvement in SNR in the right panel is largely due to the absence of solar background radiation during night operation. The bumps and dips in the plots are due to the environmental variability of aerosol concentration at the site. Smooth portions of the plots correspond to homogeneous regions of atmosphere.

For these measurements, in-situ instruments were used to absolutely calibrate the lidar signal and to determine the ratio of the aerosol backscatter contribution to the backscatter

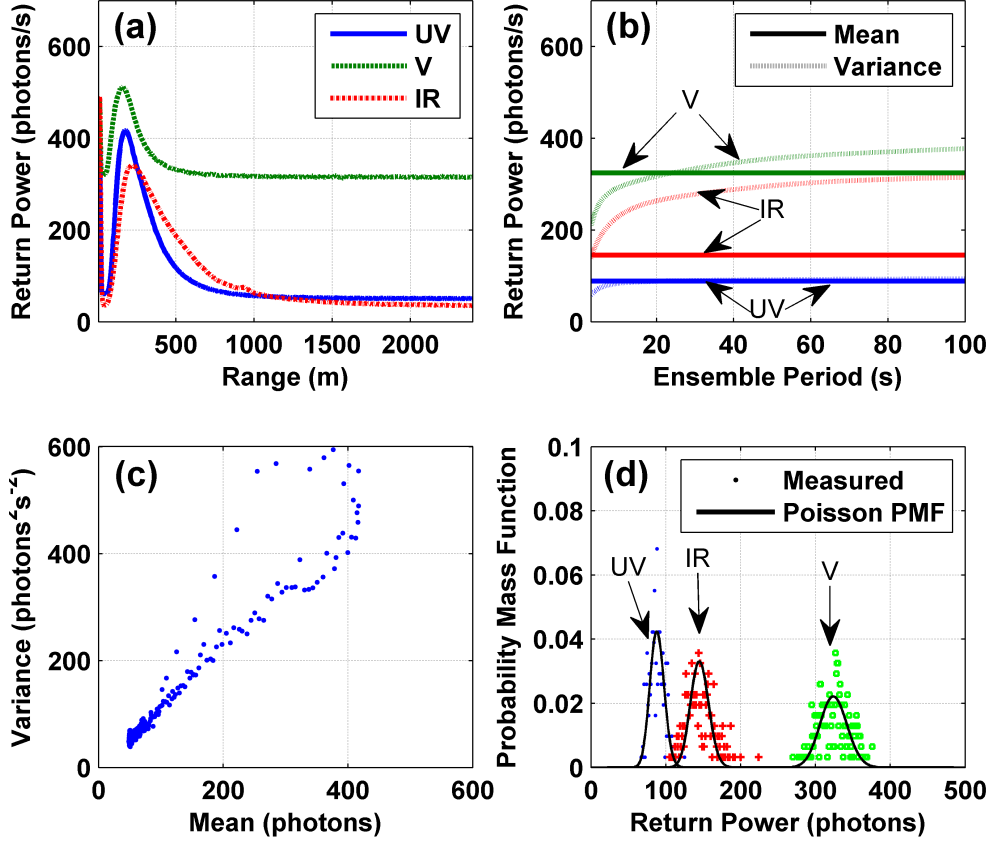


Fig. 2.4: Example return power signal and signal variance from Aglite.

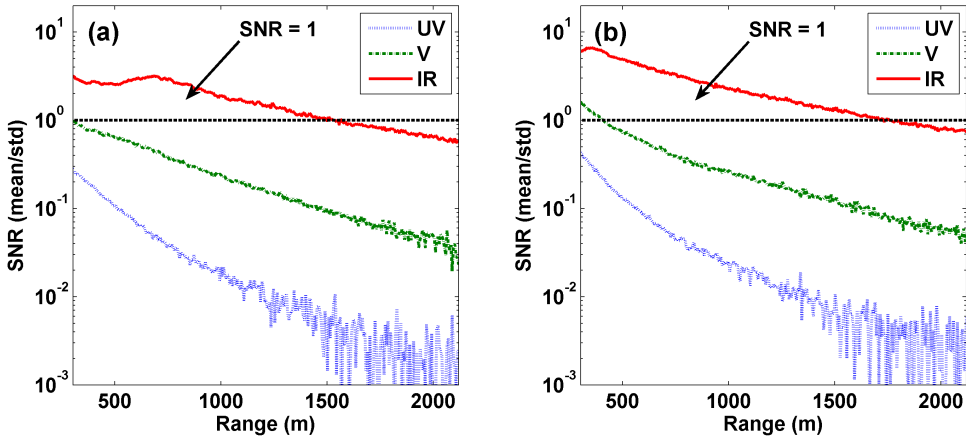


Fig. 2.5: Two examples of SNR values observed by Aglite under field conditions.

contribution due to molecular scattering. The SNR at a given range can be improved either by not attenuating the laser, or by increasing the integration time of the measurement.

## 2.4 Example Data and Discussion

The Aglite system has been deployed at several agricultural facilities in the U.S. since becoming operational in the summer of 2005. Examples from these campaigns are given below to illustrate Aglite's ability to capture the structure and dynamics of plumes from agricultural sources.

### 2.4.1 Aerosol Detection Capability

The lidar control computer has the useful ability to display the raw lidar signal in real time, allowing the individual wavelength return signals to be monitored so that the data integration time can be adjusted and pulse dead-time corrections can be made as needed. The control computer also stores the raw lidar signal for later processing. Additionally, the lidar includes a secondary display unit which shows 2-D images of the lidar scan regions in near real time. This display removes the baseline component of the background noise and performs range-correction to the signal amplitude before displaying the data, as illustrated by fig. 2.6. The conversion of raw lidar data into aerosol concentration is performed after the conclusion of a campaign.

The Aglite software consists of three parts: the lidar control software, the visualization software, and the lidar retrieval software. The lidar control software governs the data acquisition and pointing control of the lidar hardware. This program is written in the Labview programming environment and is installed on the PC in the Aglite hardware rack. The main functions of this program are to control the pointing of the steering mirror and store the values measured by the photon detectors. The software allows the user to control the lidar either manually, by means of a game controller, or in an automatic mode, in which the program directs the lidar scan in a repeating predetermined pattern. This program also controls parameters such as the PMT voltage levels, the range gate, and the integration time of the lidar. Additionally, the control software writes the lidar measurements and orientation

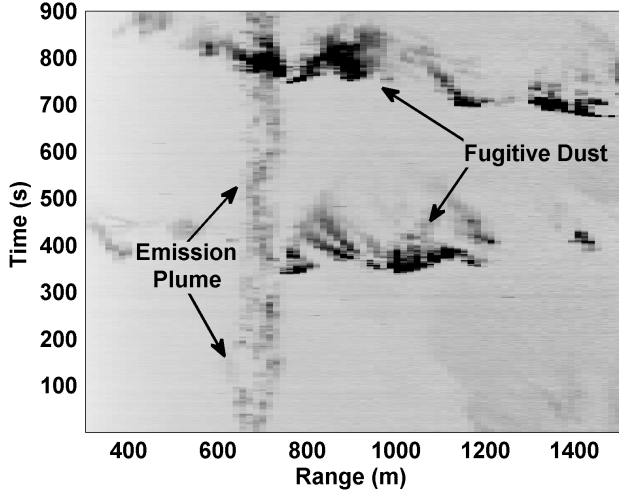


Fig. 2.6: Typical “stare” image of range-normalized IR channel intensity.

parameters to a data file for storage and also broadcasts them over the local computer network using the user datagram protocol (UDP). The visualization software receives the UDP broadcast data and graphs in near real-time the current raw signal measured by Aglite.

The visualization software is a program with a graphical user interface written in the Matlab programming environment. The function of this program is to assist the operator by providing real-time visualization of lidar data. The visualization software is installed on a separate laptop that is networked to the rack-mounted PC. The visualization software captures the data broadcast by the rack-mounted PC broadcasts and plots them in range-normalized form. The user selects the range and channel of data to view. The visualization software automatically determines the type of motion currently being performed—stare, horizontal sweep, or vertical sweep—and plots it in an appropriate 2-D graph. The visualization software is also able to plot data from the archived data files generated by the lidar control software.

The lidar retrieval software consists of a set of scripts written for the Matlab programming environment. The lidar retrieval software retrieves PM concentration from the lidar data files, allowing the lidar scans to be converted into maps of aerosol concentration. An aerosol may scatter the three wavelengths of Aglite with different efficiencies. This allows the

retrieval software to extract information about the aerosol particle size distribution as well as the concentration of the aerosol. This software does not run concurrently while the lidar is taking data, but is executed offline, after the measurements have been completed. This software requires additional inputs from point sensors to calibrate the lidar signal and to calculate the lidar-ratio and other parameters needed to perform the lidar retrieval.

#### 2.4.2 Fixed Direction Lidar Measurement

Figure 2.6 shows data collected during a lidar “stare” period in which the FOV is fixed horizontally so the lidar can record the range-dependent backscatter as a function of time (here about 15 minutes). These measurements are from a field-campaign at a swine-finishing facility. This stationary stare past a barn complex shows an emission plume from the facility ( $\sim 650$  m) and two transient road dust plumes. The co-location of the lidar path and the tower-mounted particle monitors close to the barns provides the essential step for the optical-particulate calibration of the lidar.

The choice to design Aglite with three channels adds significant cost and complexity over a one-channel design. The additional channels, however, provide additional information about the aerosol characteristics under investigation. The point sensors deployed with Aglite directly measure the particle size distribution of both the background atmosphere aerosol and the target aerosol under investigation. The accuracy of these point measurements can be gauged by comparing them to Aglite measurements.

An example is given here of retrieving aerosol concentration and mode radius using Aglite’s lidar retrieval algorithm. A stationary stare past the barn complex was performed for 400 seconds and averaged. This measurement was pre-processed to remove the baseline noise component and to correct for the GFF. The measurement was then converted to the logarithmic range-normalized form, as shown in fig. 2.7(a). The lidar inversion was performed using the Klett solution for two scatterers to estimate the backscatter coefficients as a function of range [38]. This is illustrated in fig. 2.7(b).

Point sensor measurements were used to provide the backscatter values of the homogeneous background and the lidar ratios for the two scatterers. A least-squares solution

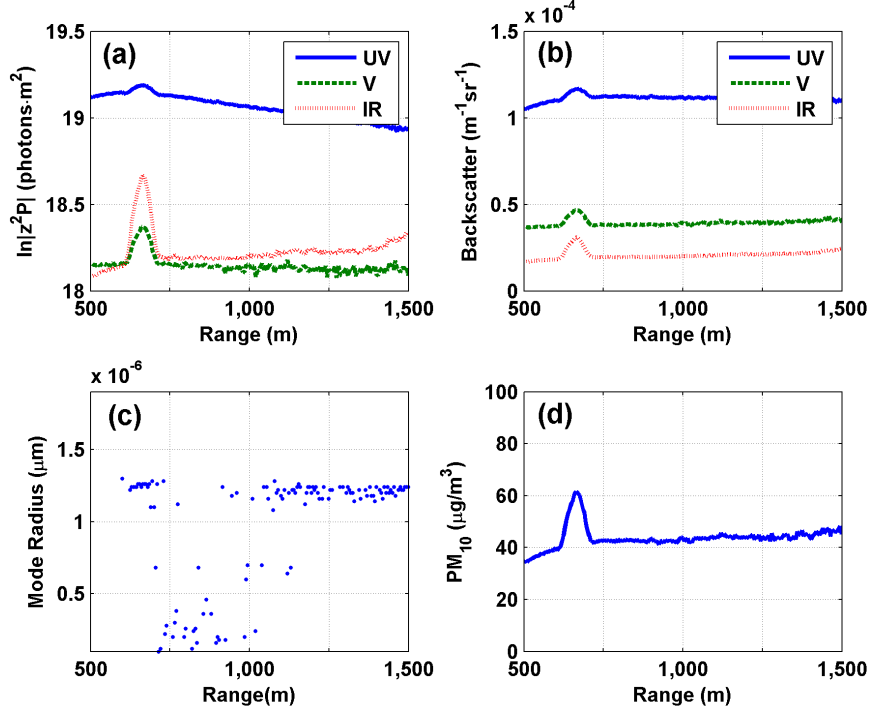


Fig. 2.7: Example retrieval showing measured signal, estimated backscatter, mode radius, and PM<sub>10</sub> concentration.

for aerosol concentration and mode radius was then calculated at every range, assuming a log-normal distribution with  $\sigma = 2.0$  and indices of refraction for a water-soluble aerosol [39]. The retrieved mode-radius as a function of range is given in fig. 2.7(c). The solution for mode radius was restricted to a window between 0 and 2  $\mu\text{m}$ . It is reasonable to assume that when the solution to the mode radius was at the limits of this window, there may have been insufficient aerosol to accurately measure the mode radius. This is supported by the fact that at ranges where a plume is visible in fig. 2.7(b), the retrieved mode radius is comfortably within the allowable window of values. Figure 2.7(d) shows the PM<sub>10</sub> concentration that results from the solution, assuming unit density. A complete description of the algorithm is given elsewhere [35], along with details of the algorithm's performance and more examples of its use.

#### 2.4.3 Crosswind Scans for Aerosol Flux Measurements

The lidar scan patterns typically used to characterize the amount of aerosol emissions

include vertical profiles between barns at upwind and downwind facility boundaries and horizontal profiles above the facility. Interleaved with these scans of the facility area are stationary stares near the *in situ* instruments to probe the aerosol parameters.

Figure 2.8(a) illustrates the use of horizontal scans that serve to locate the sources of aerosol emissions around an agricultural facility. The dark dots located roughly 700 m west of the lidar correspond to measurement towers set up between livestock barns and the dark vertical streaks between 1200 and 1400 west of the lidar are fugitive dust plumes from a north-south dirt road at that location. These scans are particularly useful when placing the aerosol point sampling equipment. While even a single wavelength system can provide these types of data, the multiple wavelength capability of Aglite comes into play in determining and tracking the distribution of particulate size classes and their flux from the facility.

Figure 2.8(b) introduces a type of scan called a “staple” scan, which Aglite uses extensively to bracket the net emission from an agricultural facility [26]. The range dependent lidar signal is displayed in three steps: an elevation scan upwards, an azimuthal scan to the right, and an elevation scan downwards. Here the wind blows south-to-north (left-to-right). On the right side, the lidar captures a plume emitted from a swine barn at a distance of roughly 600 m that have risen to about 30 meters in height. This specific scan was completed in 1.5 minutes.

## 2.5 Aerosol Traced Wind Motion

### 2.5.1 Wind Velocity from Lidar “Stares”

Figure 2.9 shows aerosol return data collected with the beam parallel to a graveled road in a fixed, horizontal stare. Each strong signal return represents a dust cloud generated by a road traffic event. Direction motion of aerosols is towards the lidar, with a dashed line tracking the movement of individual return features over time. The figure shows distance from the lidar on the horizontal axis and time difference on the vertical access. Tracking such long plume trains is possible because the lidar can see through individual plumes that have very low aerosol density and optical extinction. The scale represents the lidar signal

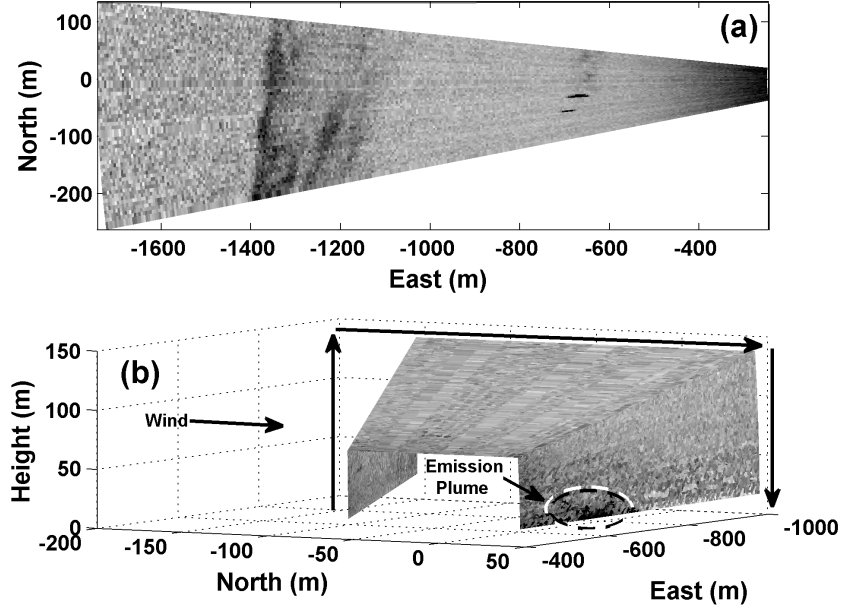


Fig. 2.8: Examples of typical horizontal and staple scans by Aglite.

intensity from white (weak) to black (strong). As in fig. 2.6(b), this display is a space-time ( $x,t$ ) graph of plume motion, with time increasing upward and lidar range increasing to the right. This type of lidar data record and subsequent velocity analysis is analogous to “streak photography,” which has found wide applications in experimental fluid dynamics [40–43]. Holmén et al. adopted this method for lidar and pointed out its significance for quantitatively measuring plume velocity and transport based on straightforward physical calibrations of distance and time [6, 7].

In fig. 2.9, the wind motion is from right to left and, based on the persistence of the  $x$ - $t$  streaks, lies directly within the lidar field of view. When the lidar is not aligned with the wind direction, the streaks are much shorter, as the cloud moves across the beam. The slopes of these aerosol traces (dashed lines) are direct measures of the wind speed (distance/time). The speed observed in this figure is consistent with the data measured on a tower at the 600 m range. As expected, the wind also demonstrates velocity variations with distance (shown in the white boxes). The lidar is so sensitive that clumps and clouds of aerosols can be tracked in daytime and nighttime situations, even when they are too tenuous to be seen

by eye.

Most of our “staring” observations have been made at reasonably steady winds above 3 m/s. During one of our experiments, one noteworthy occasion of very slow and highly variable horizontal air motion was observed at the 20 m height. This state of motion suggests almost stagnant air dominated by convection with a fluctuating horizontal wind component. This is shown in fig. 2.10 where the horizontal speeds varied between 1.4 m/s toward the lidar and 1.5 m/sec away from the lidar, out to a range of 5 km. In addition to the well-defined parts of the plumes, there are low-contrast, triangular patches in this x-t image indicating that a 1-1.5 km-wide pattern of drifting motion of aerosols persisted for at least 5 minutes. This is a remarkable cross-sectional snapshot of an atmospheric pattern that could not be seen by any means other than lidar. The capability of lidar as a tool for documenting wide area patterns of air motion dominated by convection is an important addition to the study of aerosol transport from agricultural sources.

### 2.5.2 Vertical Scans for Cross-Sections of Moving Plumes

The staring and staple scans with the lidar show that the aerosol transport consists of clumps of highly variable particle concentrations that originated from ground level. To see the full structure and height of these plumes and how they evolve, one must use vertical lidar scans  $\theta(t) = \theta_0 \pm Ct$  aimed upwind or downwind, with the scans made rapidly enough to follow the plume propagation over a range of hundreds of meters. These scans can display complete cross sections of plume structure as opposed to accidental intersections orthogonal to the motion. For the data shown in fig. 2.11, the lidar alternately scanned up and down at a rate of  $C = 0.1$  deg/s. The resulting images are divided into interleaved sequences of “up” frames in the left column and “down” frames in the right column. Each sequence shows radial aerosol plume motion with the wind towards the lidar. Each panel was recorded over a 30-second vertical scan. This record of plume motion shows a total of 4 minutes of aerosol transport of road dust plumes.

Two distinct plume populations are evident in fig. 2.12: (1) low-altitude, low-velocity (0.8 m/s) plumes originating at 600 m; and (2) higher plumes with higher speeds (2.3 m/s)

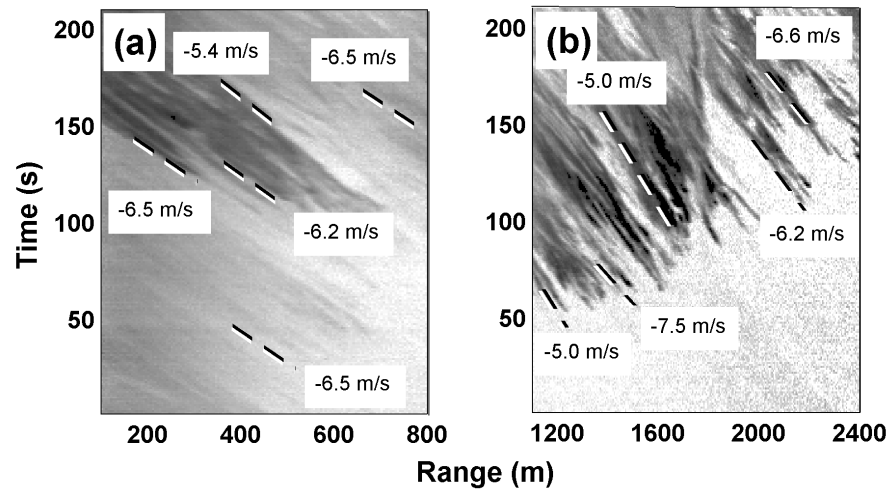


Fig. 2.9: Local wind patterns shown in a time series of lidar returns at different ranges.

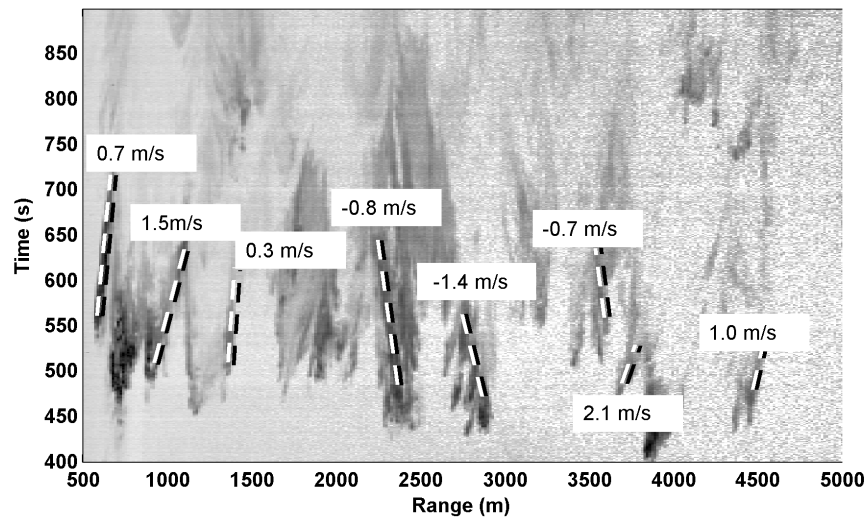


Fig. 2.10: Returns from an 8-minute horizontal stare at 20 m height during light and variable wind conditions.

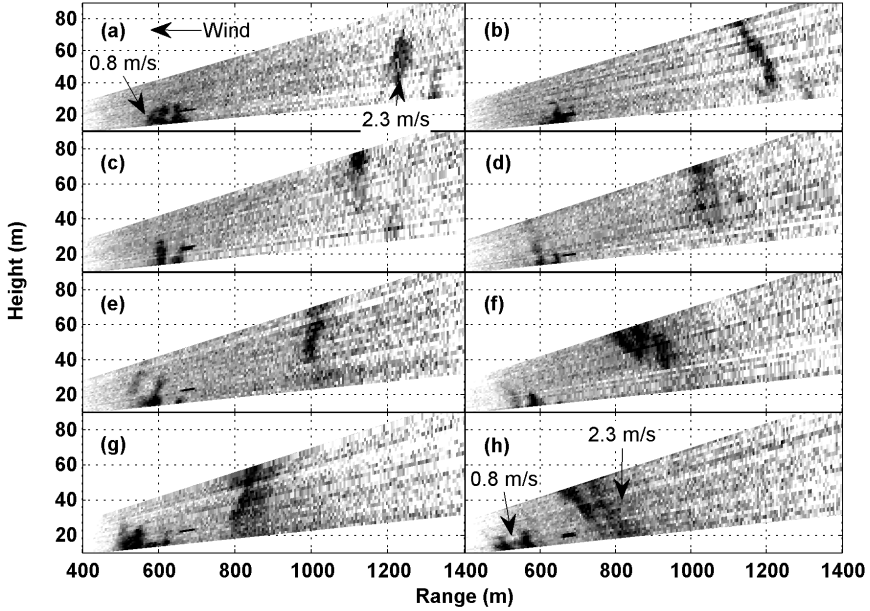


Fig. 2.11: Series of 30-second vertical scans showing the movement of plumes toward the lidar.

that originate from more distant sources. The visualization of these structures provides important information regarding the scales of aerosol inhomogeneities involved in particle transport.

There are obvious differences between up and down images due to the kinematic distortion inherent in the record of a moving object (plume) obtained by the time-dependent scan angle  $\theta(t)$ . These images show that appearance of the plume profile, especially the direction of its tilt, depends both on the plume's true shape and velocity. The shape of the plume is assumed to be made up of many smaller ragged plumes, which can be approximated as a series of fairly straight pillars that tilt forward from vertical by some angle in the direction of wind movement [44–47]. Laboratory observations of such fluid flows have also been shown [48]. Instability in the atmospheric surface layer produces intermittent gusts in which the local vertical velocity can be comparable to the horizontal wind, creating a plume of soil aerosols carried upward at an angle tilted nearly 45 degrees forward in the wind direction.

To demonstrate unscrambling the simultaneous time dependence of lidar scans and

plume motions, fig. 2.12 shows an example of vertical scans of a fugitive road dust plume moving towards the lidar. The left pane shows an initial scan, with the lidar scanning from 1.4 degrees up to 8 degrees elevation, immediately followed by a scan from 8 degrees back down to 1.4 degrees, which is shown in the right pane. The approximate shape and orientation of the tilted plume is represented by a heavy black slanted line. A series of parallel dotted lines represent its position as the plume blows from right to left. As the moving plume is intercepted by the lidar scan, the intersection first rises (left panel) in an arc from **A** to **B**, and then connects to a down-going arc from **B** to **C** (right panel). The velocity and forward tilt calculated for this plume are unique solutions to the kinematic equations underlying these arcs. The streaks in the left panel correspond to a plume tilted forward 20 degrees from vertical with a speed of 10 m/s and the streaks in the right panel correspond to a tilt angle of 50 degrees from vertical with a speed of 7 m/s.

The observational value and advantage of lidar, as illustrated here, is that it clearly provides an extremely sensitive way to see tenuous aerosol features that are hard to see or photograph. Conventional pictures of the above plumes could not be obtained because of low optical contrast. However, a successful attempt to photograph such plumes was made elsewhere under more extreme conditions. An environment was found where wind, surface temperature, lighting, and loose dust could make it possible to obtain visible images of plumes. Figure 2.13 is a photograph taken in the Black Rock desert in Nevada in September 2006. The image has been inverted and its contrast increased to improve the viewability of the dust plumes, which are indicated by the gray arrow. Similar to the lidar observations, these plumes retained their shape as they marched steadily to the east with the wind, and were tilted substantially forward at near -45 degree angles that varied slightly during any single gust event.

## 2.6 Conclusion

The Aglite lidar was developed to provide a tool for rapidly characterizing agricultural and other anthropogenic aerosol sources. It has normally been deployed as a member of a suite of classical aerosol characterization instruments that provide the additional aerosol

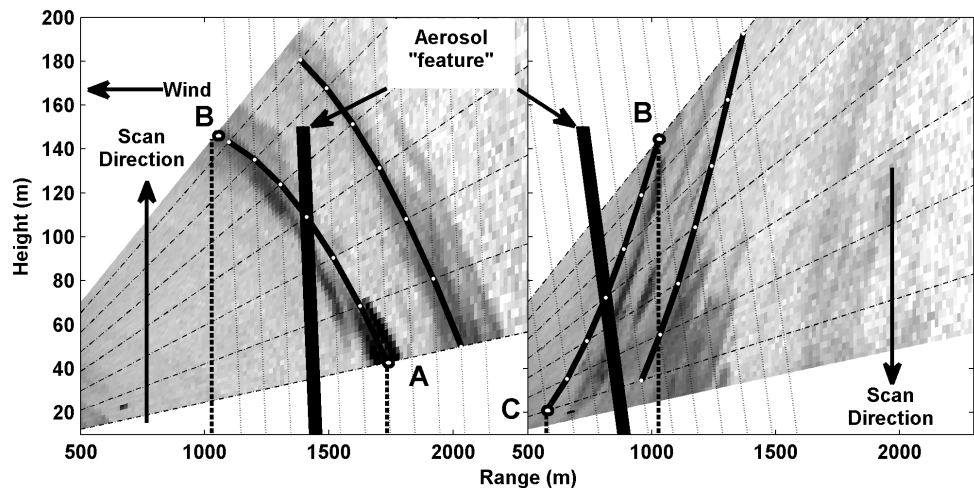


Fig. 2.12: Distortion of the aerosol image due to simultaneous motion of wind and lidar scan.

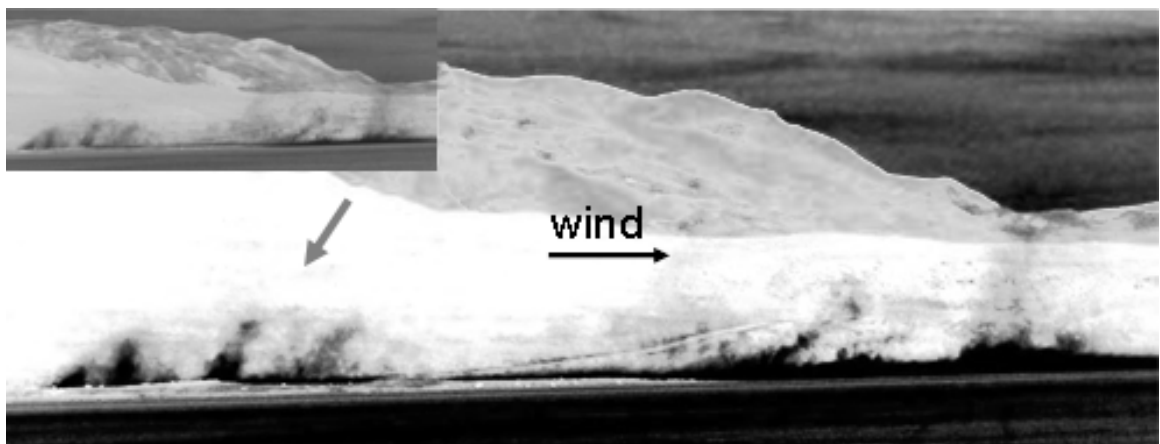


Fig. 2.13: Wind-blown plumes of clay dust in Nevada.

optical response functions required to fully understand the sources and their emission rates. The lidar beam can be scanned in the horizontal and vertical planes to allow emission tracking and profiling. The lidar allows the mapping the relative backscatter of an aerosol plume at 1064, 532, and 355 nm wavelengths, with a resolution of 12 meters (range) and 5 mrad (angle). Sensitivity at up to 10 samples/second is sufficient to identify non-visible facility plumes of PM<sub>10</sub> and PM<sub>2.5</sub> particulates, which are regulated by the US Environmental Protection Agency (EPA). The lidar has been used to create near real-time profiles of plume structures and low-elevation clouds and to map the location of aerosol sources over a range of facility types, including confined agricultural feeding operations, agricultural product processing, and mobile source operations, where variable wind and short-duration treatment evaluations are desired. Processing the lidar returns also allow the wind speed and the character of the temporal and spatial variation of aerosol plume structures to be determined. When the lidar is combined with point instruments, which provide the additional aerosol characteristics needed to determine optical parameters, the system can provide calibrated aerosol size-fraction information and emission fluxes from the studied operations [35]. The most important capabilities for Aglite's monitoring of agricultural emissions are (1) the mapping of aerosol concentration and motion around a facility, and (2) the measurement of aerosol mass concentration emission rates from a facility.

## References

- [1] Code of Federal Regulations-TITLE 40: Protection of Environment, "40 CFR 50.6-National primary and secondary ambient air quality standards for PM<sub>10</sub>," [<http://vlex.com/vid/19784798>], 2005.
- [2] Code of Federal Regulations-TITLE 40: Protection of Environment, "40 CFR 50.7-National primary and secondary ambient air quality standards for PM<sub>2.5</sub>," [<http://vlex.com/vid/19784804>], 2005.
- [3] J. B. Baker, R. J. Southard, and J. P. Mitchell, "Agricultural dust production in standard and conservation tillage systems in the San Joaquin Valley," *Journal of Environmental Quality*, vol. 34, pp. 1260–1269, 2005.

- [4] H. Clausnitzer and M. J. Singer, “Respirable-dust production from agricultural operations in the Sacramento Valley, CA,” *Journal of Environmental Quality*, vol. 25, pp. 877–884, 1996.
- [5] H. Clausnitzer and M. J. Singer, “Intensive land preparation emits respirable dust,” *Journal of California Agriculture*, vol. 51, pp. 27–30, 1997.
- [6] B. A. Holmen, W. E. Eichinger, and R. G. Flocchini, “Application of elastic lidar to PM<sub>10</sub> emissions from agricultural nonpoint sources,” *Environmental Science Technology*, vol. 32, pp. 3068–3076, 1998.
- [7] B. A. Holmen, T. A. James, L. L. Ashbaugh, and R. G. Flocchini, “Lidar-assisted measurement of PM<sub>10</sub> from agricultural tilling in California’s San Joaquin Valley-part I: Emission factors,” *Atmospheric Environment*, vol. 35, pp. 3251–3264, 2001.
- [8] B. A. Holmen, T. A. James, L. L. Ashbaugh, and R. G. Flocchini, “Lidar-assisted measurement of PM<sub>10</sub> from agricultural tilling in California’s San Joaquin Valley-part II: Emission factors,” *Atmospheric Environment*, vol. 35, pp. 3265–3277, 2001.
- [9] B. A. Holmen, D. R. Miller, A. L. Hiscox, and R. G. Flocchini, “Near-source particulate emissions and plume dynamics from agricultural field operations,” *Journal of Atmospheric Chemistry*, vol. 59, pp. 117–134, 2008.
- [10] A. L. Hiscox, D. R. Miller, B. A. Holmen, W. Yang, and J. Wang, “Near-field dust exposure from cotton field tilling and harvesting,” *Journal of Environmental Quality*, vol. 37, pp. 551–556, 2008.
- [11] W. T. Buttler, C. Soriano, J. M. Baldasano, and G. H. Nickel, “Remote sensing of three-dimensional winds with elastic lidar: explanation of maximum crosscorrelation method,” *Boundary-Layer Meteorology*, vol. 101, pp. 305–328, 2001.
- [12] V. A. Kovalev and W. E. Eichinger, *Elastic Lidar: Theory, Practice, and Analysis Methods*. Hoboken: Wiley-Interscience, 2004.
- [13] V. E. Derr and C. G. Little, “A comparison of remote sensing of the clear atmosphere by optical, radio, and acoustic radar techniques,” *Applied Optics*, vol. 99, pp. 1982–1983, 1970.
- [14] V. E. Zuev, “Lidar sounding of the atmosphere to estimate static and dynamic characteristics of aerosol inhomogeneities,” in *Proc. 5th Conf. Laser Radar Studies of the Atmosphere*, 1973.
- [15] E. W. Eloranta, J. M. King, and J. A. Weinman, “The determination of wind speeds in the boundary layer by monostatic lidar,” *Journal of Applied*, vol. 14, pp. 1485–1489, 1975.
- [16] Y. Sasano, H. Hirohara, T. Yamasaki, H. Shimizu, N. Takeuchi, and T. Kawamura, “Horizontal wind vector determination from the displacement of aerosol distribution patterns observed by a scanning lidar,” *J. Appl. Meteor.*, vol. 21, pp. 1516–1523, 1982.

- [17] W. P. Hooper and E. W. Eloranta, "Lidar measurements of wind in the planetary boundary layer: the method, accuracy, and results from joint measurements with radiosonde and kytoon," *Journal of Climate and Applied Meteorology*, vol. 25, pp. 990–1001, 1986.
- [18] D. I. Cooper and W. E. Eichinger, "Structure of the atmosphere in an urban planetary boundary layer from lidar and radiosonde observations," *Journal of Geophysical Research*, vol. 99, pp. 22 937–22 948, 1994.
- [19] P. W. Young and E. W. Eloranta, "Calculation of divergence and vertical motion from volume imaging lidar data," *Journal of Geophysical Research*, vol. 100, pp. 25 557–25 583, 1995.
- [20] W. E. Eichinger, D. I. Cooper, J. L. Hatfield, L. E. Hipps, J. J. Nicholls, R. L. Pfeiffer, and J. Preuger, "Use of elastic lidar to examine the dynamics of plume dispersion from an agricultural facility," in *Workshop on Agricultural Air Quality: State of the Science*, Ecological Society of America, 2006.
- [21] G. K. Schwemmer, "Conically scanned holographic lidar telescope," U.S. Patent No. 5,255,065, Oct. 1993.
- [22] D. V. Guerra, G. K. Schwemmer, A. D. W. Jr., S. S. Chaudhuri, and T. D. Wilkerson, "Prototype holographic atmospheric scanner for environmental remote sensing," *Journal of Geophysical Research*, vol. 104, pp. 22 287–22 292, 1999.
- [23] G. K. Schwemmer, T. D. Wilkerson, J. A. Sanders, D. V. Guerra, D. O. Miller, and S. E. Moody, "Ground based operational testing of holographic scanning lidars," in *Advances in Laser Remote Sensing*, A. Dabas, C. Loth, and J. Pelon, Eds. Ecole Polytechnique, 2001, pp. 69–72.
- [24] T. D. Wilkerson, J. A. Sanders, and I. Q. Andrus, "Kinematic analysis of conically scanned environmental properties," U.S. Patent No. 6,535,158, 2003.
- [25] T. D. Wilkerson, S. Cornelsen, C. Earl, D. Huish, J. Cutts, S. Call, M. Anderson, and G. K. Schwemmer, "Monitoring of air motion using lidar and video observations," in *Proceedings of the American Meteorological Society. 2nd Symposium of Lidar Atmospheric Applications*, 2005.
- [26] G. E. Bingham, C. C. Marchant, V. V. Zavyalov, D. Ahlstrom, K. D. Moore, D. Jones, T. D. Wilkerson, L. Hipps, R. S. Martin, J. L. Hatfield, J. H. Prueger, and R. L. Pfeiffer, "Lidar based emissions measurement at the whole facility scale: method and error analysis," *Journal of Applied Remote Sensing*, vol. 3, p. 033510, 2009.
- [27] M. McGill, D. Hlavka, W. Hart, V. S. Scott, J. Spinhirne, and B. Schmid, "Cloud physics lidar: instrument description and initial measurement results," *Applied Optics*, vol. 41, pp. 3725–3734, 2002.
- [28] R. Agishev, B. Gross, F. Moshary, A. Gilerson, , and S. Ahmed, "Simple approach to predict APD/PMT lidar detector performance under sky background using dimensionless parameterization," *Optics and Lasers in Engineering*, vol. 44, pp. 779–796, 2006.

- [29] S. Cornelsen, “Electronics design of the AGLITE instrument,” Master’s thesis, Utah State University, Logan, UT, 2005.
- [30] W. Gong, T. H. Chyba, and D. A. Temple, “Eye-safe compact scanning LIDAR technology,” *Optics and Lasers in Engineering*, vol. 45, pp. 898–906, 2007.
- [31] Z136.1, Laser Institute of America, “American national standard for the safe use of lasers,” ANSI, 2000.
- [32] F. C. Delori, R. H. Webb, and D. H. Sliney, “Maximum permissible exposures for ocular safety (ANSI 2000), with emphasis on ophthalmic devices,” *Journal of the Optical Society of America*, vol. 24, pp. 1250–1265, 2007.
- [33] R. Baxter, “Laser safety training manual,” [<http://chemistry.uchicago.edu/safety/LaserSafety.pdf>], 2001.
- [34] A. L. Augustoni, “Laser hazard analysis for airborne AURA (big sky variant) proteus platform,” SAND2004-0413, Sandia National Laboratories, 2004.
- [35] V. V. Zavyalov, C. C. Marchant, G. E. Bingham, T. D. Wilkerson, J. L. Hatfield, R. S. Martin, P. J. Silva, K. D. Moore, J. Swasey, D. J. Ahlstrom, and T. L. Jones, “Aglite lidar: Calibration and retrievals of well characterized aerosols from agricultural operations using a three-wavelength elastic lidar,” *Journal of Applied Remote Sensing*, vol. 3, p. 033522, 2009.
- [36] R. M. Measures, *Laser Remote Sensing: Fundamentals and Applications*. New York: John Wiley, Inc., 1984.
- [37] S. W. Dho, Y. J. Park, and H. J. Kong, “Experimental determination of a geometrical form factor in a lidar equation for an inhomogeneous atmosphere,” *Applied Optics*, vol. 36, pp. 6009–6010, 1997.
- [38] J. D. Klett, “Extinction boundary value algorithms for lidar inversion,” *Applied Optics Letters*, vol. 22, pp. 514–515, 1983.
- [39] A. S. Jursa, *Handbook of Geophysics and the Space Environment*, Air Force Geophysics Laboratory, Hanscom Air Force Base, 1985.
- [40] E. Mallard and H. L. L. Chatelier, “On the propagation velocity of burning in gaseous explosive mixtures,” *Comptes-rendus Hebdomadaires des Séances de l’Académie des Sciences de Paris*, vol. 93, p. 145, 1881.
- [41] H. B. Dixon, “On the movement of the flame in the explosions of gases,” *Philosophical Transactions of the Royal Society of London*, vol. A200, pp. 315–352, 1903.
- [42] B. Lewis and G. von Elbe, *Combustion, Flames and Explosions of Gases*. New York - London: Academic Press, 1951.
- [43] O. Laporte and T. D. Wilkerson, “Hydrodynamic aspects of shock tube spectroscopy,” *Journal of the Optical Society of America*, vol. 50, pp. 1293–1299, 1960.

- [44] R. B. Stull, *An Introduction to Boundary Layer Meteorology*. Netherlands: Kluwer Academic Publishers, 1998.
- [45] J. C. Kaimal and J. A. Businger, “Case studies of a convective plume and a dust devil,” *Journal of Applied Meteorology*, vol. 9, pp. 612–620, 1970.
- [46] J. M. Wilczak and J. E. Tillman, “The three-dimentional structure of convection in the atmospheric surface layer,” *Journal of Atmospheric Science*, vol. 37, pp. 2424–2443, 1980.
- [47] J. M. Wilczak and J. A. Businger, “Thermally indirect motions in the convective atmospheric boundary layer,” *Journal of Atmospheric Science*, vol. 40, pp. 343–358, 1984.
- [48] L. Prandtl, *Führer durch die Strömungslehre*. Braunschweig: Vieweg, 1942.

## Chapter 3

# An Iterative Least Square Approach to Elastic-Lidar Retrievals for Well-Characterized Aerosols<sup>1</sup>

### 3.1 Background

Analytical solutions to the lidar equation have been known for some time. These methods have generally relied on a two-step process: first, convert lidar data into backscatter and extinction values; second, to convert these values into the PSD of the aerosol, from which mass fraction concentration can be calculated. Solutions for calculating backscatter and extinction have included the slope method [1], the ratio constraint methods, including those by Klett [2, 3] and Fernald [4], and EKF methods [5–7]. Many methods for calculating PSDs from optical parameters have been demonstrated using error minimization techniques, with various forms of regularization to stabilize the solution [8–10].

This chapter presents a method of retrieving aerosol concentration from elastic lidar data, which operates by formulating the lidar equation into a novel vector form, linearizing it around some solution value, and computing the least-squares solution. This process is repeated until the solution converges, similar to the Newton-Raphson method. The method is a type of nonlinear least-squares (NLS) solution to the lidar problem. The method requires *a priori* knowledge of backscatter values at a boundary point as well as defined relationships between backscatter, extinction, and mass fraction concentration for all scattering components. An algorithm using this method was validated using both simulated and experimental data.

The ratio constraint methods by Klett and Fernald are analytical solutions to the differential equation form of the lidar equation and have been shown to be mathematically

---

<sup>1</sup>C. C. Marchant, T. K. Moon, J. H. Gunther, “An iterative least square approach to elastic-lidar retrievals for well-characterized aerosols” ©IEEE. Reprinted, with permission, from *IEEE Trans. Geosci. Remote Sens.*, vol. 48, pp. 2430–2444, 2010.

equivalent [3]. These solutions contain a singularity located on the far side of the boundary point. As a result, the retrieved solution is not stable for ranges significantly beyond the boundary point and practical application of these methods require the boundary point to be placed at a range beyond the aerosol target. These methods have widespread use in many lidar systems today [11].

The requirement that the boundary point must be placed beyond the aerosol target is an important characteristic of Klett's method because it directly impacts two major drawbacks of the method [12]. One drawback is that the quality of the lidar return is very dependent on the SNR value at the boundary point. The lidar signal has significantly inferior SNR values at ranges beyond the aerosol target compared to ranges before the target due to the range-squared dependent falloff of the signal. Averaging could reduce the noise at a distant boundary point; however the same averaging could be used to lower the noise at a boundary point located before the aerosol target. As a result, the closer point would still have a better SNR value and it would still be more desirable to place the boundary point before the target aerosol.

Another drawback is that the quality of a lidar return generated by Klett's method is very dependent on the quality of the calibration extinction value chosen for the boundary point. It is common practice with Klett's method to calibrate the lidar in the molecular atmospheric layer above the aerosol boundary layer [13]; however in many circumstances this is not possible. For example, Federal Aviation Administration regulations limit the power of lasers that may be pointed vertically, particularly in sensitive airspace near airports. In this case, a horizontally operating lidar would be able to operate pointing parallel to the ground, but would not be allowed to point vertically to calibrate using the molecular atmospheric layer. Alternatively, a lidar with a relatively short effective operating range, such as a low-power micro-pulse lidar, might have insufficient power to reach an altitude where molecular scattering dominates with sufficient SNR. The Aglite lidar instrument [14] has faced both of the situations described above in field campaigns.

If the boundary point can be placed at relatively close range to the instrument, an

alternative means can be used to calibrate the lidar. As illustrated in fig. 3.1, a point-sensor instrument for measuring backscatter can be positioned at relatively close range where the SNR is relatively high. The lidar beam can shine past this point and the boundary point placed at this location.

In addition to the requirement of boundary point placement, Klett's method does not account for the noise levels of the different channels or the relationships between the channels when calculating backscatter and extinction. Although the formulation does not explicitly require it, practical application of Klett's solution for two scatterers requires that a constant lidar ratio for the non-homogeneous component be assumed for each individual wavelength. As a result, the method retrieves backscatter (or alternatively extinction) as a function of range for each wavelength.

Different versions of the EKF have also been applied to the lidar inversion problem. By updating a state space vector with sequential observations, the EKF generates a weighted least-squares estimate of the state using *a priori* information from the previous measurements. Rocadenbosch's formulation of the EKF returns a state-vector containing backscatter and lidar ratio values as a function of range, at the expense of spatial resolution, for individual channels [5]. Further computations must still be performed to convert these optical parameters to aerosol concentration and other physical parameters.

Alternatively, Warren's formulation of the EKF uses a two step process, where a maximum-likelihood estimator first estimates the aerosol type, and then a Kalman filter is used to estimate aerosol concentration. Warren's formulation linearizes the filter by assuming an optically thin aerosol and dropping the extinction expression, limiting the versatility of this formulation [6].

Dias presents a solution to the lidar equation in the form of an extended Kalman fixed-interval smoother [7]. In this formulation, the state vector is composed of the extinction coefficient of the current range and the optical thickness of the path up to and including the current range. The updated state equation is a function of the state at the previous range in the current measurement. This formulation offers the significant advantages of being both

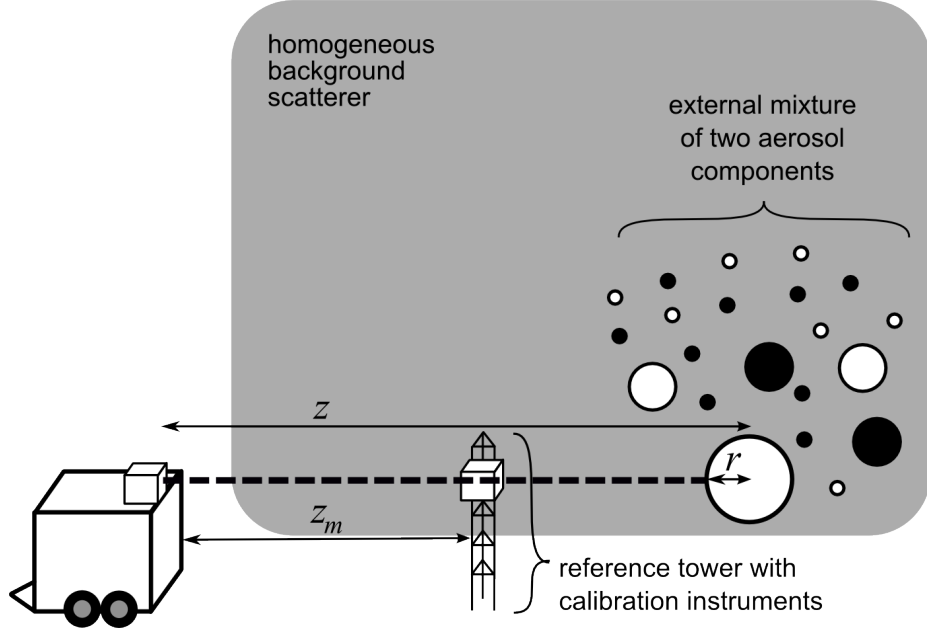


Fig. 3.1: Illustration of Aglite measuring an atmosphere that consists of a baseline component plus a mixture of varying components.

computationally efficient and giving stable performance under noisy conditions.

It is convenient to divide the atmosphere into a baseline and a varying component. Similar to Klett's solution for two scatterers, the iterative least-squares method formulates the lidar equation as a baseline background scatterer plus a non-homogeneous mixture composed of one or more varying aerosol components. The method assumes that the extinction/backscatter ratios of these individual mixture components at all wavelengths are constant over the range of the signal and that only the amplitudes of the individual components vary. This assumption may seem unrealistic for many circumstances, as aerosols often have spatially varying characteristics. However by approximating an aerosol as an external mixture of aerosol components, the aggregate characteristics of the aerosol are free to vary with range, even though the characteristics of individual components are constant. Another similarity with Klett's method is that the formulation given here also requires a boundary point. This boundary point calibrates the signal and allows the retrieval to work even in situations with relatively low SNR values.

Unlike other lidar retrieval methods that typically give results in the form of optical

parameter values, the method presented here returns amplitude values of the individual mixture components. If the mass fraction values of the component aerosols are also known, it is straightforward to calculate the total mass fraction values of the atmosphere by multiplying the amplitudes of the individual components by their corresponding individual mass fraction values and summing them. If the PSDs of the individual components are also known, the PSD of the aggregate aerosol mixture can be easily calculated as a linear combination of the PSDs of the individual components.

One advantage of this formulation is that it is straightforward to deal with multi-wavelength data. It is simply necessary to describe the optical parameters for each mixture component at every wavelength, and it is possible to retrieve mixture component amplitudes as long as the number of components is less than or equal to the number of channels. Because each component has backscatter and extinction coefficient values for each channel, the method takes full advantage of knowledge of the relationships between the different channels.

For a given wavelength, the lidar equation is under-determined, where the equation for returned power depends on coefficients for both extinction and backscatter. If the assumption is made that the atmosphere consists a well-characterized baseline component plus a well-characterized varying component, the lidar equation can be formulated as a one-to-one mapping, similar to Klett's method. For a multi-channel lidar, the atmosphere can be modeled using as many scattering components as channels. As a result, the method can be used with an arbitrary number of channels, ensuring that the retrieved solution is consistent across all channels.

The iterative least-squares method works by calculating the least-squares solution to the lidar equation consistent with a given set of constraints. The lidar equation is iteratively linearized using a first-order Taylor series expansion and minimized using the weighted least-squares solution until the solution converges. In the presence of Gaussian noise, if the correct weighting matrix is selected, this estimator approximates a maximum-likelihood estimator. The method is presented simply in the context of a least-squares estimator of

the atmospheric state at a single moment in time, not using any information from prior or future measurements. In addition to the current measured signal, an EKF also takes into account all information from past measurements and returns a solution based on all measurements. It would be a straightforward task to incorporate the method described in this paper into an EKF by choosing state-space equations that use the same state vector formulation described below and by substituting the linearized form of the lidar equation described below for the observation equation of the EKF.

### 3.2 Well Characterized Local Aerosol

For an elastic lidar with  $\Lambda$  channels, the vector form of the lidar equation can be represented by (3.1).

$$\mathbf{p}(z) = \mathbf{k} \cdot \mathbf{g}(z) \cdot \frac{\boldsymbol{\beta}(z)}{z^2} \cdot \exp\left(-2 \int_0^z \boldsymbol{\alpha}(z') dz'\right) \quad (3.1)$$

The bold expressions in (3.1) are all  $\Lambda \times 1$  vectors, whose elements correspond to the lidar detector channels. The variable  $z$  represents range [m], the expression  $\mathbf{p}(z)$  has units of power [W], the function  $\mathbf{g}(z)$  represents the attenuation (unitless) due to the GFF at range  $z$ , and  $\boldsymbol{\alpha}(z)$  [ $m^{-1}$ ] and  $\boldsymbol{\beta}(z)$  [ $m^{-1} \cdot sr^{-1}$ ] represent total backscatter and extinction coefficients as a function of range, respectively [15]. The exponential expression represents attenuation due to extinction. The operator  $\cdot$  represents element-by-element multiplication and the exponent function operates on an element-by-element basis. The vector  $\mathbf{k}$  is defined as by (3.2).

$$\mathbf{k} = (c\tau/2) A \mathbf{p}_0 \cdot \mathbf{x} \quad (3.2)$$

The term  $\mathbf{k}$  has units [W·m<sup>3</sup>·sr],  $c$  is the speed of light [m/s] vector,  $\tau$  is the detection window length [s], the vector  $\mathbf{p}_0$  is the power per channel [W],  $A$  is the receiver area [m<sup>2</sup>], the vector  $\mathbf{x}$  (unitless) is the combined transmitter and receiver efficiencies.

The geometric form factor can be removed from (3.1) in pre-processing if the form of

$\mathbf{g}(z)$  is known, or if  $z$  is sufficiently large that  $\mathbf{g}(z)$  can be approximated as unity. In this case, the relationship between  $\mathbf{k}$  and the backscatter at some boundary point  $m$  can be expressed by (3.3).

$$\mathbf{k} = \frac{\mathbf{p}_m z_m^2}{\beta_m \cdot \exp \left( -2 \int_0^{z_m} \boldsymbol{\alpha}(z') dz' \right)} \quad (3.3)$$

If a lidar is calibrated (i.e.  $\mathbf{k}$  is known) and if the exponential term is close to unity, then the boundary value  $\beta_m$  is known. Alternatively,  $\beta_m$  can be obtained from another source such as in-situ instruments or an atmospheric model, and be used to calculate  $\mathbf{k}$ . In any case, the formulation of (3.3) assumes that  $\mathbf{k}$  is constant, not dependent at all on the magnitude of the received power. This requires an optical detector with a linear response. For example, the Aglite lidar instrument [14] uses PMTs and an APD, all in photon counting mode, and as a result the instrument has a highly linear detector response on each channel for low to moderate numbers of received photons. For very large numbers of photons, the nonlinear response of photon-counting detectors can be well modeled mathematically and processing of the lidar signal can correct for the nonlinear response. For the case of detectors with nonlinear response, such as PMTs in current mode, characterization of the detector response is required and the lidar signals must be processed to remove the nonlinear effects before retrievals may be performed.

It is assumed that the PSD of a well characterized (i.e. well mixed) scatterer can be described as a so-called external mixture, or linear combination, of  $S$  scattering components plus a baseline component (which can have zero amplitude) that is constant with range, where  $S \leq \Lambda$  in order to avoid an under-constrained system of equations. This is illustrated in fig. 3.1, which illustrates a typical setup using the Aglite lidar instrument. For aerosol scatterers, the PSD as a function of range can then be described by (3.4).

$$n(r, z) = n_0(r) + \sum_{i=1}^S n_i(z) \tilde{n}_i(r) \quad (3.4)$$

The variable  $r$  represents the particle's optical radius [ $\mu\text{m}$ ],  $n_0(r)$  is the PSD [ $\#\cdot\text{m}^{-3}$ ].

$\mu\text{m}^{-1}$ ] of the homogeneous component,  $\tilde{n}_i(r)$  is the  $i$ th PSD [ $\text{m}^{-3} \cdot \mu\text{m}^{-1}$ ], and  $n_i(z)$  [#] is the amplitude of the  $i$ th component.

The choice of functions for the PSDs of the  $S$  non-baseline scattering components in (3.4) has a significant impact on the solution to the lidar equation. These functions are a basis of the vector space representing the PSD. These functions must be linearly independent; however it is not necessary that they be either orthogonal or normal. In addition, each function has a corresponding vector of backscatter coefficients, and these backscatter vectors must be linearly independent. In fact, because a linearly dependent set of PSD functions cannot generate a linearly independent set of backscatter vectors, it is sufficient for the backscatter vectors to be linearly independent to guarantee that the PSDs are independent [16]. Ultimately, the proper selection of these functions is situation dependent, but in general they should be chosen in such a way that they are able to approximate the expected shape of the true PSD of the atmosphere.

Throughout this paper the subscript 0 is used to denote the baseline component of the atmosphere, including both molecular Rayleigh scattering plus residual scattering from baseline background aerosols. Let the vector  $\mathbf{v}(z)$  be the vector of the amplitudes of all of the non-baseline components, as shown by (3.5).

$$\mathbf{v}(z) = \begin{bmatrix} n_1(z) & n_2(z) & \dots & n_S(z) \end{bmatrix}^T \quad (3.5)$$

For each component  $\tilde{n}_i(r)$ , there is a corresponding extinction, backscatter, and mass fraction vector. Backscatter and extinction values due to molecular scattering can be calculated using Rayleigh theory with measurements of temperature, pressure, and relative humidity [17]. Given an individual component PSD  $\tilde{n}_i(r)$  and complex index of refraction  $m_j$  for wavelength  $\lambda_j$  and assuming spherical particles, Mie theory can be used to calculate backscatter and extinction coefficients [18]. Assuming that the aerodynamic radius equals the optical radius and the aerosol density is already known (it may be convenient to assume  $\rho = 1$ ), the PSD of the scattering component can also be used to calculate mass fraction values for the individual components. The expression here for mass fraction concentration,

also called particulate matter, is  $PM_D$ , which is defined as the total mass of particles in a cubic meter of air [ $\mu\text{g}\cdot\text{m}^{-3}$ ] with an aerodynamic diameter less than  $D$ . Assuming spherical particles, the equations for extinction  $\alpha_\lambda$  [ $\text{m}^{-1}$ ], backscatter  $\beta_\lambda$  [ $\text{m}^{-1}\cdot\text{sr}^{-1}$ ], and mass fraction concentration  $PM_D$  [ $\mu\text{g}\cdot\text{m}^{-3}$ ] of an individual component  $\tilde{n}_i(r)$  for a given wavelength  $\lambda_j$  are given by (3.6).

$$\begin{aligned}\alpha_i(\lambda_j) &= \pi \int_0^\infty r^2 Q_{ext}(k_j, r, m_j) \tilde{n}_i(r) dr \\ \beta_i(\lambda_j) &= \frac{1}{4} \int_0^\infty r^2 Q_{pi}(k_j, r, m_j) \tilde{n}_i(r) dr \\ PM_{i,D} &= \frac{4}{3} \pi \rho_i \int_0^{D/2} r^3 \tilde{n}_i(r) dr\end{aligned}\quad (3.6)$$

The variable  $k$  is the size parameter  $k_j = 2\pi/\lambda_j$ . The expressions  $Q_{ext}$  and  $Q_{pi}$  are the scattering efficiency functions for extinction and backscatter, respectively.

Since the atmosphere at any given range can be described as a homogeneous baseline scattering component plus a linear combination of other varying scattering components, the total extinction, backscatter, and mass fraction vectors can be written in matrix form as shown in (3.7).

$$\begin{aligned}\boldsymbol{\alpha}(z) &= \boldsymbol{\alpha}_0 + A\mathbf{v}(z) \\ \boldsymbol{\beta}(z) &= \boldsymbol{\beta}_0 + B\mathbf{v}(z) \\ \mathbf{pm}(z) &= \mathbf{pm}_0 + M_{PM}\mathbf{v}(z)\end{aligned}\quad (3.7)$$

The column vectors of the matrices  $A$ ,  $B$ , and  $M_{PM}$  are the extinction, backscatter, and PM vectors for the individual scattering components. These column vectors can be calculated using Mie theory as described by (3.6), or can be taken from some other source. As mentioned previously, the PSDs of the non-baseline aerosol components must be chosen so that the corresponding backscatter vectors are linearly independent. As a consequence,  $B$  must be full column rank. The expression  $\mathbf{pm}$  represents the mass fraction vector. Government air-quality regulations typically regulate  $PM_{2.5}$  and  $PM_{10}$ , so a convenient formulation for  $\mathbf{pm}$  might be (3.8).

$$\mathbf{pm} = \begin{bmatrix} PM_{2.5}(z) & PM_{10}(z) \end{bmatrix}^T \quad (3.8)$$

The vectors  $\boldsymbol{\alpha}$ ,  $\boldsymbol{\alpha}_0$ ,  $\boldsymbol{\beta}$ , and  $\boldsymbol{\beta}_0$  are  $\Lambda \times 1$  elements, the vector  $\mathbf{v}$  is  $S \times 1$  elements, and the matrices  $A$  and  $B$  are  $\Lambda \times S$ . Following the form shown in (3.8),  $\mathbf{pm}$  and  $\mathbf{pm}_0$  are  $2 \times 1$ , and  $M_{PM}$  is  $2 \times S$ . The values of these vectors and matrices might be determined from an aerosol database, atmospheric model, or using independent point sensors. In this way, extinction, backscatter, and mass fraction can be described as linear functions of the vector  $\mathbf{v}(z)$ , which represents the amplitudes of each of the component scatterers at range  $z$ .

### 3.3 State Vector Formulation

The lidar equation can be rewritten in terms of  $\boldsymbol{\beta}_m$  by substituting (3.3) into (3.1).

$$\mathbf{p}(z) = \mathbf{p}_m \cdot \frac{z_m^2 \boldsymbol{\beta}(z)}{z^2 \boldsymbol{\beta}_m} \cdot \exp \left( -2 \int_{z_m}^z \boldsymbol{\alpha}(z') dz' \right) \quad (3.9)$$

Substituting (3.7) into (3.9) results in (3.10).

$$\mathbf{p}(z) = \mathbf{p}_m \cdot \frac{z_m^2 (\boldsymbol{\beta}_0 + B\mathbf{v}(z))}{z^2 \boldsymbol{\beta}_m} \cdot \exp \left( -2 \int_{z_m}^z (\boldsymbol{\alpha}_0 + A\mathbf{v}(z')) dz' \right) \quad (3.10)$$

At this point, the lidar equation for a given range has been reduced to set of  $\Lambda$  equations with  $S$  unknowns, which are the amplitudes of  $n_i(z)$ , the PSDs of the individual components.

In practice, any lidar signal will have error. Possible sources of error in a lidar system include photo-induced shot noise from the background radiance and the returned lidar-signal itself, shot dark current noise, and thermal noise. Additionally, non-uniform detector response and laser source power fluctuations can be another source of error. If the error is assumed to be a zero-mean random variable, then the measured signal can be expressed by adding the error term  $\boldsymbol{\nu}_z$  to (3.10), which is a zero-mean random vector for range  $z$ .

$$\mathbf{p}(z) = \mathbf{p}_m \cdot \frac{z_m^2 (\beta_0 + B\mathbf{v}(z))}{z^2 \beta_m} \cdot \exp \left( -2 \int_{z_m}^z (\alpha_0 + A\mathbf{v}(z')) dz' \right) + \nu_z \quad (3.11)$$

Let the matrix  $U$  be defined as a matrix whose  $i$ th column vector is  $\mathbf{v}(z_i)$ . For a lidar with  $L$  range values,  $U$  is a  $S \times L$  matrix.

$$U = \begin{bmatrix} n_1(z_1) & n_1(z_2) & \cdots & n_1(z_L) \\ n_2(z_1) & n_2(z_2) & \cdots & n_2(z_L) \\ \vdots & \vdots & \ddots & \vdots \\ n_S(z_1) & n_S(z_2) & \cdots & n_S(z_L) \end{bmatrix}^T \quad (3.12)$$

Let  $P(U)$  be defined as a function of  $U$  that returns an  $\Lambda \times L$  matrix whose  $i$ th column vector is  $\mathbf{p}(z_i)$ . This matrix is the estimate of what the returned lidar signal should be given  $U$ . In this case, the least-squares solution to the lidar equation is the value for an estimate of the matrix  $U$  that minimizes the squared difference between the measured power and its estimate.

$$\hat{U} = \arg \min_U |P(U) - P_{meas}|^2 \quad (3.13)$$

Both  $P_{meas}$  and  $P(U)$  are matrices, and it is convenient to vectorize them. Let  $\mathbf{y} = \text{vec}(U)$ ,  $\mathbf{q} = \text{vec}(P_{meas})$ , and  $\hat{\mathbf{q}}(y) = \text{vec}(P(U))$ . The vector  $\mathbf{y}$  is  $SL \times 1$  and the vector  $\mathbf{q}$  is  $\Lambda L \times 1$ . In this case the vectorized form of (3.13) becomes (3.14).

$$\hat{\mathbf{y}} = \arg \min_{\mathbf{y}} |\hat{\mathbf{q}}(\mathbf{y}) - \mathbf{q}|^2 \quad (3.14)$$

The structure of  $\mathbf{y}$  is given by (3.15).

$$\hat{\mathbf{y}} = \begin{bmatrix} n_{1,1} & n_{2,1} & \cdots & n_{S,1} & n_{1,2} & \cdots & n_{S,L} \end{bmatrix}^T \quad (3.15)$$

The norm is defined using a weighted Euclidean inner product  $|A|^2 = A^T W A$ . If  $W$  is

chosen to be the inverse of the measurement covariance matrix, the least-squares solution to (3.14) will in fact be the maximum-likelihood solution to the lidar equation for the case of Gaussian noise [16].

At this point, a state vector given by (3.15) describes the aerosol concentration of the atmosphere and the lidar retrieval problem can be restated in terms of finding the weighted least-squares solution to this state-vector.

### 3.4 Linearization

Since the form of (3.11) is nonlinear,  $\hat{\mathbf{q}}(\mathbf{y})$  is also nonlinear. Nevertheless, a solution to (3.14) can still be calculated by iteratively linearizing and solving, similar to Newton's method. The details of applying this method to the lidar equation are presented here. The function  $\hat{\mathbf{q}}(\mathbf{y})$  and all of its component matrices can be expressed by (3.16).

$$\hat{\mathbf{q}}(\mathbf{y}) = (B'\hat{\mathbf{y}} + \mathbf{b}_0) \cdot \exp(A'\hat{\mathbf{y}} + \mathbf{a}_0) \quad (3.16)$$

Full details on how to construct the matrices  $A'$  and  $B'$  and vectors  $\mathbf{a}_0$  and  $\mathbf{b}_0$  are given in Appendix A.

A linear approximation of (3.16) around some point  $\hat{\mathbf{y}}_0$  can be made by expanding it into a Taylor series and discarding all but the terms up to the first order. Examples of how to expand exponential matrix expressions are given in Appendix A. In general, the form of a first order Taylor series approximation of a vector function around the point  $\mathbf{x}_0$  is shown below.

$$f(\mathbf{x}_0) \approx f(\mathbf{x}_0) + \frac{df(\mathbf{x}_0)}{d\mathbf{x}} (\mathbf{x} - \mathbf{x}_0) \quad (3.17)$$

Using (3.17), it is possible to approximate (3.16) with a linear expression with the same value and first derivative at the point  $\mathbf{y}_0$ .

$$\begin{aligned}
\hat{\mathbf{q}} &\approx G\hat{\mathbf{y}} + \mathbf{h} \\
G &= \text{diag} [\exp (A'\hat{\mathbf{y}}_0 + \mathbf{d})] [B' + \text{diag} (B'\hat{\mathbf{y}}_0) A' + \text{diag} (\mathbf{b})] \\
h &= \text{diag} [\exp (A'\hat{\mathbf{y}}_0 + \mathbf{d})] [\text{diag} (\mathbf{b}) (1 - A'\hat{\mathbf{y}}_0) - \text{diag} (B'(\hat{\mathbf{y}})_0) A'\hat{\mathbf{y}}_0]
\end{aligned} \tag{3.18}$$

The dimensions of  $G$  are  $\Lambda L \times LS$  and  $\mathbf{h}$  is  $\Lambda L \times 1$ . Given an initial estimate  $\hat{\mathbf{y}}_0$ , the linear approximation to the minimum weighted least-squares solution of (3.16) can now be written as shown in (3.19).

$$\hat{\mathbf{y}} = (G^T W G)^{-1} G^T W (\mathbf{q} - \mathbf{h}) \tag{3.19}$$

Assuming there is no correlation between channels or ranges, the appropriate choice for the best linear unbiased estimator is for  $W$  to be a diagonal matrix of matrices that weights each element of  $\mathbf{y}$  by the inverse of its variance, or in other words  $W^{-1}$  is the noise covariance matrix of measured power vector described by (3.11) [16].

$$\begin{aligned}
W &= \text{diag} \left[ \begin{array}{ccc} W_1 & \dots & W_\Lambda \end{array} \right] \\
W_i &= \text{diag} \left[ \begin{array}{ccc} 1/\sigma_{1,i}^2 & \dots & 1/\sigma_{L,i}^2 \end{array} \right]
\end{aligned} \tag{3.20}$$

The expression  $\sigma_{h,i}^2$  represents the observation noise variance [ $\text{W}^2$ ] at range  $z_h$  for the  $i$ th channel. There is no universal method of how to determine the variance for a given range and channel as this depends on the characteristics of the instrument, however for the case of the simulated lidar data and Aglite lidar data described later in this paper, the return signal was Poisson distributed so the variance was estimated by time-averaging the signal and fitting each channel with a curve described by  $Az^{-2}$ , and then assuming that the variance for each channel was equal to  $Az^{-2}$ .

Computer simulations have demonstrated that this retrieval method behaves correctly as the SNR falls below 0 dB. Examples of simulated one-second return-power signals (symbols) are shown in figs. 3.2(a,c,e), compared with estimated return-power signals according to the NLS estimator (lines), which they match very well. Inspection of figs. 3.2(b,d,f) shows that

estimated concentration remains roughly centered around the simulated values at farther ranges, but with progressively increasing error. Although it is unrealistic to expect arbitrarily accurate retrievals as the SNR approaches 0 dB, it is reasonable to expect the retrieval to fail gracefully. This means one can expect the algorithm to continue to deliver useful results with zero-mean distributed solution error as the SNR goes to 0 dB. Whereas the SNR of the returned signal is inversely related to the range of the signal, the weighting coefficients in (3.20) are not. In fact, for the case of shot noise, both the variance and expected power of the signal decrease with increasing range. Therefore, according to (3.20), the weighting coefficients increase as range increases. Consequently, although closer signals have relatively more influence on the solution because of their higher amplitudes, the weighting coefficients give farther range signals sufficient importance so that their information is correctly incorporated into the solution. Although shot noise is Poisson distributed, due to the central limit theorem it is reasonable to approximate it as Gaussian noise, where the variance equals the mean.

As the approximate solution approaches the true solution, the linear approximation more closely approximates the lidar equation and returns a progressively better solution. In turn, the improved solution allows for a better linear approximation of the lidar equation. In this way the retrieved solution converges to the true solution.

The computational cost of each iteration is not trivial, as the matrix  $G$  can be quite large. The main computational expense lies in computing the matrix multiplications and matrix inverse from (3.19). Consider the matrix  $G$ , which has dimensions  $\Lambda L \times LS$ . A 500 bin long 3-channel lidar signal, retrieved for two aerosol components, would require  $G$  to be 1500x1000, meaning computation of (3.19) requires the inversion of a 1000x1000 matrix. This computation is readily achieved using modern computing power, however since Gaussian elimination has a computational complexity bound of  $O(n^3)$ , it may be prohibitive to use this method with significantly longer lidar signals.

Computational costs can be mitigated by restricting the retrieval to the region of interest in the signal. An additional strategy to reduce computational costs and also to constrain the

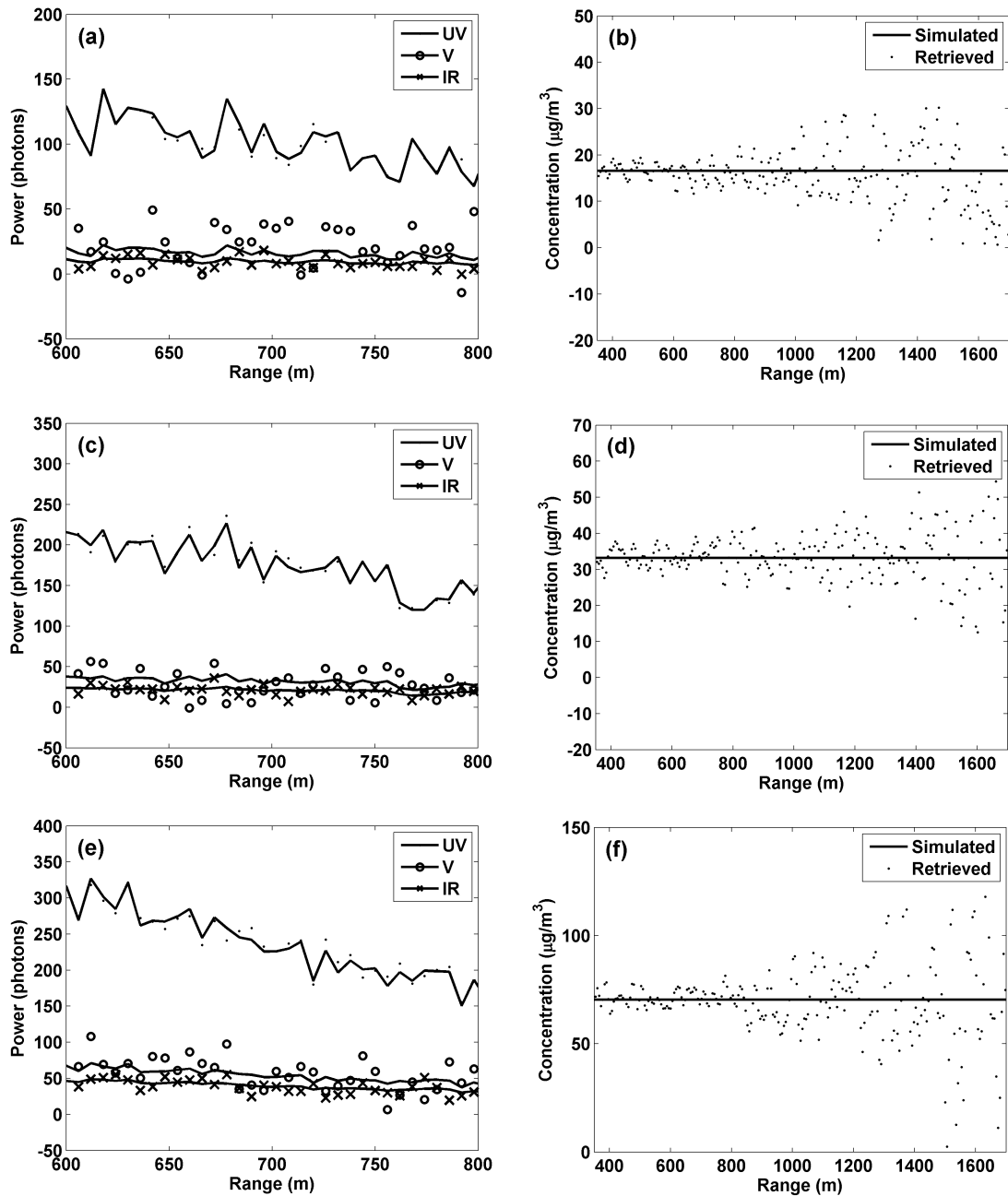


Fig. 3.2: Comparison of synthesized data with the estimated solution for measured power (left column) and  $\text{PM}_{10}$  concentration (right column) of (a,b) average continental, (c,d) polluted continental, and (e,f) urban type homogeneous atmospheres.

solution would be the use of a regularization matrix. Since a detailed investigation of lidar signal regularization is beyond the scope of this paper, a couple of comments on the topic should be made. Warren et al. have previously demonstrated regularization in retrieving lidar signals, decomposing the state vector into a reduced set of sinusoidal basis functions [6], while the use of regularization to constrain PSDs retrieved from multi-wavelength extinction and backscatter measurements have been demonstrated [8–10]. Regularization could be incorporated into the algorithm described here by substituting the state vector with a reduced state vector.

$$\hat{\mathbf{y}} = R\hat{\mathbf{y}}' \quad (3.21)$$

The matrix  $R$  is the  $SL \times TL$  regularization matrix and  $\hat{\mathbf{y}}'$  is the  $TL \times 1$  reduced state vector to be used in place of  $\hat{\mathbf{y}}$ . The regularization matrix decomposes the state into a reduced set of  $T$  basis functions, where  $T < S$ . As a result, the size of the state vector is reduced, along with the cost of matrix inversion, which reduces from inverting an  $LS \times LS$  matrix to a smaller  $LT \times LT$  matrix.

In summary, a flowchart of the algorithm is illustrated in fig. 3.3, and the steps of the lidar retrieval are described as follows:

1. Initialize  $\hat{\mathbf{y}}_0 = 0$ ,
2. Linearize the lidar equation around  $\hat{\mathbf{y}}_0$  using (3.18),
3. Calculate  $\hat{\mathbf{y}}_i$  using (3.19),

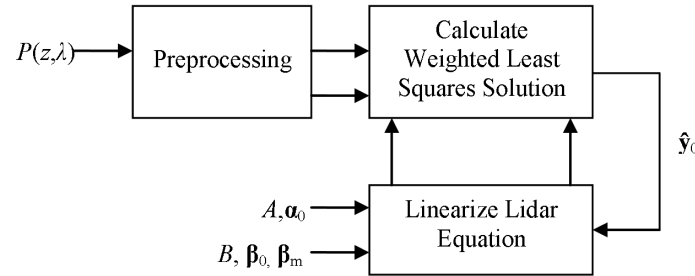


Fig. 3.3: Flowchart illustrating the operation of the iterative least-squares method.

4. Update  $\hat{y}_0 = \hat{y}_0 + \hat{y}_i$ ,
5. Repeat steps 2 through 4 until  $\hat{y}_0$  converges.

### 3.5 Laser Pulse Shape and Geometric Form Factor

The laser pulse shape and range resolution can have an appreciable effect on the lidar data. The form of (3.1) is derived for a laser with a delta-function pulse shape and continuous range measurement. In practice, the laser pulse shape can have significant width and the measured lidar signal is integrated over a certain detection window length  $\tau$ . As a result, the measured lidar signal is the convolution of the lidar function (3.1) with the laser pulse shape and with an integrating window, a rectangle function with width  $c\tau/2$ . Previous work has shown how to deconvolve the laser pulse shape from lidar data using a Wiener filter [6].

A unique way of compensating for the convolution effect of the lidar pulse shape is presented here, which works by incorporating the convolution phenomenon into the lidar equation. Convolution is a linear function, so it can be represented as a matrix multiplication and appended to (3.16). In this way, the deconvolution of the laser pulse with the lidar signal is not explicitly computed, but rather the solution is computed so as to compensate for the convolution. This is very similar to the operation of a zero-forcing equalizing filter [19]. Zero-forcing filters often amplify stop-band noise, so it may be necessary to filter the solution with a low-pass filter to control this noise. It is beyond the scope of this paper to investigate the optimality of this method or compare it to other methods such as the Wiener filter, but it is presented here simply to demonstrate the ability of the iterative least-squares method to integrate this technique.

As an example of a real lidar system, the laser pulse shapes and detection time window for Aglite are illustrated in fig. 3.4(a). The detection time window is a rectangle function, whose width equals the range resolution of the lidar. The actual measured lidar signal is (3.1) convolved with both the laser pulse shape and the detection time window. The laser pulse shape and detection time window can be combined and treated as a low-pass filter. The frequency responses for each channel of Aglite are shown in fig. 3.4(b) with units of

power decibels. The 3 dB point with the lowest frequency of all three channels is at .034 m<sup>-1</sup>, corresponding to an equivalent spatial resolution of 29.4 m for the IR channel (further details of the Aglite lidar are given by Marchant et al. [14]).

It is straightforward to incorporate this filtering effect into the retrieval algorithm. The action of convolution can be represented as multiplication by the matrix  $F$ .

$$\begin{aligned} F &= \text{diag} \left[ \begin{array}{ccc} F_1 & \dots & F_\Lambda \end{array} \right] \\ F_j &= \text{diag} \left[ \begin{array}{cccc} \mathbf{f}_{1,j} & \mathbf{f}_{2,j} & \dots & \mathbf{f}_{L,j} \end{array} \right] \end{aligned} \quad (3.22)$$

The vector  $\mathbf{f}_{h,j}$  is an  $L \times 1$  vector containing the time-reversed convolved pulse shape and measurement window of the  $j$ th channel, as illustrated in fig. 3.4(a), which has been shifted down by  $h-1$  elements, where  $h$  is the column of  $F_j$ . The expression  $L$  is the length of the laser pulse in bins. The filter matrix  $F$  can be attached to (3.16).

$$\hat{\mathbf{q}} = F (A' \hat{\mathbf{y}} + \mathbf{b}) \cdot \exp(C' \hat{\mathbf{y}} + \mathbf{d}) \quad (3.23)$$

The rest of the procedure described in Section 3.5 can then be followed to achieve a retrieval which takes into account the channel-dependent filtering effects of the lidar pulse shape and measurement window.

In addition to lidar pulse shape and windowing effects, the effect of the GFF can also be easily incorporated into  $F$ . The GFF can be calculated [15]; however there can be large discrepancies between the expected and actual shape of the GFF due to misalignment or inaccurate knowledge of the lidar optics parameters, such as the laser divergence angle and beam profile shape. As a result, the GFF may need to be experimentally measured [20]. Normally it is desirable to take measurements in the region of the lidar signal where the GFF is constant, however in some aerosol lidar applications it may be unavoidable to use a region where the GFF has a significant impact on the shape of the return signal [21]. For the case of the experimental data described in Section 3.8, the Aglite instrument was placed 650 m away from the emission source. This location was imposed by the geography of the facility; a more distant location for the lidar was logically impractical. At 650 m, the GFF

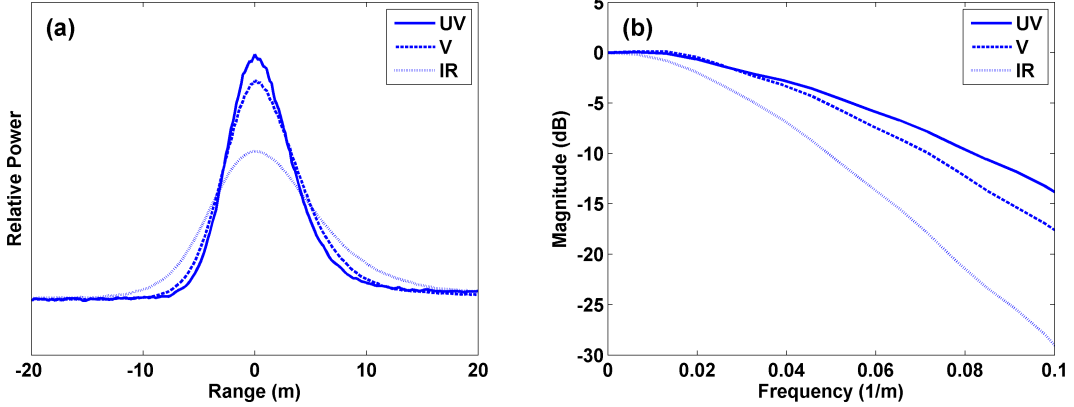


Fig. 3.4: (a) Laser pulse shape convolved with the integration window, and (b) its frequency response.

of Aglite is only approximately 80% of its far-field value, so it was necessary to compensate for this effect in the retrieval [14].

Inserting  $F$  into the lidar equation requires multiplying a  $\Lambda L \times \Lambda L$  matrix with a  $\Lambda L \times SL$  matrix. If a series of lidar retrievals are made, where identical values for  $A$  and  $\mathbf{b}$  will be used for every retrieval and the laser pulse shape and GFF are constant in time,  $A$  and  $\mathbf{b}$  only need to be multiplied by  $F$  once. The convolution will be then be compensated automatically at no additional cost as part of the retrieval for every measurement in the time series.

### 3.6 Solution Error

There are two main assumptions in the retrieval process. The first is that the aerosol is well-characterized, or in other words, extinction and backscatter coefficients must be known for the baseline aerosol, at the boundary point, and for each non-homogeneous component aerosol, as previously described by (3.7). These might come from a database or from in-situ instrument measurements. Inaccurate values for any of these extinction and backscatter coefficients will lead to systematic errors in the retrieved concentration values.

The second assumption is that the atmosphere under investigation consists of a baseline component plus a number of components whose amplitude is spatially dependent, but whose

other characteristics are uniform in space. The retrieval process uses these components as a set of basis functions to represent the aerosol being measured by the lidar. Error can result if the components are only weakly independent.

In addition to errors related to inaccurate assumptions in the retrieval process, there is also error from the measurement noise of the system. An expression for the covariance of the solution as determined by the covariance of the lidar signal noise is derived here. One intuitively expects that as the SNR of the signal decreases, the variance of the retrieved solution will increase. It is possible to estimate the influence of signal noise on the variance of the retrieved solution.

The solution estimate  $\hat{\mathbf{y}}$  is treated as the sum of the true state vector  $\mathbf{y}$  plus some random variable  $\mathbf{s}$ , modeling the solution error.

$$\hat{\mathbf{y}} = \mathbf{y} + \mathbf{s} \quad (3.24)$$

Inserting (3.24) into the solution (3.19) yields the following expression for the covariance of  $\hat{\mathbf{y}}$ .

$$\text{Cov}(\hat{\mathbf{y}}) = (G^T W G)^{-1} G^T W \text{Cov}(\mathbf{q}) W G (G^T W G)^{-1} \quad (3.25)$$

As demonstrated by (B.8), the total error in  $\mathbf{q}$  is due to both the noise in the lidar calibration, described by (B.7), as well as the observation noise in all range bins of the lidar power signal, described by (B.4). One should not be concerned that the weighting matrix  $W$  depends on the variance of the noise. Because  $W$  depends on an *a priori* estimate of the noise measurement, not on the actual value of a given noise vector, it is permitted to come outside of the covariance expression. Inspection of (3.25) shows that the covariance of  $\hat{\mathbf{y}}$  is a function of the total-noise covariance matrix. Since the lidar calibration coefficient noise and the individual range bin noise are either independent or sum to zero, the total-noise covariance matrix is the sum of the range bin covariance and the lidar coefficient covariance. The range bin covariance was defined in (3.20) as  $W^{-1}$ . The covariance of the solution error

is shown by (3.26).

$$\begin{aligned}\text{Cov}(\mathbf{q}) &= \text{diag}(\mathbf{h}) \text{Cov}(\mathbf{d}_k) \text{diag}(\mathbf{h}) + W^{-1} \\ \text{Cov}(\mathbf{d}_k) &= \text{diag} \left[ \frac{\sigma_{m,1}^2}{P_{m,1}^2} \mathbf{1} \quad \frac{\sigma_{m,2}^2}{P_{m,2}^2} \mathbf{1} \quad \dots \quad \frac{\sigma_{m,\Lambda}^2}{P_{m,\Lambda}^2} \mathbf{1} \right]\end{aligned}\quad (3.26)$$

The expression  $\mathbf{1}$  is an  $L \times L$  submatrix, whose elements are all equal to 1. The derivation of (3.26) is given in Appendix B.

The covariance of the retrieved extinction, backscatter, and mass fraction vectors can be calculated as well. Using (3.7), the covariance matrix of the estimated extinction vector for a given range can be calculated.

$$\text{Cov}([\alpha_1 \ \dots \ \alpha_L]) = \text{diag}[A \ \dots \ A] \text{Cov}(\hat{\mathbf{y}}) [A^T \ A^T \ \dots] \quad (3.27)$$

Similar definitions exist for the covariance of the backscatter and mass fraction vector estimates. The equations above show how to estimate the error of all the retrieval parameters for each bin in the lidar retrieval if the variance of the lidar power signal is already known. In practice, this covariance can only be estimated. Additionally as described in Appendix B, this method assumes  $\hat{\mathbf{y}} = 0$  when estimating the contribution of boundary point noise. This means that the (3.25) returns an estimate of the solution variance, not the actual solution covariance. Nevertheless, since the calculations use estimates of the lidar signal noise and retrieval parameters, the calculated values are as close as could be hoped for and should be sufficiently close to the “true” error to be useful.

### 3.7 Simulations

This section presents the results of validating this method using synthetic data, representing a variety of aerosol loading conditions, while Section 3.8 presents the results of applying this method to experimental data. In all cases, the retrieved values were consistent with the simulated values. The following section presents the results from validating this method with experimental data. Synthetic lidar data were created to simulate a variety of atmospheric conditions. The synthetic lidar data are based on the parameters of the Aglite

lidar instrument [14], which is a micro-pulse lidar that uses photon-counting detection, with channels at 355, 532, and 1064 nm. These were used to test the performance of the retrieval method described above.

The Rayleigh scattering component was calculated corresponding to conditions of 20° C, 50% relative humidity, and barometric pressure of 1013.25 mbar. In addition to Rayleigh scattering, three types of Mie scattering components were simulated. These are the continental average, continental polluted, and urban aerosol mixtures, as described by Hess et al. Backscatter, extinction, PM<sub>2.5</sub>, PM<sub>10</sub>, and total suspended particulate (TSP) were calculated for these scatterers at 50% relative humidity using the OPAC database [22]. These aerosols are summarized in Table 3.1.

Simulated lidar returns were generated for three wavelengths using (3.1). The baseline background component consisted of either continental average or continental polluted aerosols added to the Rayleigh component. Lidar returns were also generated for the same baseline components, but with an added emission plume composed of continental average, continental polluted, or urban aerosol. The emission plume has a Gaussian shape, for which the half-max width of the plume is 131 m, placed at 800 or 1600 m. An integration time of 1 second was used to generate 1000 returns for each scenario. The signal was simulated assuming channel power values of 1.15, 0.85, and 4.10 W, and lidar channel efficiency values of 2.88e-4, 7.71e-5, and 1.03e-5 [unitless] for the 355, 532, and 1064 nm channels, respectively, matching typical values for the Aglite instrument. A noise component was also added to the signal to simulate the effects of solar background radiation with values of 100, 250, and 10 photons per bin, again corresponding to typical values during Aglite operation. The combined noise and signal are then modeled as a Poisson distributed random process.

The algorithm described above in Sections 3.3 and 3.4 was applied to these simulated returns, and the resulting retrievals were evaluated. The range of the boundary point was 600 m in all cases, and baseline backscatter vector that was used to generate the signal was used for the boundary point backscatter vector  $\beta_m$ . The convolution matrix  $F$  described by (3.22) was incorporated into the retrieval to compensate for the laser pulse width and

Table 3.1: Aerosol optical and mass characteristics.

		355 nm	532 nm	1064 nm
Extinction ( $\text{m}^{-1}$ )	Average	9.01e-5	5.26e-5	2.17e-5
	Polluted	2.16e-4	1.24e-4	4.99e-5
	Urban	4.58e-4	2.63e-4	1.10e-4
Backscatter ( $\text{m}^{-1}\text{str}^{-1}$ )	Average	1.56e-6	9.26e-7	4.70e-7
	Polluted	3.61e-6	2.09e-6	9.76e-7
	Urban	7.23e-6	4.22e-6	2.00e-6
Lidar Ratio	Average	57.8	56.8	46.2
	Polluted	59.8	59.3	51.1
	Urban	63.3	62.3	55
		PM <sub>2.5</sub>	PM <sub>10</sub>	TSP
Mass Fraction Concentration ( $\mu\text{g}/\text{m}^3$ )	Average	10.5	16.6	24.2
	Polluted	24.1	33.1	44.6
	Urban	47.8	70.4	99.1

the geometric form factor. A low pass Kaiser-window filter of order 14 with a pass-band cutoff frequency of  $.034 \text{ m}^{-1}$  and a stop-band cutoff frequency of  $.068 \text{ m}^{-1}$  was applied to the solution to compensate for high-frequency noise generated by  $F$ .

### 3.7.1 Background Retrieval

For both the background and plume data sets, the individual solutions were calculated over 1000 individual measurements for four of the synthetic data sets. Figure 3.2 shows examples of individual retrievals performed on synthetic data simulating continental average, continental polluted, and urban atmospheres. Figures 3.2(a,c,e) illustrate a single 1 second return of original signal (minus the solar background component) along with its corresponding minimum least-squares solution, and figs. 3.2(b,d,f) compare the PM<sub>10</sub> concentration of the solution with the original backgrounds.

For these retrievals, a single varying component was used, and the same extinction, backscatter, and mass fraction values were used for the varying component as for the aerosol component of the baseline scatterer. Because the synthetic signal was constructed using

only the baseline aerosol component, the true state vector  $\mathbf{y}$  is the zero-vector.

Inspection of fig. 3.2 confirms that there is no obvious bias in the retrieved signal. Because of the progressively worsening SNR at farther ranges, the estimated aerosol concentration values become noisier, however the retrieved state vector values remains roughly centered around zero. Nevertheless, it is clear that the solution remains stable at distances past the boundary point and the form of the solution is generally consistent with the true state vector. Table 3.2 lists the average error of the retrieved solution compared with the true state vector, as well as the 99% confidence interval.

### 3.7.2 Plume Retrieval

Like the background retrievals, 1000 individual 1-second retrievals were performed, and then averaged. These signals consist of a superposition of the same background aerosol signals used in the background retrievals, with an emission plume added to them, consistent with (3.4). The average of these solutions is computed using both the NLS method described here and Klett's solution for two scatterers [3], with the results compared with the true PM<sub>10</sub> concentration that was used to generate the synthetic data. Klett's solution is computed by applying Klett's method to recover backscatter values, and then a least-squares method is applied to calculate PM<sub>10</sub> concentration [23]. Figures 3.5(a,c,e) clearly illustrates that the signal is the sum of a Gaussian curve shaped emission plume plus a baseline background aerosol.

The mean PM<sub>10</sub> concentration and 99% confidence interval were calculated at 800 and 1600 m ranges for the NLS method and are summarized in Table 3.2. Although the retrieval method clearly introduces some bias, in all cases the average error was on the same order of magnitude as the 99% confidence interval. This bias may be introduced by the low-pass filter that is applied to the solution. No bias is apparent when the low-pass filter is omitted; however the magnitude of the error values increases.

An important benefit of the NLS method is that it is a straightforward process to compute a covariance matrix for the solution. The standard deviation values of the individual PM<sub>10</sub> values, taken as the square root of the diagonal values of the solution covariance matrix,

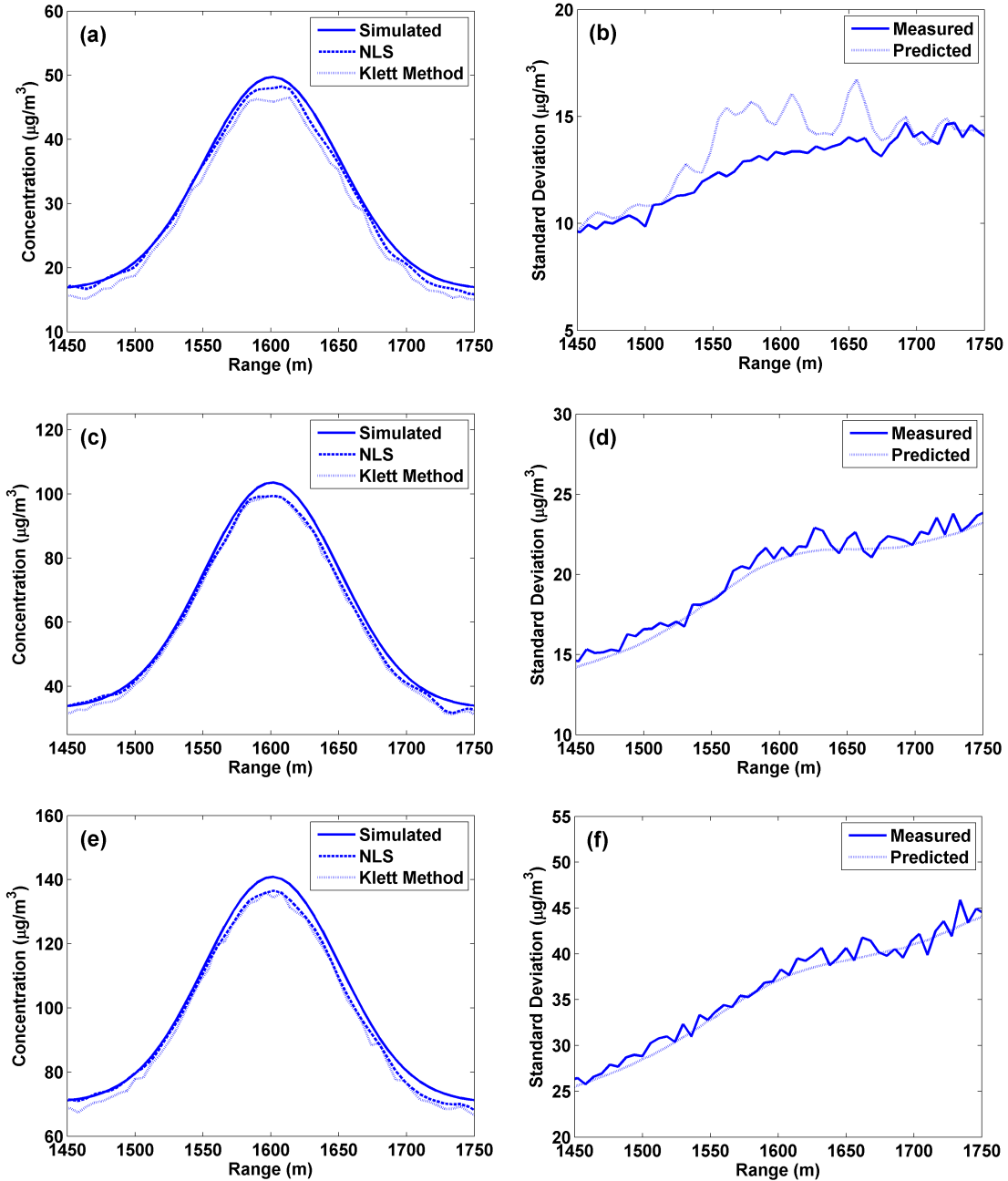


Fig. 3.5: Estimated  $\text{PM}_{10}$  mean concentration and standard deviation compared to actual values for synthesized data representing (a,b) average continental, (c,d) polluted continental, (e,f) and urban type plumes.

Table 3.2: Average retrieval error comparison.

PM <sub>10</sub> ( $\mu\text{g}/\text{m}^3$ )		800 m	1600 m	800 m	1600 m
Background	Plume	Error	99% CI	Error	99% CI
Average	None	0.28	$\pm 0.23$	0.67	$\pm 0.92$
	Average	0.10	$\pm 0.27$	-0.61	$\pm 0.94$
	Polluted	0.02	$\pm 0.29$	-1.73	$\pm 0.88$
Polluted	None	0.27	$\pm 0.28$	0.39	$\pm 1.15$
	Polluted	-0.51	$\pm 0.36$	-2.01	$\pm 1.24$
	Urban	-0.14	$\pm 0.46$	-4.18	$\pm 1.41$
Urban	None	0.13	$\pm 0.47$	0.74	$\pm 2.21$
	Urban	-0.42	$\pm 0.62$	-4.31	$\pm 2.49$

are plotted in figs. 3.5(b,d,f). They are also compared with the standard deviation values as measured from the set of individual retrievals. The predicted standard deviation values compare very favorably with the measured standard deviation of the individual retrievals.

### 3.8 Experimental Data

This NLS method was also performed on experimental data from the Aglite lidar instrument. The data were gathered at a hog farm located near Ames, Iowa, at 3:00 pm on September 5<sup>th</sup> 2005. The lidar was placed about 600 m east of the facility and the measurement was made with the lidar beam staring directly west at an elevation angle of 0 degrees elevation, parallel to the ground. The peak of the emission plume signal occurs at about 650 m, at which range the GFF is approximately 80% of its far-field value. The lidar was set up near the edge of the property line and we did not have permission to place the lidar on the neighboring property, thus preventing us from taking measurements from a greater range. The lidar integration time was set to 1 second and a range resolution of 4.8 meters was used. The measurement was taken for 400 seconds.

Two MetOne OPCs were deployed at the facility; one was mounted on an instrumentation trailer directly north of the facility, downwind of the emission plume, while another OPC was placed in the field on the east side of the facility where it was not expected to be impacted

by the emission plume of the facility. In addition, a Davis weather station was set up which measured temperature, pressure, and humidity. Complete details on the experiment setup are given by Bingham et al. [21].

The OPC measures particle counts at 20 second intervals and sizes the particles in to one of seven size ranges, resulting in high time-resolution in-situ measurement of the PSD of the aerosol. This PSD is converted into extinction and backscatter using (3.6) and using the index of refraction values for water-soluble aerosols given by the Air Force Handbook of Geophysics and the Space Environment [17]. The mass fraction concentrations for PM<sub>2.5</sub> and PM<sub>10</sub> are also calculated using the PSD, assuming the aerosol particle density equals one and the aerosol aerodynamic diameter equals the aerosol optical diameter.

It was assumed that the OPC in the field was unaffected by the facility and measured only the regional background atmosphere. The backscatter, extinction, and mass fraction concentration measurements of that OPC were averaged over the duration of the lidar measurement to calculate the optical and mass fraction coefficient vectors of the background aerosol. The temperature, pressure, and humidity parameters measured by the weather station were used to calculate the Rayleigh scattering contributions to backscatter and extinction. These were added to the coefficient vectors of the background aerosol to get the backscatter, extinction, and mass fraction vectors of the baseline component. It was assumed furthermore that the trailer-mounted OPC downwind of the facility measured the regional background aerosol plus the emission plume. This OPC was used to calculate the backscatter, extinction, and mass fraction vectors of the varying aerosol component. This was done by averaging the coefficients of the trailer-mounted OPC over the duration of the experiment and subtracting the baseline coefficients from the field OPC.

The reference point was selected to be at 900 meters. Although the background OPC was not mounted along the line-of-sight of the lidar, it was assumed that the backscatter at the reference point was equal to the background baseline backscatter values. The retrieval was performed on the average of 400 individual 1-second measurements.

The retrieval was performed both using only a single varying component,  $S = 1$ , and

using two varying components,  $S = 2$ . In both cases, the baseline component was the same and was defined using the backscatter, extinction, and mass fraction vectors from the field OPC. For the single-varying-component case, the component was described by the emission plume aerosol, whereas for the two-varying-component case, the first component was described by the emission plume aerosol and the second component was described using the same backscatter, extinction, and mass fraction vectors as the baseline aerosol. The backscatter vectors of the emission plume and regional background aerosols are linearly independent, meaning they form a basis and are acceptable selections for the retrieval. As indicated by (3.4), the PSD of the retrieved solution must be a linear combination of the regional background and emission plume PSDs. This is a good choice of components as it is reasonable to expect the PSD of the emission aerosol to be a combination the PSDs previously measured by the two OPCs.

As in the case of the synthetic data retrieval, a convolution matrix was used to compensate for both the GFF and the lidar pulse shape, and the same low-pass filter used to remove high-frequency noise in the solution.

The results of the one-component and two-component retrievals on the individual measurements are shown in fig. 3.6. Inspection of figs. 3.6(c,d) shows that the one-component solution is smoother than the two-component solution. This is explained by the fact that the solution is less constrained for the two-component case and is able to fit itself to more of the noise than in the one-component case. This is also illustrated in figs. 3.6(a,b) by the fact that the two-component solution provides a tighter fit to the observed data than the one-component solution. If multiple components are necessary to get a good fit with the measured aerosol, care must be taken in choosing them appropriately. The different components should have orthogonal backscatter vectors and the shapes of their PSD functions should be similar to the PSD of the target aerosol. Different choices of components may allow for solutions which fit the data equally well but may give significantly different aerosol concentration values.

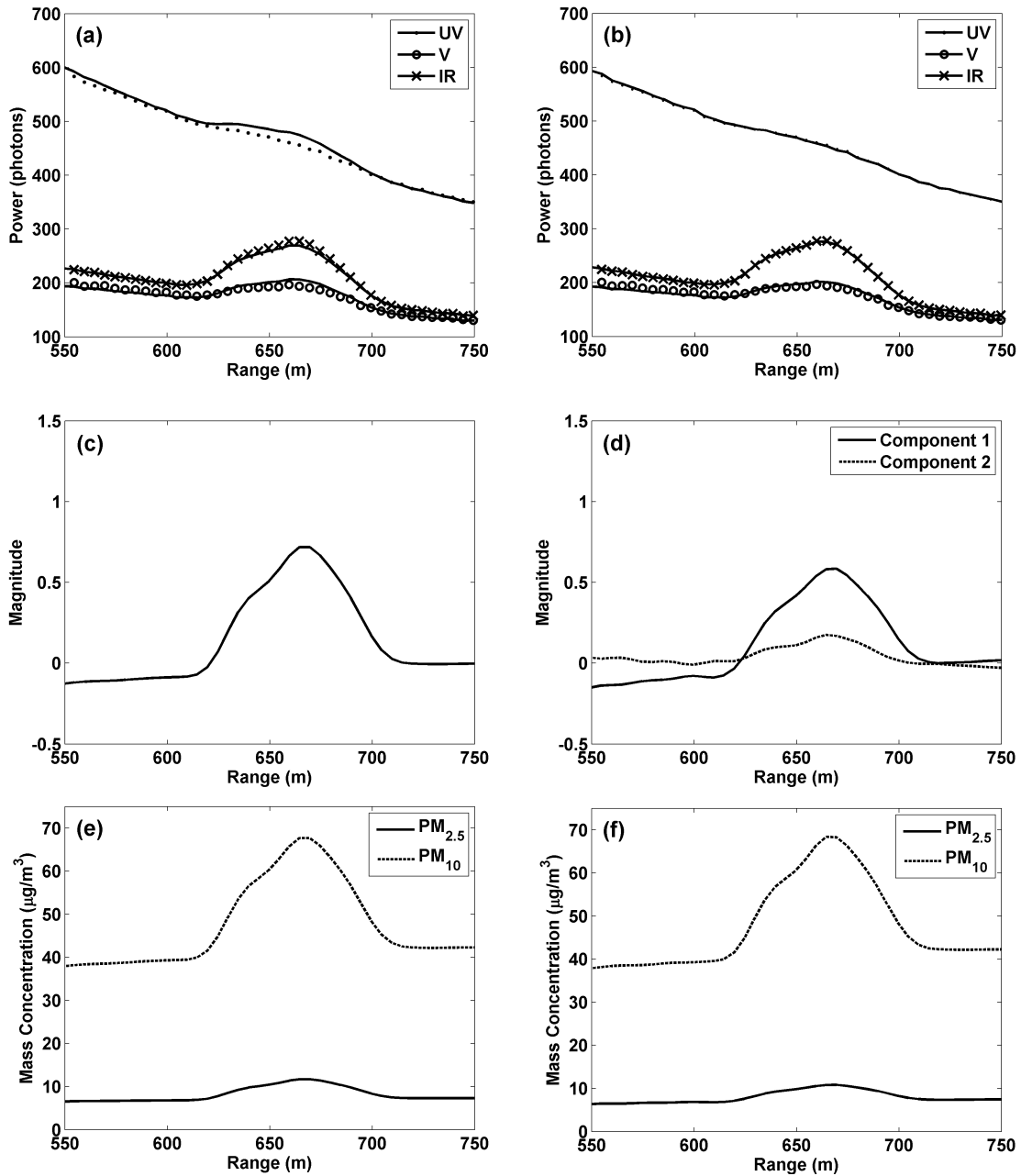


Fig. 3.6: Estimated values for (a,b) returned power, (c,d) emission component amplitude, and (e,f) PM concentration from swine facility measurement, assuming one component aerosol (left column) and two component aerosols (right column).

The NLS method demonstrates good stability when used on experimental data. Comparisons of this method with Klett's method for two-scatterers for experimental data at ranges further than the boundary point are shown in figs. 3.7(a,b). The feature at 650 m is the emission from the swine facility, also illustrated in fig. 3.6, and the feature at 1600 m corresponds to an unpaved road running perpendicular to the lidar beam direction. Figure 3.7(a) shows the results of applying both the NLS method and Klett's method to the experimental data previously illustrated in fig. 3.6. For fig. 3.7(a), both methods are applied under two sets of conditions: first, the boundary point backscatter values are equal to the baseline backscatter values, and second, the boundary point backscatter values are equal to 1.25 times the baseline backscatter values. In the first case, both methods give very similar results, and in the second case, both the NLS method and Klett's method give higher retrieved values for PM<sub>10</sub> over all ranges. However, whereas the solution from Klett's method becomes unstable very quickly at ranges past the reference point (located at 900 m), the solution generated by the NLS method remains stable at distant ranges. Figure 3.7(b) also illustrates the results of both methods under two sets of conditions: first, the baseline extinction coefficients are equal to the extinction values as calculated from the point-sensor instruments; and second the baseline extinction coefficients are equal to 1.50 times the point-sensor instrument values. In this figure it is also shown that under normal conditions both methods give similar results, however when the baseline extinction coefficients are overestimated, the solution generated by Klett's method becomes unstable. Under the same 50% error conditions, the NLS solution also increases somewhat at ranges beyond the boundary point, but to a much lower degree than the Klett solution.

### 3.9 Conclusion

This iterative least-squares lidar retrieval method has been shown to generate useful results from elastic lidar data. This method is capable of handling an arbitrary number of channels and generates stable solutions at ranges beyond the reference point and at low SNR values. When processing synthetic data, the algorithm gives solutions which are consistent with the original aerosol concentration values. When processing experimental data from

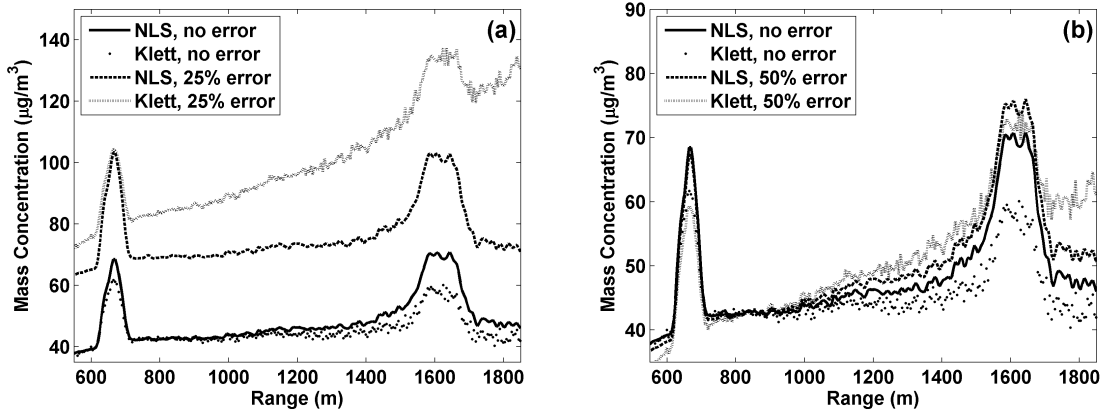


Fig. 3.7: Comparison of the stability of estimated PM<sub>10</sub> concentration from the NLS and Klett methods under the conditions of (a) 25% error in the boundary point backscatter coefficients, and (b) 50% error in the baseline extinction values.

the field, the algorithm gave solutions that were consistent with both the measured lidar returns and with the optical parameters calculated from point-sensor instruments. The method requires certain *a priori* constraints, including that the aerosol under investigation be modeled as an external mixture of component aerosols and that the terms in (3.7) be well described. Care must be taken to correctly choose these component aerosols, as different sets of components could potentially fit the data nearly equally well, while giving very different PSDs and mass fraction concentration results. Although this method can be used to probe the PSD of an aerosol, as described by (3.4), any PSD obtained using this method must necessarily be a linear combination of the PSDs of the selected component aerosols. For this reason, in order to encourage a physically realistic solution, components should be selected whose PSD shape is similar to the expected PSD shape of the target aerosol.

The ability of this method to account for noise, to use all channels in the retrieval simultaneously, and its stability at all ranges make this method especially useful for extracting maximal information in the far tail-end of a lidar signal, where the SNR is low. Nevertheless, it is possible for the estimator to give a solution that is physically unrealistic. A potential strategy to deal with this is to add constraints using Lagrange multipliers to the solution. Appropriate constraints can be selected depending on the expected characteristics of the aerosol under investigation. It is beyond the scope of this dissertation to investigate the

consequences of adding physical constraints to the solution; however this may be an effective way of improving the robustness of the algorithm.

## References

- [1] R. T. H. Collis, "Lidar: a new atmospheric probe," *Quarterly Journal of the Royal Meteorological Society*, vol. 92, pp. 220–230, 1966.
- [2] J. D. Klett, "Stable analytical inversion solution for processing lidar returns," *Applied Optics*, vol. 20, pp. 211–220, 1981.
- [3] J. D. Klett, "Extinction boundary value algorithms for lidar inversion," *Applied Optics Letters*, vol. 22, pp. 514–515, 1983.
- [4] F. G. Fernald, "Analysis of atmospheric lidar observations: some comments," *Applied Optics*, vol. 23, p. 652, 1984.
- [5] F. Rocadenbosch, C. Soriano, A. Comeron, and J. Baldasano, "Adaptive filter solution for processing lidar returns: optical parameter estimation," *Applied Optics*, vol. 37, pp. 7019–7034, 1998.
- [6] R. E. Warren, R. G. Vanderbeek, A. Ben-David, and J. L. Ahl, "Simultaneous estimation of aerosol cloud concentration and spectral backscatter from multiple-wavelength lidar data," *Applied Optics*, vol. 47, pp. 4309–4320, 2008.
- [7] J. M. B. Dias, J. M. N. Leitao, and E. S. R. Fonseca, "Reconstruction of backscatter and extinction coefficients in lidar: a stochastic filtering approach," *IEEE Transactions on Geoscience and Remote Sensing*, vol. 42, pp. 443–456, 2004.
- [8] D. Müller, U. Wandinger, D. Althausen, I. Mattis, and A. Ansmann, "Retrieval of physical particle properties from lidar observatison of extinction and backscatter at multiple wavelengths," *Applied Optics*, vol. 37, pp. 2260–2263, 1998.
- [9] I. Veselovskii, A. Kolgotin, V. Griaznov, D. Müller, U. Wandinger, and D. N. Whiteman, "Inversion with regularization for the retrieval of tropospheric aerosol parameters from multiwavelength lidar sounding," *Applied Optics*, vol. 41, pp. 3685–3699, 2002.
- [10] C. Böckmann, "Hybrid regularization method for the ill-posed inversion of multiwavelength lidar data in the retrieval of aerosol size distributions," *Applied Optics*, vol. 40, pp. 1329–1342, 2001.
- [11] M. Sicard, F. Molero, J. L. Guerrero-Rascado, R. Pedros, F. J. Exposito, C. Cordoba-Jabonero, J. M. Bolarin, A. Comeron, F. Rocadenbosch, M. Pujadas, L. Alados-Arboledas, J. A. Martinez-Lozano, J. P. Diaz, M. Gil, A. Requena, F. Navas-Guzman, and J. M. Moreno, "Aerosol lidar intercomparison in the framework of SPALINET - The Spanish lidar network: methodology and results," *IEEE Transactions on Geoscience and Remote Sensing*, vol. 47, pp. 3547–3559, 2009.

- [12] A. Comeron, F. Rocadenbosch, M. A. Lopez, A. Rodriguez, C. Munoz, D. Garcia-Vizcaino, and M. Sicard, “Effects of noise on lidar data inversion with the backward algorithm,” *Applied Optics*, vol. 43, pp. 2572–2577, 2004.
- [13] J. A. Reagan, X. Wang, and M. T. Osborn, “Spaceborne lidar calibration from cirrus and molecular backscatter returns,” *IEEE Transactions on Geoscience and Remote Sensing*, vol. 40, pp. 2285–2290, 2002.
- [14] C. C. Marchant, T. D. Wilkerson, G. E. Bingham, V. V. Zavyalov, J. M. Andersen, C. B. Wright, S. S. Cornelsen, R. S. Martin, P. J. Silva, and J. L. Hatfield, “Aglite lidar: a portable elastic lidar system for investigating aerosol and wind motions at or around agricultural production facilities,” *Journal of Applied Remote Sensing*, vol. 3, p. 033511, 2009.
- [15] R. M. Measures, *Laser Remote Sensing: Fundamentals and Applications*. New York: John Wiley, Inc., 1984.
- [16] T. K. Moon and W. C. Stirling, *Mathematical Methods and Algorithms for Signal Processing*. Upper Saddle River: Prentice Hall, 2000.
- [17] A. S. Jursa, *Handbook of Geophysics and the Space Environment*, Air Force Geophysics Laboratory, Hanscom Air Force Base, 1985.
- [18] C. F. Bohren and D. R. Huffman, *Absorption and Scattering of Light by Small Particles*. New York: Wiley, 1983.
- [19] J. G. Proakis and M. Salehi, *Digital Communications*. New York: McGraw-Hill, 2008.
- [20] S. W. Dho, Y. J. Park, and H. J. Kong, “Experimental determination of a geometrical form factor in a lidar equation for an inhomogeneous atmosphere,” *Applied Optics*, vol. 36, pp. 6009–6010, 1997.
- [21] G. E. Bingham, C. C. Marchant, V. V. Zavyalov, D. Ahlstrom, K. D. Moore, D. Jones, T. D. Wilkerson, L. Hipps, R. S. Martin, J. L. Hatfield, J. H. Prueger, and R. L. Pfeiffer, “Lidar based emissions measurement at the whole facility scale: method and error analysis,” *Journal of Applied Remote Sensing*, vol. 3, p. 033510, 2009.
- [22] M. Hess, P. Koepke, and I. Schult, “Optical properties of aerosols and clouds: The software package OPAC,” *Bulletin of the American Meteorological Society*, vol. 79, pp. 831–844, 1998.
- [23] C. C. Marchant, “Algorithm development of the Aglite-lidar instrument,” Master’s thesis, Utah State University, Logan, UT, 2008.

## Chapter 4

# Estimation of Aerosol Effective Radius by Multi-Wavelength Elastic Lidar

### 4.1 Background

A major subject of research using elastic-lidar is the investigation of atmospheric aerosols, including estimation of their concentration and PSD functions. These distributions can be very complex, with concentration, density, and index of refraction varying with particle size. In practical circumstances, when using a lidar with a limited number of channels, some sort of simplifying approximation of the aerosol PSD must be made. Simple aerosols are sometimes approximated using analytical functions such as the log-normal distribution, power-law distribution, or a modified gamma distribution, while more complex aerosols are often approximated as an “external mixture,” or in other words, a linear combination of simpler component aerosols [1].

Significant effort has been spent in developing methods for estimating the PSD of an aerosol using multi-wavelength lidar. Some of these methods assume that the aerosol fits a particular distribution type and operate by estimating the distribution’s parameters [2, 3], while other methods assume that the aerosol can be described as an external mixture and operate by estimating the amplitudes of the basis-aerosols [4–6].

Conventional algorithms have relied on a two-step process for estimating the PSD of an aerosol; first, estimating the scattering coefficients from the measured lidar signal, followed by estimating the PSD from the scattering coefficients. The first step is often performed using ratio-constraint techniques, such as the popular Klett method [7], and for the second step, several algorithms have been demonstrated that were developed from an optimization perspective [8, 9].

Several forms of the EKF have been demonstrated for estimating backscatter and extinction coefficients from lidar signals. By updating a state space vector with sequential observations, the EKF generates a weighted least-squares estimate of the state using *a priori* information from the previous measurements. Rocadenbosch's formulation of the EKF returns a state-vector containing backscatter and lidar ratio values as a function of range, at the expense of spatial resolution, for individual channels [10].

Alternatively, Warren's formulation of the EKF uses a two-step process, where a maximum-likelihood estimator first estimates the aerosol type, and then a Kalman filter is used to estimate aerosol concentration [11]. Warren's formulation linearizes the filter by assuming an optically thin aerosol and dropping the extinction expression, limiting the versatility of this formulation.

This chapter presents a solution to the lidar equation in the form of an adaptive extended Kalman filter [12]. In this formulation, the state vector is composed of the extinction coefficient of the current range and the optical thickness of the path up to and including the current range. The updated state equation is a function of the state at the previous range in the current measurement. This formulation offers the significant advantages of being both computationally efficient and giving stable performance under noisy conditions.

Nevertheless, it is reasonable to expect improved solution quality using an algorithm that estimates the aerosol PSD directly from measured lidar power, without any intermediate estimation steps. An NLS algorithm has been previously demonstrated that directly estimates basis-aerosol amplitudes from measured lidar power, using an iterative least-squares technique [13]. However, a novel form of the EKF, as applied to lidar, is presented here that also allows the direct estimation of basis-aerosol amplitudes from measured lidar power, with higher relative computational efficiency than the NLS technique.

## 4.2 EKF Formulation

### 4.2.1 Forward Model

A more in-depth description of the vector formulation of the lidar equation and its

application to the Aglite lidar instrument has been given previously [14], but is briefly outlined here for convenience. For an elastic lidar with  $c$  channels, the vector form of the lidar equation can be represented as (4.1).

$$\mathbf{p}(z) = \mathbf{k} \cdot \mathbf{g}(z) \cdot \frac{\boldsymbol{\beta}(z)}{z^2} \cdot \exp \left[ -2 \int_0^z \boldsymbol{\alpha}(z') dz' \right] + \boldsymbol{\nu}_z \quad (4.1)$$

This equation represents the measured power of the lidar signal plus noise, where  $p(z)$  has units of power [W], the variable  $z$  represents range [m], the function  $g(z)$  represents the attenuation (unitless) due to the GFF at range  $z$ , and the vectors  $\boldsymbol{\alpha}(z)$  [ $m^{-1}$ ] and  $\boldsymbol{\beta}(z)$  [ $m^{-1} \cdot sr^{-1}$ ] represent total backscatter and extinction coefficients as a function of range, respectively. The exponential expression represents attenuation due to extinction. The operator  $\cdot$  represents element-by-element multiplication, while the exponent function operates on an element-by-element basis. The vector  $k$  is composed of the calibration constants for each channel, and has units [ $W \cdot m^3 \cdot sr$ ]. The vector  $\boldsymbol{\nu}_z$  is a zero-mean random vector for range  $z$ , representing the observation noise in the signal. All of these vectors have  $c$  elements.

The geometric form factor can be removed from (4.1) in pre-processing if the form of  $g(z)$  is known, or if  $z$  is sufficiently large that  $g(z)$  can be approximated as unity. In this case, the relationship between  $k$  and the backscatter can be determined for some boundary point  $m$ .

$$\mathbf{k} = \frac{\mathbf{p}_m z_m^2}{\boldsymbol{\beta}_m \cdot \exp \left[ -2 \int_0^{z_m} \boldsymbol{\alpha}(z') dz' \right]} \quad (4.2)$$

If the value for  $\boldsymbol{\beta}_m$  is known, perhaps obtained from another source such as an in-situ instrument, it can be used to calculate  $\mathbf{k}$  [13].

The lidar equation can be rewritten in terms of  $\boldsymbol{\beta}_m$  by substituting (4.2) into (4.1).

$$\mathbf{p}(z) = \mathbf{p}_m \cdot \frac{\boldsymbol{\beta}(z) z_m^2}{\boldsymbol{\beta}_m z^2} \cdot \exp \left[ -2 \int_0^z \boldsymbol{\alpha}(z') dz' \right] + \boldsymbol{\nu}_z \quad (4.3)$$

Assuming that the atmosphere at any given range can be described as a homogeneous

baseline scattering component plus a linear combination of other spatially varying aerosol components, the total extinction and backscatter vectors can be written in matrix form.

$$\boldsymbol{\alpha}(z) = \boldsymbol{\alpha}_0 + A\mathbf{v}(z), \quad \boldsymbol{\beta}(z) = \boldsymbol{\beta}_0 + B\mathbf{v}(z) \quad (4.4)$$

The symbol  $\mathbf{v}$  is a vertical vector with  $s$  elements, where  $s$  is the number of basis aerosols needed to describe the spatially-varying part of the atmosphere. The vectors  $\boldsymbol{\alpha}_0$  and  $\boldsymbol{\beta}_0$  are  $s \times 1$ , and the matrices  $A$  and  $B$  are  $c \times s$ . The correct selection of  $\boldsymbol{\alpha}_0$ ,  $\boldsymbol{\beta}_0$ ,  $A$ , and  $B$  is essential for proper operation of the algorithm. In the case of the Aglite instrument, this is carried out using OPC point sensors and is described in a later section.

Substitution of (4.4) into (4.3) results in an equation representing the measured lidar power as a function of basis-aerosol amplitudes.

$$\mathbf{p}(z) = \mathbf{p}_m \cdot \frac{[\boldsymbol{\beta}_0 + B\mathbf{v}(z)] z_m^2}{\beta_m z^2} \cdot \exp \left[ -2 \int_0^z \boldsymbol{\alpha}_0 + A\mathbf{v}(z') dz' \right] + \boldsymbol{\nu}_z \quad (4.5)$$

#### 4.2.2 State-Space Signal Model

For a given range, the measured power can be represented as a function of the current basis-aerosol amplitudes and the summation of all previous basis-aerosol amplitudes. In order to form a system of equations that represent the lidar measurement process, the lidar equation needs to be represented in discrete form.

$$\mathbf{p}_i = \mathbf{p}_m \cdot \frac{[\boldsymbol{\beta}_0 + B\mathbf{v}(z)] z_m^2}{\beta_m z^2} \cdot \exp \left[ -2(z_i - z_m) \boldsymbol{\alpha}_0 - 2\Delta_z A \sum_m^i \mathbf{v}_j \right] + \boldsymbol{\nu}_z \quad (4.6)$$

The expression  $\Delta_z$  is the length of each range bin in meters. At first glance, the measured power appears not to be a Markov process, or in other words  $\mathbf{p}_i$  does not exclusively depend on  $\mathbf{v}_i$ , but also on all prior values of  $\mathbf{v}$ , due to the presence of the summation term in the exponent. Nevertheless, by making a substitution similar to the one by Dias et al. [12], the lidar equation can be expressed in Markov form.

$$\mathbf{p}_i = \mathbf{p}_m \cdot \frac{[\beta_0 + B\mathbf{v}(z)] z_m^2}{\beta_m z^2} \cdot \exp[-2(z_i - z_m)\alpha_0 - 2\Delta_z A(\mathbf{v}_i + \boldsymbol{\gamma}_i)] + \boldsymbol{\nu}_z \boldsymbol{\gamma}_i = \sum_m^{i-1} \mathbf{v}_j \quad (4.7)$$

With this formulation, it is clear that the current observation  $\mathbf{p}_i$  depends strictly on the current values of  $\mathbf{v}_i$  and  $\boldsymbol{\gamma}_i$  and an appropriate state vector, state update equation, and observation equation can be constructed.

$$\mathbf{x}_i = \begin{bmatrix} \mathbf{v}_i^T & \boldsymbol{\gamma}_i^T \end{bmatrix}^T, \quad \mathbf{x}_{i+1} = \begin{bmatrix} \theta I & 0 \\ I & I \end{bmatrix} \mathbf{x}_i + \mathbf{w}_i, \quad \mathbf{p}_i = f(\mathbf{x}_i) + \boldsymbol{\nu}_i \quad (4.8)$$

The expression  $I$  is an identity matrix,  $f()$  represents the lidar equation, and  $\theta$  is a gain coefficient, which can reasonably have any value between 0 and 1. Setting  $\theta = 0$  will encourage the estimator to choose values for  $\mathbf{v}_{i+1}$  that are close to zero, while setting  $\theta = 1$  will encourage the estimator to choose values for  $\mathbf{v}_{i+1}$  that are close to  $\mathbf{v}_i$ . The term  $\mathbf{w}_i$  is a zero-mean random vector that describes the change in the state vector and  $\boldsymbol{\nu}_i$  is the zero-mean random vector that describes the measurement noise at range  $z_i$ . For an atmosphere described using  $s$  number of basis aerosols, the state vector is a vertical vector with  $2s$  elements. By combining coefficients and making a change of variables, (4.7) can be represented in a simplified form.

$$\mathbf{p}_i = (\mathbf{b}_i + B'_i \mathbf{x}_i) \cdot \exp(\mathbf{a}_i + A'_i \mathbf{x}_i) + \boldsymbol{\nu}_z \quad (4.9)$$

A more general state-space formulation could also contain a zero-order term in the state-vector update equation shown in (4.8). However, it is normally not necessary because any *a priori* known baseline aerosol value can be incorporated into the  $\mathbf{b}_i$  term in (4.9). A linear approximation of the lidar equation can be made using a first-order Taylor series around the vector  $\mathbf{x}_0$ .

$$\begin{aligned}
p_i &\approx C_i \mathbf{x}_i + \mathbf{d}_i + \boldsymbol{\nu}_z \\
C &= \text{diag} [\exp (A' \mathbf{x}_0 + \mathbf{a})] [B' + \text{diag} (B' \mathbf{x}_0) A' + \text{diag} (\mathbf{b}) A'] \\
\mathbf{d} &= \text{diag} [\exp (A' \mathbf{x}_0 + \mathbf{a})] [\text{diag} (\mathbf{b}) (1 - A' \mathbf{x}_0) - \text{diag} (B' \mathbf{x}_0) A' \mathbf{x}_0]
\end{aligned} \tag{4.10}$$

Using the state-space signal model, it is straightforward to implement an EKF estimator. This requires knowledge of the covariance matrices of  $\boldsymbol{\nu}_i$  and  $\mathbf{w}_i$ .

$$\text{cov} (\mathbf{w}_i) = Q_i, \quad \text{cov} (\boldsymbol{\nu}_i) = R_i \tag{4.11}$$

The values of these covariances might be provided by in-situ instruments or by a computer model. It is assumed that these noise vectors are uncorrelated with respect to range. If the individual channels are uncorrelated with each other, then  $R_i$  is a diagonal  $c \times c$  matrix of the individual channel noise variances, whereas if the gain coefficient  $\theta$  equals zero,  $Q_i$  is a  $2s \times 2s$  matrix containing the covariance matrix of the basis-aerosols as a submatrix.

$$Q_i = \begin{bmatrix} \text{cov} (\mathbf{v}_i) & 0 \\ 0 & 0 \end{bmatrix}, \quad R_i = \begin{bmatrix} \nu_1 & & \\ & \nu_2 & \\ & & \ddots \end{bmatrix} \tag{4.12}$$

If  $\theta$  equals one,  $Q_i$  is composed of the covariance of the derivative of  $\mathbf{v}_i$ , and if  $\theta$  is some intermediate value,  $Q_i$  is composed proportionally of both the covariance of  $\mathbf{v}_i$  and the covariance of its derivative with respect to range.

At this point it is straight-forward to implement an EKF estimator [15]. The steps in this process are as follows:

1. Select state vector values at every range bin, around which the observation equation will be linearized;
2. Linearize the observation equation at every range bin;
3. Initialize the state vector and state covariance matrix, beginning at the reference range;

4. Run the Kalman filter forward with respect to range, beginning at the reference range and ending at the far range of the signal;
5. Initialize the state vector and state covariance matrix, beginning at the reference range;
6. Run the Kalman filter backward with respect to range, beginning at the reference range and ending at the near range of the signal;
7. Use the output of the filter, the estimated state vector values at each range, to linearize the observation equation at each range;
8. Repeat steps 3-7 until the output of the filter converges.

In this way, an estimate of the amplitudes of the basis-aerosols is obtained over the whole signal. It should be noted that it is convenient to choose a reference point where little variable aerosol is expected. This way, the state vector can reasonably be initialized as a zero vector.

#### 4.2.3 State-Vector Augmentation

The form of (4.1) assumes that the laser pulse shape of the instrument is a delta function. In some cases the laser pulse shape has significant temporal width and stretches over multiple measurement bins. An example of this is the Aglite lidar system [14]. As a result, the measured signal is a convolution of (4.1) with the lidar pulse shape. This can be corrected by augmenting the state vector to include basis-aerosol amplitudes over several bins.

If the laser pulse shape extends over  $f$  bins, the state vector can be expressed as an  $sfx1$  vector.

$$\mathbf{x}_i = \begin{bmatrix} \mathbf{v}_i^T & \mathbf{v}_{i-1}^T & \cdots & \mathbf{v}_{i-f+1}^T & \boldsymbol{\gamma}_{i-f}^T \end{bmatrix} \quad (4.13)$$

The influence of the laser pulse shape can be described by the matrix  $F$  with dimensions  $cxf$  appended to the observation equation.

$$\mathbf{p}_i = F \left[ (\mathbf{b}_i + B'_i \mathbf{x}_i) \cdot \exp(\mathbf{a}_i + A'_i \mathbf{x}_i) \right] + \boldsymbol{\nu}_z \quad (4.14)$$

The forms of vectors  $\mathbf{a}$ ,  $\mathbf{b}$ , and the matrices  $A'_i$ ,  $B'_i$ ,  $B''_i$ , and  $F$  are shown in (4.15).

$$\begin{aligned} \mathbf{a}_i &= -2 \begin{bmatrix} (z_i - z_m) \boldsymbol{\alpha}_0^T & (z_{i-1} - z_m) \boldsymbol{\alpha}_0^T & \dots \end{bmatrix}^T, \quad \mathbf{b}_i = z_m^2 \begin{bmatrix} \frac{\mathbf{p}_m^T \boldsymbol{\beta}_0^T}{z_i^2 \boldsymbol{\beta}_m^T} & \frac{\mathbf{p}_m^T \boldsymbol{\beta}_0^T}{z_{i-1}^2 \boldsymbol{\beta}_m^T} & \dots \end{bmatrix}^T, \\ A'_i &= -2\Delta_z \begin{bmatrix} A & A & \cdots & A & A \\ A & \cdots & A & A \\ \ddots & & \vdots & & \vdots \\ 0 & & & A & A \end{bmatrix}, \quad B'_i = \begin{bmatrix} B''/z_i^2 & & & 0 & 0 \\ & B''/z_{i-1}^2 & & & \ddots \\ & & 0 & & B''/z_{i-f+1}^2 \\ & & & & 0 \end{bmatrix} \\ F &= \begin{bmatrix} f_{1,1} & 0 & f_{2,1} & 0 & f_{f,1} & 0 \\ \ddots & & \dots & & \ddots & \\ 0 & f_{1,c} & 0 & f_{f-1,c} & 0 & f_{f,c} \end{bmatrix}, \quad B'' = \text{diag} \left( \frac{z_m^2 \mathbf{p}_m}{\boldsymbol{\beta}_m} \right) B \end{aligned} \quad (4.15)$$

The expression  $f_{i,j}$  is the relative magnitude of the laser pulse at the  $i$ th range bin and  $j$ th channel. Linearizing (4.14) using (4.10) yields an appropriate form for the observation equation of the EKF.

$$\mathbf{p}_i = F(C_i \mathbf{x}_i + \mathbf{d}_i) + \boldsymbol{\nu}_i \quad (4.16)$$

The state-update equation for this augmented-state vector and state-noise covariance matrix are described by (4.17).

$$\mathbf{x}_{i+1} = \begin{bmatrix} \theta & 0 \\ I & \ddots \\ 0 & I & I \end{bmatrix} \mathbf{x}_i + \mathbf{w}_i, \quad Q_i = \text{cov}(\mathbf{w}_i) = \begin{bmatrix} \text{cov}(\mathbf{v}_i) & & \\ & 0 & \\ & & 0 \end{bmatrix} \quad (4.17)$$

By constructing the EKF using the augmented-state vector together with (4.16) and (4.17), the estimator becomes an instance of a fixed-lag Kalman smoother [15].

Each update step of the EKF involves the computation of a number of matrix additions, multiplications, and a matrix inversion. The state vector is of length  $(f + 1)s$ , so the necessary matrix computations of each update step are of complexity order  $(f + 1)^3 s^3$ . Therefore, the computational complexity for an entire lidar measurement consisting of  $y$  range bins is  $(f + 1)^3 s^3 y$ , proportional to the number of bins in the measurement.

Some lidar retrieval algorithms use state vectors containing atmospheric values from all range values at the same time [8, 9]. These methods do not apply the Kalman filter over range, but over time, and in both cases the length of the state vector is proportional to  $y$ . The iterative least-squares algorithm previously described by Marchant et al. also uses a state vector proportional to  $y$  [13]. These types of algorithms require multiplying large matrices, and as a result, the order of the computational complexity for retrieving one single lidar pulse over all its range values is proportional to  $y^3$ . On the other hand, forms of the EKF that are applied over range, including the one described here, have computational complexity simply proportional to  $y$ . Given the fact that many lidars like Aglite have thousands of range bins per measurement, this can be a significant issue.

### 4.3 Simulation

The performance of the augmented-state EKF was demonstrated by applying it to a set of synthetic test data. This test data was generated so as to match the parameters of the Aglite instrument, a micro-pulse three-channel lidar with UV, V, and IR channels, at wavelengths of 355, 532, and 1064 nm and a total output power of 5 W [14].

The synthetic data was generating by assuming that the atmosphere consisted of a homogeneous baseline scattering component plus a variable aerosol component. The Rayleigh scattering portion of the baseline component was modeled assuming a temperature of 293 K (68 F), relative humidity of 50%, and atmospheric pressure of 101.325 kPa. The Mie scattering portion was modeled as a Continental Polluted type aerosol [1].

The variable scattering component was modeled as an aerosol with a log-normal

distribution, whose logarithmic standard deviation equals 2.24. The magnitude and mode-radius of the distribution varied as functions of range, described by Gaussian functions centered at 1000 m range with standard-deviations of 100 m.

The scattering coefficients of the atmosphere were modeled using Rayleigh theory and the lidar signal was modeled based on the physical parameters of Aglite. Lidar channel efficiency values of 5.8e-4, 3.0e-4, and 4.3e-5 were used for the UV, V, and IR channels, respectively. The attenuation effects caused by the geometric form factor were applied to the signal, as well as the convolution effects due to the laser pulse shape. The effects of solar background radiation were modeled by adding a baseline noise component of 100, 250, and 10 photons to the UV, V, and IR channels, respectively. Finally, in order to model the effects of photon counting noise, the signal was modeled as a Poisson distributed random vector. This was repeated to generate 1000 individual measurement signals for testing.

In order to perform the retrieval on the synthetic data, the spatially varying aerosol must be approximated as a linear combination of basis-aerosols in order to satisfy (4.4). For experimental data measurements, these basis-aerosols can be selected using point-sensor instrument measurements. However in the case of synthetically generated data, this basis was calculated from the solution itself. This may seem like a paradox, since the properties of the aerosol must be known before those same properties can be retrieved from the measurement data, but the use of point-sensor measurements can resolve this when processing real-world experimental data.

The appropriate basis aerosols for the retrieval were calculated from the same backscatter coefficient functions that were used to generate the synthetic data. Principal component analysis was used to decompose these backscatter functions, resulting in three orthonormal backscatter basis vectors with their corresponding amplitude functions [15]. The state-vector covariance was assumed to be stationary and was formed using (4.17). The backscatter coefficients as functions of range and the basis vectors of the two most significant components are illustrated in fig. 4.1(a,b).

The volume distribution of the varying aerosol was calculated as a function of range,

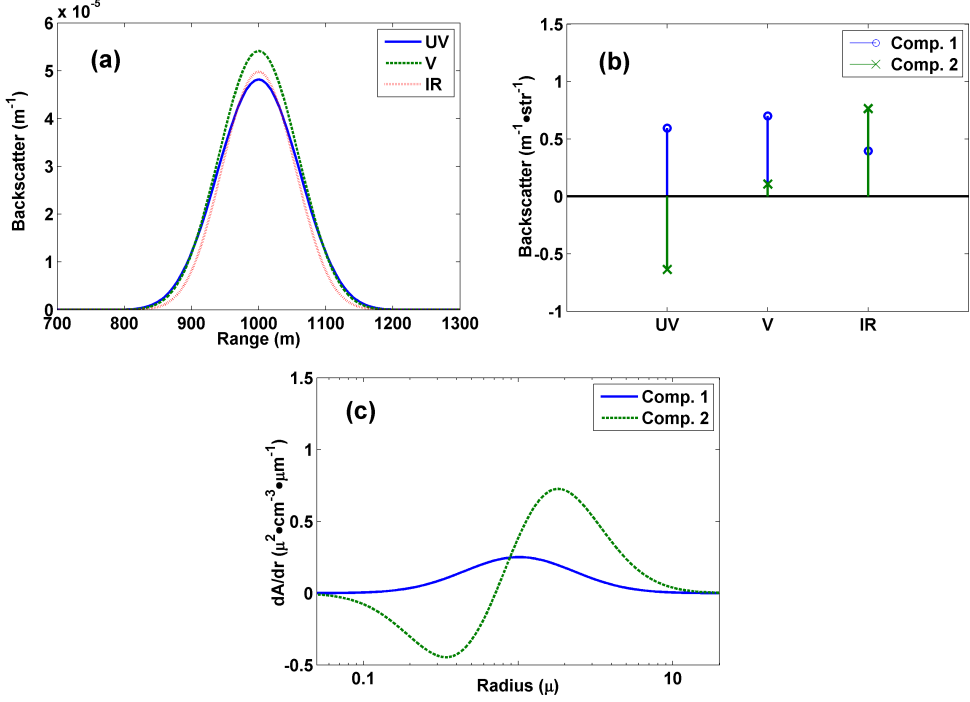


Fig. 4.1: Backscatter coefficients of a (a) single-component, and (b) two-component aerosol as a function of range. (c) The particle volume distributions of the two components.

and the PSD functions of the individual components were calculated so that their combined volume distribution matched the varying aerosol as closely as possible. The volume distribution is defined by (4.18), where  $r$  is the particle radius [ $\mu\text{m}$ ] and  $n(r)$  is the particle size distribution of the aerosol [ $\#\cdot\text{cm}^{-3} \cdot \mu\text{m}^{-1}$ ].

$$\frac{dV}{dr} = \frac{4}{3}\pi r^3 n(r) \quad (4.18)$$

The particle volume distributions for the two components are illustrated in fig. 4.1(c). Using the calculated PSD functions for the individual components, their extinction vectors were also calculated. In addition, the baseline scattering coefficient vectors were chosen so as to match those used to generate the synthetic data; the backscatter and extinction vectors of a Rayleigh component plus a Continental Polluted component. The reference point backscatter vector was chosen to be equal to the baseline backscatter vector.

The augmented-state EKF estimator was constructed following the steps outlined

previously and applied to the synthetic data. The gain coefficient  $\theta$  was set to 0.75 and a reference point range of 600 m was used. The estimator was applied to each of the individual return power measurements, resulting in values for the component amplitude functions and estimated returned power for each of the 1000 measurements. Using the estimated component amplitudes, the aerosol PSD was calculated for every range.

An example of both the measured and estimated returned power for a single measurement is shown in fig. 4.2(a). Even with the relatively low SNR of an individual measurement (fig. 4.2(b)), the retrieved power estimate is stable and closely matches the measured power. The SNR of the measured signal, expressed in power decibels, is also shown in the figure. The SNR describes the portion of the returned power signal that is attributable to the varying aerosol component, divided by the standard-deviation of the entire returned power signal.

Additionally, fig. 4.2(c) is a plot showing the average of all 1000 estimates of the component amplitudes, together with their standard deviation. Figure 4.2(d) shows the average error between the estimated component amplitude values and the “true values” used to generate the data, fig. 4.2(e) is a plot of the average aerosol volume-fraction concentration, and fig. 4.2(f) is a plot of the average aerosol effective radius, as calculated from the aerosol PSD as retrieved by the estimator.

A common measure of aerosol concentration is the PM<sub>10</sub> mass-fraction concentration, which is defined as the total mass in a volume of air of all the particles whose aerodynamic diameter is less than some diameter  $D$ .

$$PM_D = \rho \frac{4\pi}{3} \int_0^{D/2} r^3 n(r) dr \quad (4.19)$$

For this analysis, the simulant density  $\rho$  was unknown, so it was always assumed to equal unity. As a result, instead of mass-fraction concentration, the parameter of interest was volume-fraction concentration. Additionally, since both OPC and lidar instruments detect aerosol particles optically, it was necessary to assume that the optical and aerodynamic diameters were the same, even though they might not be in a real-world scenario.

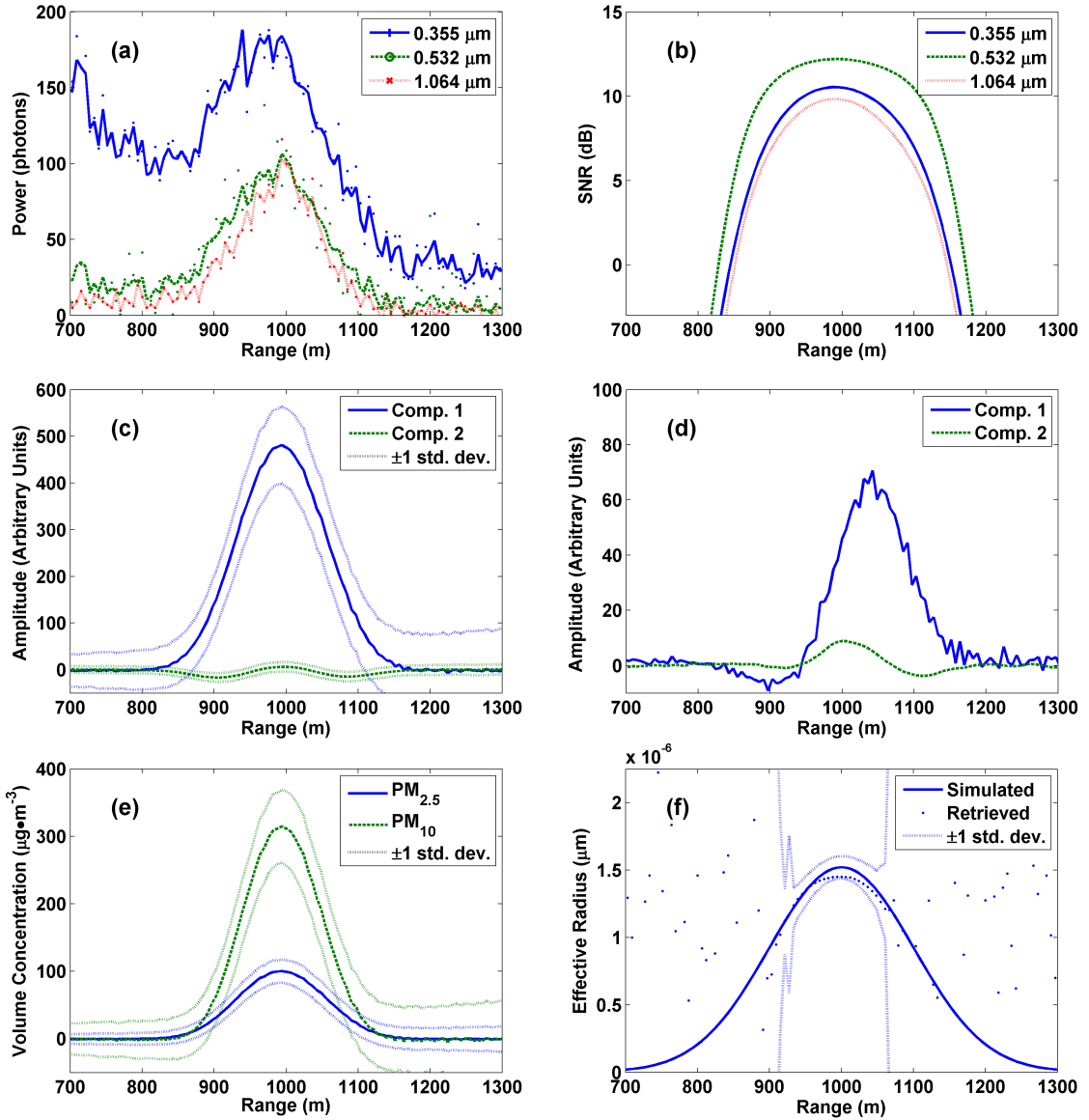


Fig. 4.2: Illustration of the performance of an EKF filter on a synthetic data set, including (a) the estimated returned power, (b) SNR, (c) component amplitude, (d) retrieved component bias, (e) volume concentration, and (f) effective radius.

The effective radius of an aerosol is defined as ratio of the third moment to the second moment of the aerosol's PSD.

$$r_{eff} = \int_0^{\infty} r^3 n(r) dr / \int_0^{\infty} r^2 n(r) dr \quad (4.20)$$

Since the particle size distributions of the two components are known *a priori*, it is straightforward to calculate the volume-fraction concentration and effective radius at every range once the component amplitudes have been estimated.

Inspection of fig. 4.2(f) shows that, although the simulated values for the effective radius do not exactly match the estimated values, their average values fall within at least one standard deviation. Furthermore, it is clear that while the estimated effective radius values are stable between approximately 920 and 1060 meters, outside of this range the values of the estimated effective radius become extremely unstable.

The volume-fraction concentration is a linear combination of the two components. This means that it is related to the sum of the components, and as their magnitude approach zero it remains stable. On the other hand, the effective radius is somewhat related to the ratio of the components, meaning that as the component amplitudes approach zero, the estimated value becomes unstable. This implies that reliable estimation of effective radius requires higher SNR values than reliable retrieval of volume-fraction concentration.

#### 4.4 Experimental Measurements

A set of experiments were conducted at Dugway Proving Grounds (DPG) involving biological aerosol simulants from May 31 through June 18, 2009. The test facility was the Joint Ambient Breeze Tunnel, an open-ended rectangular tunnel, 162 m long, 18 m high, and 13 m wide. The Aglite lidar instrument was positioned 1220 m west of the structure and aimed so that the transmitted beam travels along the long axis through the center of the structure.

A system of sprayer equipment was mounted to the walls of the structure, which was used to disperse various wet aerosols into the atmosphere contained within the structure.

The ends of the structure were open, allowing the free flow of air through it. A suite of point-sensor instruments were placed on tables within the structure, including three MetOne OPCs. The OPC measures particle counts in the ambient air at 2 s intervals and sizes the particles into one of seven size ranges, resulting in high time-resolution *in situ* measurement of the particle-size distribution of the aerosol.

For these experiments, the particle-size distribution was converted into extinction and backscatter using Mie theory and the index of refraction values given by the Air Force Handbook of Geophysics and the Space Environment [16, 17]. The volume-fraction concentrations for PM<sub>2.5</sub> and PM<sub>10</sub> were also calculated using the PSD, assuming that the aerosol particle density was equal to one, and the aerosol aerodynamic diameter was equal to the aerosol optical diameter.

During the course of a night, several sets of biological aerosol simulants were released into the tunnel. Each set consisted of three simulants. Each of these was continuously released over a period of 3 minutes, with a 3 minute period in between releases. Each simulant was released near the east opening and was wafted by the wind through the tunnel and out the west opening. A rest period of 15 minutes followed the end of each third release before the beginning of the next set of simulant releases.

A specific set of simulant releases is described here that was released in the very early morning of June 1. The first simulant was a bacterial insecticide *Bacillus thuringiensis* subspecies kurstaki (Btk), which was released from 12:32 am until 12:35 am using a Micronair disperser. This was followed by a release of Arizona Road Dust (ARD) from 12:38 am to 12:41 am using a Skil-Blower disperser. Finally, the simulant Male-specific bacteriophage (MS2) was released from 12:43 am to 12:46 am. The effective radius and assumed aerosol type for each simulant are shown in Table 4.1. The average temperature, pressure, relative humidity, wind speed, and direction are also shown in Table 4.1.

The Aglite instrument was operated from 12:29 am until 12:48 am, with 0.5 s temporal resolution and measured the releases of these simulants. A reference range of 1150 m was selected, and the gain coefficient  $\theta$  was set to 0.75. The augmented-state EKF was applied to

Table 4.1: Simulant properties and conditions.

Simulant	Type	Eff. Radius ( $\mu\text{m}$ )	Temp. ( $^{\circ}\text{C}$ )	Press. (kPas)	Rel. Hum. (%)	Wind Speed (m/s)	Wind Dir.
Btk	water soluble	2.1	17.0	86.4	62.0	2.0	SE
ARD	dust like	2.2	17.1	86.4	61.5	1.7	SE
MS2	water soluble	2.4	16.9	86.4	62.2	2.5	SSE

the measurements, resulting in estimates both for the returned power and for the amplitudes of the basis aerosols, which were converted into PSD as a function of range. In turn, the PSD functions used to calculate the  $PM_{10}$  volume-fraction concentration and the effective radius, which are plotted as a function of time and range in fig. 4.3 for the MS2 simulant.

Baseline measurements of the atmosphere were conducted during the rest periods. The PSD measurements of the OPC were averaged over the duration of the rest period, and the baseline backscatter and extinction coefficient values attributable to aerosol were calculated using Mie theory, assuming that the baseline aerosol had index of refraction values of a water-soluble type aerosol [17]. The portion of the baseline coefficients that were attributable to Rayleigh scattering was calculated using meteorological measurements of temperature, pressure, and humidity. The Mie and Rayleigh scattering coefficients were added together, resulting in the total baseline extinction and backscatter coefficients, as described by (4.4). The values of the baseline backscatter vector were also used for the reference point backscatter vector.

For the retrieval, each simulant was classified as being a water-soluble or dust-like aerosol for purposes of selecting appropriate index of refraction values. The basis aerosol components were calculated for each simulant using the OPC measurements taken during the actual time of release. First, the measurements of the three OPC instruments were concatenated together and converted into backscatter coefficients. Next, principle component

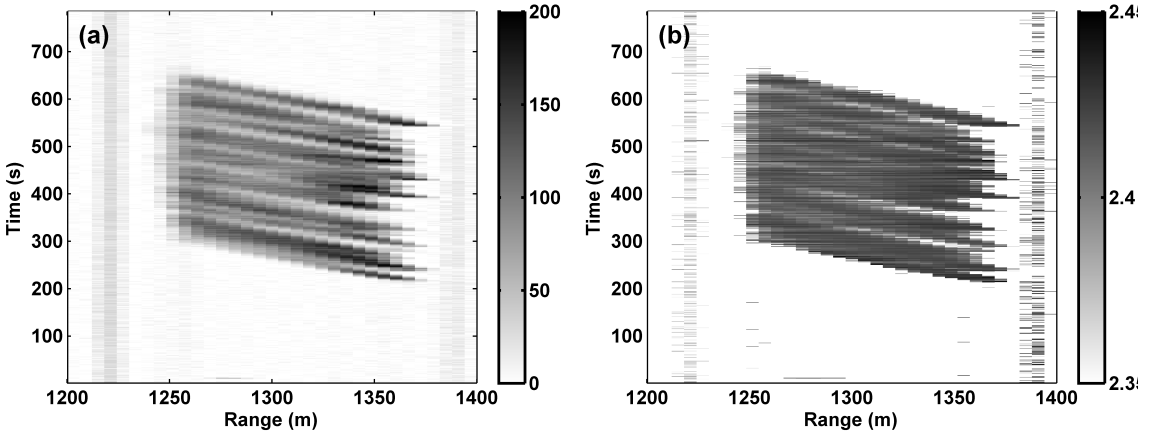


Fig. 4.3: Images of the estimated (a)  $\text{PM}_{10}$  volume-fraction concentration, and (b) effective radius for the MS2 simulant.

analysis was applied to these coefficients to identify the two main backscatter components of the aerosol. Lastly, the PSD functions of these components were identified and used to construct the matrices  $A$  and  $B$  in (4.4). In this way, the backscatter and extinction vectors of the basis-aerosols were identified.

The results given by the augmented-state EKF for each of the Btk, ARD, and MS2 type simulants are illustrated in fig. 4.4. Each measured return power signal was averaged over a 100 s interval during the peak release time for each simulant. The augmented-state EKF was applied to each of these measured power signals, and the effective radius was estimated as a function of range. Figure 4.4 shows comparisons of the average measured return power with the estimated return power given by the EKF, as well as the estimated effective radius as a function of range.

Inspection of the figure shows that the estimated return power matches the measured return power reasonably well for the Btk and ARD type simulants, however they match poorly for the MS2 type simulant. This may be due to incorrect assumed values for the indices of refraction of the simulant, or it may be due to poor measurement of the simulant particle size distribution by the OPC instruments.

Both the Btk and MS2 type simulants showed little variation in the estimated effective radius value, meaning that each simulant's backscatter values on the different channels

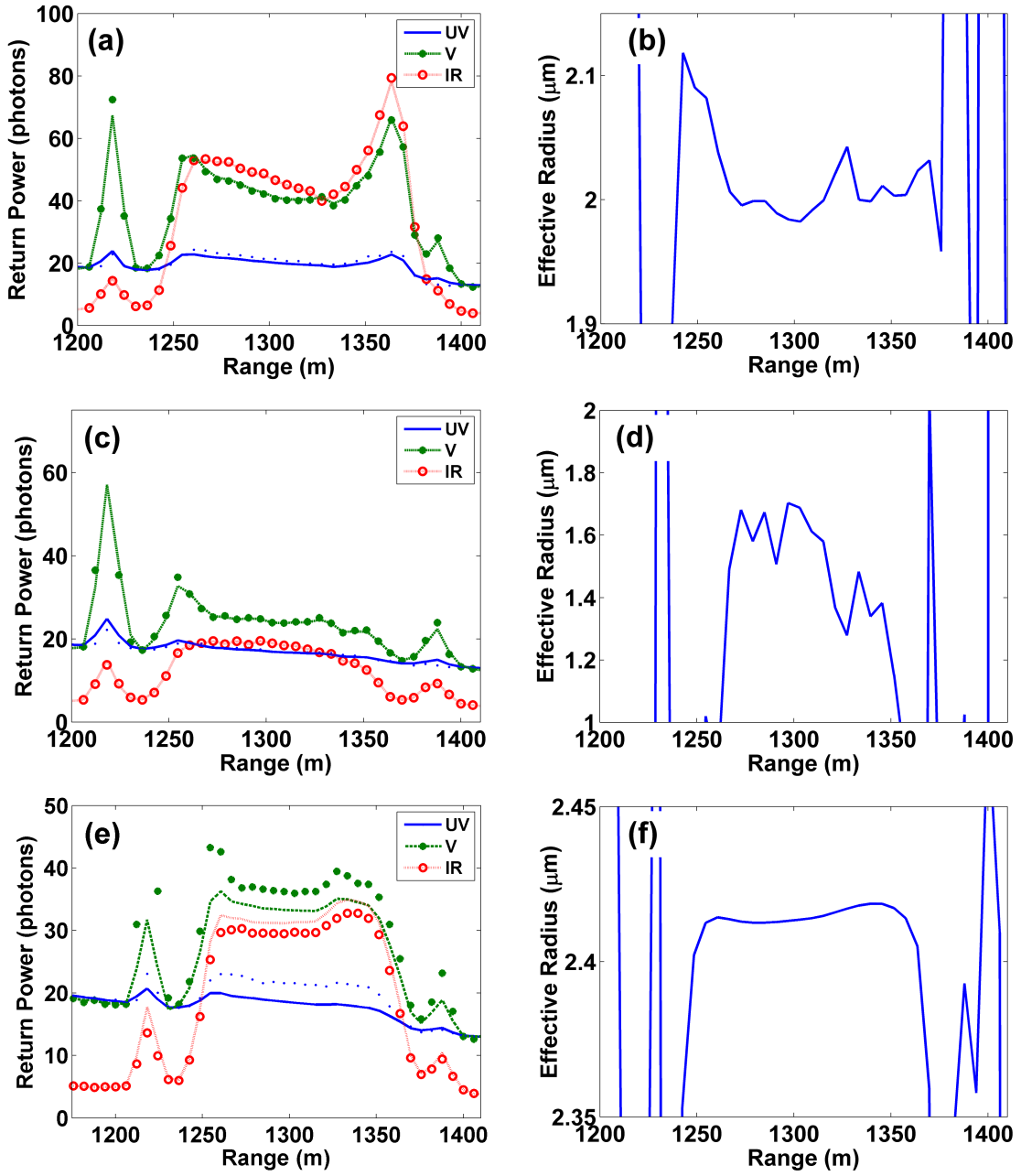


Fig. 4.4: Measured (symbols) and estimated (lines) average return power and estimated effective radius for (a,b) Btk, (c,d) ARD, and (e,f) MS2 type simulants.

changed little relative to one another with respect to range. Although some structure is visible in fig. 4.4, the simulant appears to be relatively homogeneous. The variation of the effective radius value of the ARD type simulant might be explained by its much lower signal magnitude.

## References

- [1] M. Hess, P. Koepke, and I. Schult, “Optical properties of aerosols and clouds: the software package OPAC,” *Bulletin of the American Meteorological Society*, vol. 79, pp. 831–844, 1998.
- [2] M. D. Guasta, M. Morandi, L. Stefanutti, B. Stein, and J. P. Wolf, “Derivation of Mount Pinatubo stratospheric aerosol mean size distribution by means of a multiwavelength lidar,” *Applied Optics*, vol. 33, pp. 5690–5697, 1994.
- [3] G. von Cossart, J. Fiedler, and U. von Zahn, “Size distributions of the NLC particles as determined from 3-color observations of NLC by ground-based lidar,” *Geophysical Research Letters*, vol. 33, pp. 5690–5697, 1994.
- [4] M. D. King, “Sensitivity of constrained linear inversions to the selection of the lagrange multiplier,” *Journal of Atmospheric Science*, vol. 39, pp. 1356–1369, 1982.
- [5] D. P. Donovan and A. I. Carswell, “Principal component analysis applied to multiwavelength lidar aerosol backscatter and extinction measurements,” *Applied Optics*, vol. 36, pp. 9406–9424, 1997.
- [6] D. Müller, U. Wandinger, and A. Ansmann, “Microphysical particle parameters from extinction and backscatter lidar data by inversion with regularization: theory,” *Applied Optics*, vol. 38, pp. 2346–2357, 1999.
- [7] J. D. Klett, “Lidar inversion with variable backscatter/extinction ratios,” *Applied Optics*, vol. 24, pp. 1638–1643, 1985.
- [8] C. Böckmann, “Hybrid regularization method for the ill-posed inversion of multiwavelength lidar data in the retrieval of aerosol size distributions,” *Applied Optics*, vol. 40, pp. 1329–1342, 2001.
- [9] I. Veselovskii, A. Kolgotin, V. Griaznov, D. Müller, U. Wandinger, and D. N. Whiteman, “Inversion with regularization for the retrieval of tropospheric aerosol parameters from multiwavelength lidar sounding,” *Applied Optics*, vol. 41, pp. 3685–3699, 2002.
- [10] F. Rocadenbosch, C. Soriano, A. Comeron, and J. Baldasano, “Adaptive filter solution for processing lidar returns: optical parameter estimation,” *Applied Optics*, vol. 37, pp. 7019–7034, 1998.

- [11] R. E. Warren, R. G. Vanderbeek, A. Ben-David, and J. L. Ahl, "Simultaneous estimation of aerosol cloud concentration and spectral backscatter from multiple-wavelength lidar data," *Applied Optics*, vol. 47, pp. 4309–4320, 2008.
- [12] J. M. B. Dias, J. M. N. Leitao, and E. S. R. Fonseca, "Reconstruction of backscatter and extinction coefficients in lidar: a stochastic filtering approach," *IEEE Transactions on Geoscience and Remote Sensing*, vol. 42, pp. 443–456, 2004.
- [13] C. C. Marchant, T. K. Moon, and J. H. Gunther, "An iterative least square approach to elastic-lidar retrievals for well-characterized aerosols," *IEEE Transactions on Geoscience and Remote Sensing*, vol. 48, pp. 2430–2444, 2010.
- [14] C. C. Marchant, T. D. Wilkerson, G. E. Bingham, V. V. Zavyalov, J. M. Andersen, C. B. Wright, S. S. Cornelsen, R. S. Martin, P. J. Silva, and J. L. Hatfield, "Aglite lidar: a portable elastic lidar system for investigating aerosol and wind motions at or around agricultural production facilities," *Journal of Applied Remote Sensing*, vol. 3, p. 033511, 2009.
- [15] T. K. Moon and W. C. Stirling, *Mathematical Methods and Algorithms for Signal Processing*. Upper Saddle River: Prentice Hall, 2000.
- [16] A. S. Jursa, *Handbook of Geophysics and the Space Environment*, Air Force Geophysics Laboratory, Hanscom Air Force Base, 1985.
- [17] C. F. Bohren and D. R. Huffman, *Absorption and Scattering of Light by Small Particles*. New York: Wiley, 1983.

## Chapter 5

### Estimation of Dairy PM Emission Rates by Lidar and Inverse Modeling

#### 5.1 Application

Agricultural production facilities are being increasingly investigated for emissions of pollutants into the atmosphere in order to understand their contributions to and effects on local and regional air quality. Under the Clean Air Act, the EPA has set threshold levels for widespread criteria pollutants considered harmful to public health and the environment, referred to as the National Ambient Air Quality Standards (NAAQS) [1]. The NAAQS include standards for aerosol as PM<sub>2.5</sub> and PM<sub>10</sub>, which are defined as the sum of particles with aerodynamic equivalent diameters  $\leq 2.5$  and  $\leq 10 \mu\text{m}$ , respectively. Furthermore, several state air quality regulatory agencies, such as the State of California Air Resources Board, have begun to require air pollution permits for agricultural operations that exceed certain sizes. The San Joaquin Valley Air Pollution Control District (SJVAPC) has required agricultural operations of nearly all sizes to select and implement approved Conservation Management Practices (CMP) since 2005 in order to meet PM<sub>10</sub> emissions reductions targeted under the EPA-accepted plan to bring the San Joaquin Valley airshed in California into compliance with ambient PM<sub>10</sub> levels. The EPA redesignated the airshed as being in compliance with ambient PM<sub>10</sub> levels in November 2008, but sources must continue to implement measures that helped meet PM<sub>10</sub> NAAQS, including CMPs, as part of their federally approved maintenance plan.

The accurate quantification of agricultural aerosol emission rates is an important part of the regulation process. To date, PM emission rate and emission factor values for dairies in the United States are scarce in published literature. Sources of particulate matter from dairies

include: animal activity, handling of feed and manure, combustion, vehicle activities on unpaved roads and areas, windblown soil, manure, and feed. It is expected that PM emission rates vary with multiple factors, including diet, bedding, type of pen or housing, feed storage and distribution practices, waste cleaning and storage practices, animal age, moisture level of soil or animal bedding, and meteorological conditions. A report by the US Department of Agriculture (USDA) estimated the PM<sub>10</sub> emission rate for a dairy to be 1.8 g/day/animal [2]. This was made by extrapolating the previously reported emission rate from a feedlot, and assuming that a dairy has 20% less emission. Schmidt et al. measured PM<sub>10</sub> concentrations in a naturally ventilated dairy barn during winter and summer, and calculated emission rates by coupling measured concentrations with ventilation rates estimated based on carbon dioxide exchange rates [3]. Winter average PM<sub>10</sub> emissions were 1.7 g/day/animal and summer average emissions were 0.3 g/day/animal. Goodrich et al. made measurements of TSP concentration using filter-based samplers at a free-stall and open lot dairy over two summers and then measured the PSD of the dust to determine the PM<sub>10</sub> fraction [4]. An inverse modeling technique was applied to the calculated PM<sub>10</sub> fractions to estimate PM<sub>10</sub> emission rates of 5.0 g/day/animal from the free-stall areas and 15.0 g/animal/day from the open lot areas. Using a similar approach, Martin et al. measured the dust concentration at a dairy during late fall using filter-based samplers and performed inverse modeling to estimate emission rates of 2.3 g/day/animal and 9.2 g/day/animal for PM<sub>2.5</sub> and PM<sub>10</sub>, respectively [5].

These previous estimates of PM emission rates relied on indirect methods, either extrapolating values from indirect measurements or by using computer modeling. Scanning aerosol lidar allows direct measurement of aerosol concentration, so the Aglite lidar was used to investigate particulate matter emissions from a free-stall and open-lot dairy in the San Joaquin Valley employing CMPs over an eight day period during June 2008.

## 5.2 Methodology

The PM emission rates from the selected dairy were estimated using two different techniques: a flux measurement technique using elastic lidar [6] and an inverse modeling

technique with the filter-based samples [7]. The PM emission rates were not estimated for the individual potential PM sources within the dairy, but rather an overall PM emission rate was estimated for the entire facility, normalized by the number of animal units in the facility.

### 5.2.1 Site Description

The dairy was located near Hanford, California and was surrounded by agricultural land, including two other dairies located approximately 500 m downwind. The dairy facility is roughly square shaped, covering 22.6 hectares, including all associated storage areas and access roads, which are mostly unpaved. It is bordered on its east side by a paved road and on the three other sides by cropland. The total number of animals on the dairy was 1,885, with: 950 milking cows, 100 dry milking cows, 30 bulls, 5 steers, and 800 heifers uniformly distributed between birth and two years old. One animal unit (AU) is defined herein as one heifer, steer, or bull cattle and 0.7 milking or dry cattle, according to the EPA definition [1], totaling 2,335 AU on the dairy. The youngest calves were housed in individual small pens, each with a shelter. Bulls, steers, dry cows, and heifers older than about four weeks old were housed in open lot pens, most of which were equipped with an open shelter. Milking cows were housed in a combination of open lot and covered free stall pens. Pens had a total area of 13.7 hectares, about 65% of the total dairy footprint. Feed lanes were concrete and sloped for drainage; all other surfaces were unpaved.

The CMP plan accepted by the San Joaquin Valley Air Pollution Control District for this dairy operation addressed the following: feed cultivation, harvest, and storage; unpaved roads and unpaved vehicle/equipment areas for crops; unpaved roads and unpaved vehicle/equipment areas for animal feeding operations; and dairy. For the feed cultivation, harvest, and storage categories, all implemented CMPs pertained solely to crop land and have no impact on PM emissions from the dairy area; this was also the case with the unpaved roads and unpaved vehicle/equipment areas for crops category. The unpaved roads and unpaved vehicle/equipment areas for animal feeding operations category listed the following CMPs: 1) water shall be applied to 1.4 km of private roads; 2) 0.2 km of private roads shall

be paved; 3) an 8 km per hour speed limit shall be placed on 1.4 km of private roads; 4) water shall be applied to 0.2 hectares of private vehicle/equipment traffic areas; and 5) an 8 km per hour speed limit shall be placed on 0.2 hectares of private vehicle/equipment traffic areas. The listed CMPs for the dairy category were the following, with the first three dealing with corral/manure handling and the last two dealing with overall management/feeding: 1) manure from open corrals shall be frequently scraped or removed; 2) pull-type manure harvesting equipment shall be used; 3) shaded areas shall be provided for cattle in open corrals; 4) wet material shall be placed in the feed wagon prior to mixing; and 5) feed shall be wetted during mixing. Each implemented CMP is targeted to reduce PM<sub>10</sub> emissions from the dairy.

The cows were milked twice a day, with a milking schedule from 8 am to 5 pm and from 8 pm to 5 am local time. A feed truck delivered feed to all pens from 5:30 am to 12 pm and from 3 pm to 5 pm local time. Milk cow lanes were flushed with water several times daily, while heifer, dry cow, bull and steer lanes were scraped approximately weekly. Corrals were scraped as needed, with gathered material stored as a mound in each pen for later removal. No corral scraping occurred during the measurement campaign, although a scraping was performed during equipment setup.

### **5.2.2 Setup**

Historical measurements of wind velocity for the previous three years were obtained from station #15 of the California Irrigation Management and Information System near Stratford, CA, 24 km southwest of Hanford. These records showed that wind conditions during the months of May and June were very consistent, with winds coming dominantly from the northwest. Based on these data, instruments were deployed so as to measure background concentrations northwest of the facility and to measure emission plumes south and southwest of the dairy. On-site measurements of the wind direction during the experiment confirmed the dominant direction to be from the northwest.

Two 15.3 m towers dedicated to holding meteorological instruments were erected at the site. One was located 400 m west of the dairy and the other was located just inside

the southern boundary of the dairy. Each tower was equipped with five cup anemometers mounted at heights of 2.5, 3.9, 6.2, 9.7, and 15.3 m. Five temperature and relative humidity sensors were also mounted at heights of 1.5, 2.5, 3.9, 6.2, and 9.7 m. Wind vanes were mounted on top of both towers at 15.3 m and a sonic anemometer was mounted on the tower inside the dairy boundary at 11.3 m. Campbell Scientific data-loggers were used to record and store the data from the towers and sonic anemometers.

Twenty four MiniVol PM filter-based samplers (Airmetrics) were deployed in groups of either two or three instruments at multiple locations around the dairy in order to allow characterization of the particle mass distributions ( $PM_{2.5}$ ,  $PM_{10}$ , and TSP) of both background and emitted aerosols. The MiniVol is a portable, programmable, filter-based sampler that yields mass concentration averaged over the sample time, with an impactor plate assembly employed for a single-sized particle fractionation. A pair of samplers consisted of one  $PM_{10}$  sampler and one  $PM_{2.5}$  sampler, whereas a group of three samplers consisted of one TSP sampler, one  $PM_{10}$  sampler, and one  $PM_{2.5}$  sampler. Nine Met One Instruments Aerosol Profilers, a type of OPC, were co-located with several of the sampler groups. The OPCs measured the optical particle size distribution with a period of 20 s using eight discrete size bins, counting the number of particles with diameters between two sequential cutoff values. The lower bin values were 0.3, 0.5, 0.6, 1.0, 2.0, 2.5, 5.0, and 10.0  $\mu\text{m}$ , with the eighth bin measuring all particles whose diameter was greater than 10  $\mu\text{m}$ . Flow calibration of the MiniVols was carried out just prior to the study; OPC flow measurements were conducted prior to and after the study, as well as counting calibrations/comparisons between all OPCs.

Upwind/background point sampler groups were located to the northwest (A) and north (B) of the dairy at 2 and 9 m elevations, respectively. Downwind measurements were made along the southern edge of the dairy at locations C (9 m), D (2 m), E (2 m), F (2 m), and AQ (2, 5, and 9 m), with sampler heights above ground level shown in parentheses. An air quality instrumentation trailer at location AQ was used for the following: sample preparation, collection, and storage; instrument handling, storage, and servicing; and data storage. The lidar instrument was housed within a trailer that was placed approximately

800 m west of the southwest corner of the dairy.

The PM sampling layout during the field campaign is shown in fig. 5.1. The locations of instrumentation towers are illustrated using solid black symbols, including the location of Aglite in the bottom-left corner of the figure. The dotted lines extending from Aglite represent the beam paths of the vertical profile scans. The dairy footprint is shown by a gray rectangle, and within it the pen, free-stall, and manure storage areas of the dairy are represented by white polygons. The expected dominant wind direction is shown by an arrow in the top-left corner.

Samples of the soil on unpaved roads and in dry-lot pens were collected on June 16 and analyzed for percent moisture level. The analysis showed that the average percent moisture  $\pm$  one standard deviation was  $0.56 \pm 0.50$  ( $n = 3$ ) and  $5.3 \pm 5.1$  ( $n = 7$ ) for the unpaved roads and pens, respectively.

### **5.2.3 Inverse Modeling**

Sources of PM at the dairy were modeled using the American Meteorological Society Regulatory Model (AERMOD) software. The interface used to run this model was the commercially available AERMOD View package by Lakes Environmental, Inc. The model assumes steady-state conditions, continuous emissions, and conservation of mass. It requires the source type, size, location, and emission rate be specified, as well as sampler/receptor locations. It also requires hourly averaged meteorological data including wind speed, wind direction, temperature, and cloud cover. Wind and temperature data were supplied by the meteorological towers and cloud cover was set to be zero for the entire period, as there were clear skies throughout the measurement campaign. The surrounding land was categorized as agricultural in the summer season for the purpose of estimating values for the Bowen Ratio, midday albedo, and surface roughness, which were 0.30, 0.14, and 0.03 m, respectively. Required upper air meteorological parameters were estimated by AERMET, the meteorological pre-processor for AERMOD, from the measured surface conditions. Based on these inputs, AERMOD calculated the period average concentrations at each sample location.

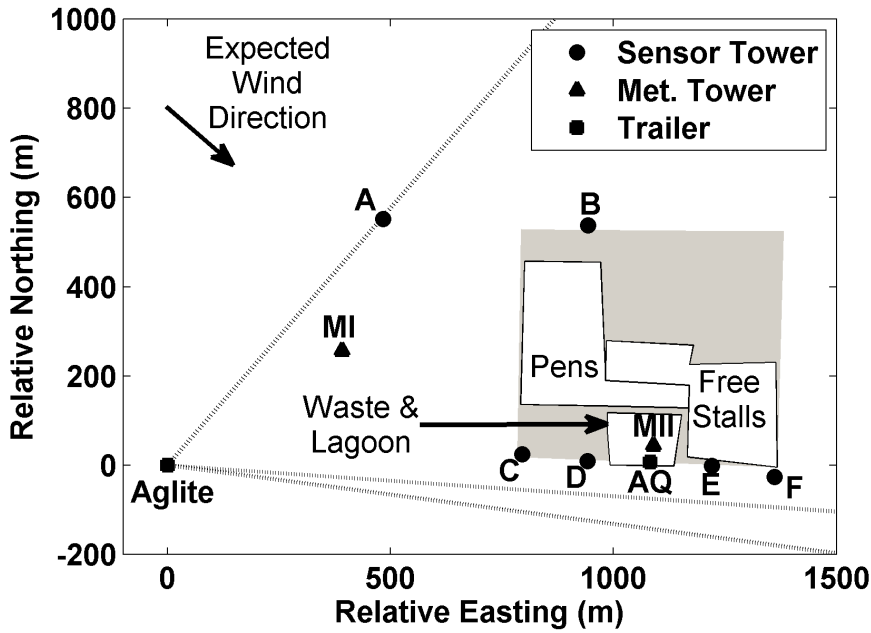


Fig. 5.1: Map of instrumentation locations.

The models require *a priori* values for the emission rate, which we seek to derive, in order to predict the sampler PM concentration values, which we have already measured. Inverse modeling is the process of adjusting the assumed emission rate to determine the actual emission rate by comparison of the already-measured concentration values to the model-predicted concentrations; it consists of determining that model-input emission rate that corresponds to the predicted concentration values that best fit measured values. AERMOD only predicts concentrations resulting from specified sources, in this case the dairy pens, so background/upwind PM levels must be subtracted from actual concentrations measured downwind of the dairy for comparison in inverse modeling. Facility-produced PM concentrations, or concentrations resulting from the dairy activities, were calculated on a location-by-location basis by subtracting the average upwind concentration from the measured downwind concentration. This difference was determined to be significant if greater than the 67% confidence interval about the upwind measurements, corresponding to one standard deviation. Only facility-produced concentrations deemed significant were used in inverse modeling.

Given a set of predicted PM concentration values, a cost metric is used to describe how well they match the measured values. In this case, the measured concentration values were assembled into a vector and the predicted concentration values were assembled into another vector, and the cost metric was chosen to be the sum of the squares of the difference. The optimal emission rate estimate was selected using a steepest descent algorithm; an initial or “seed” emission rate was chosen, the predicted concentration values were calculated, and the cost metric was calculated. The emission rate was then perturbed and a new cost metric value was calculated, thus allowing the computation of the gradient of the cost metric with respect to the emission rate. The emission rate was adjusted by a predetermined step size so as to lower the cost metric value and the procedure was repeated until the cost metric reached a minimum, at which point it was expected that the emission rate had converged to its optimal estimate.

Modeled sources of PM emission at the dairy included the pens of the heifers, dry and lactating cows, bulls and steers (13.3 hectares), as well as calf hutches (0.4 hectares). Fugitive dust emissions were seen during the campaign due to vehicle traffic on the unpaved service roads; however, these emissions were intermittent and not modeled, but were instead attributed to pen emissions as part of the operational activities of the dairy. Also, it was assumed that PM emissions from the wastewater lagoon and solids separator basin were negligible compared to other sources.

#### **5.2.4 Elastic Lidar**

Elastic lidar is a remote sensing technology with an application in imaging aerosols in the atmosphere [8]. Aglite is a lidar instrument that was used to map dust emissions at this dairy. Lidar (also known as laser-radar) functions by emitting a pulse of laser light and measuring the intensity and timing of the light as it is scattered by molecules and aerosols in the atmosphere. By recording the direction of the laser beam, the timing and intensity of the scattered light, it is possible to construct an image of the dust in the atmosphere.

Lidar technology can estimate the total PM emission rate from a source using a mass balancing technique. PM vertical concentration profiles are measured both upwind and

downwind of the emission source. The difference between the profiles is multiplied with a vertical wind velocity profile and the result is integrated over distance and height, resulting in the total aerosol emission flux passing through the profile area. In this way, the net emission rate of a facility can be directly observed with high temporal resolution and without requiring a mathematical model of the emission process [6]. In addition, elastic lidar enables measurement of dust concentration at thousands of points at relatively high temporal and spatial resolution, in contrast to a handful of filter samplers, which only measure dust concentration at a single point averaged over a time period typically measured in hours to days.

Elastic lidar allowed direct measurement of the dust emission rate of this dairy. Aglite is a three-wavelength micro-pulse scanning lidar, capable of imaging a 400 m high aerosol profile of the atmosphere in 25 seconds, with 8 m vertical resolution and 6 m horizontal resolution [9]. It requires data from both the OPCs and filter samplers for calibration and conversion of optical data into mass concentrations. Aglite was regularly calibrated throughout each day by co-locating its scanning beam next to a cluster of point sensors, which was mounted on a tower upwind of the dairy. The OPC in the cluster provided high temporal resolution measurements of dust concentration and the optical particle size distribution of the background atmosphere. Additionally, OPCs were located downwind of the dairy and measured the optical PSD of the impacted atmosphere. By taking the difference between upwind and downwind OPC data, the PSD of the emission plume was calculated. Using Mie scattering theory, the light-scattering properties of both the emission plume and the background aerosol were calculated. By aiming Aglite past the upwind OPC, calibration coefficients were calculated that established the relationship between the optical properties of the atmosphere and the photons detected by Aglite [9].

Aerosol volume concentration values are estimated from the return power measurements of Aglite using a form of the extended Kalman filter [10, 11]. The filter uses the optical properties of the emission aerosol and calibration coefficients of Aglite, as measured by the OPCs, to relate the measured return power to aerosol volume concentration.

Since both Aglite and the OPCs detect dust optically, they can only estimate the effective volume concentration of an aerosol by assuming detected particles are spherical and the same index of refraction as the calibration aerosol. This effective volume concentration is not necessarily equivalent to the true total volume of the aerosol particles, as the particles may be non-spherical and have a different index of refraction. Therefore, a conversion factor is required to convert the lidar aerosol volume measurement to units of mass; this is called the mass conversion factor (MCF) by the authors [12]. It is derived using co-located OPCs and MiniVol samplers. The OPC volume concentration, defined as the total volume of all particles in a given volume of air ( $V_{TSP}$ ) or the total volume of those particles whose optical diameter is less than or equal to either 2.5 ( $V_{2.5}$ ) or 10  $\mu\text{m}$  ( $V_{10}$ ), is averaged over the MiniVol sample time. The ratio of the MiniVol size fractionated concentration over the same size fraction of OPC volume concentration is the MCF. Because it measures the PSD, a single OPC can measure the separate effective volume concentrations corresponding to  $\text{PM}_{2.5}$ ,  $\text{PM}_{10}$ , and TSP. The MCF incorporates into a single coefficient the differences between mass measurement and optical measurement techniques as well as the effects of many aerosol characteristics that are otherwise difficult to accurately measure in ambient air (i.e. particle shape, index of refraction, porosity, and density).

The configuration of the lidar sampling is illustrated in fig. 5.1. It began with a continuous stare for calibration purposes at 0 degrees elevation and 41 degrees azimuth, clockwise from true north, lasting 40 seconds and pointing past the upwind sample location A. This was followed by two vertical scan pairs upwind of the facility, also at 41 degrees azimuth. The dashed line extending from the Aglite trailer to location A represents the direction of the upwind profile scan and calibration stare. The beam was then horizontally scanned about 10 m over the dairy from the upwind to downwind sampling locations, which was followed by five vertical downwind scan pairs. The vertical scan pairs consisted of one up scan and one down scan, where the beam began pointing parallel to the ground, was raised to 25 degrees elevation over 25 seconds, and then lowered back to ground level over 25 seconds. Three vertical scan pairs were made on the downwind border of the dairy, at

90 degrees azimuth, with two more at different distances downwind of the dairy, at 94 and 98 degrees azimuth. Unfortunately, due to a logistical error, the vertical scans made at 90 degrees azimuth, parallel to the downwind border of the dairy, were impaired by the backscatter of laser light off of the support guy-wires of a downwind instrument tower. For this reason, only vertical profiles taken at 94 and 98 degrees azimuth were used for estimating aerosol emissions. The two dashed lines extending from the Aglite trailer past the south of the dairy in fig. 5.1 represent these two scan angles for profile scans that did not suffer interference from sample towers. The use of the two separate downwind profile scans was motivated by an attempt to monitor changes in plume morphology at multiple ranges from the emission source, which is not discussed here.

### **5.3 Measurements**

The measurement campaign began at noon Pacific Standard Time (PST) on June 13th, 2008, and lasted through midnight on the 20th. All stated times are in PST. For logistical reasons, the OPC and MiniVol instruments were not available to make measurements on the afternoon of the 18<sup>th</sup> and the 19<sup>th</sup>. The lidar was operated continuously until it was stopped at 19:30 on the 19<sup>th</sup> due to a malfunction of its laser. One more period of measurements was conducted with the OPC and MiniVol instruments on the 20<sup>th</sup>. Meteorological conditions throughout the field study were hot and dry, with diurnally consistent winds. The mean temperature of the seven measurement periods at 10 m height was 28.8 degrees C; cloud cover was absent or extremely light and at high altitudes throughout with no recorded precipitation events. Calm or very low wind conditions existed each morning before sunrise with unstable direction. During daylight and through most of the night the average wind direction was from the northwest, with an average speed of 2.5 m/s at 10 m height.

#### **5.3.1 Point Samplers**

The filter samplers were run over seven separate periods from June 13 until June 20. On the 13<sup>th</sup> they ran from noon until 23:00 PST. On the 14<sup>th</sup>, 15<sup>th</sup>, 16<sup>th</sup>, and 17<sup>th</sup> they ran from 00:30 until 23:00. On the 18<sup>th</sup>, the filters ran from 00:30 until noon and on the 20th

the samplers ran from 11:00 until 23:00. There was a logistical break of one-and-a-half hours between sample periods to allow for instrument inspection, data recording, and placement of fresh filters in the MiniVol samplers.

Measured PM<sub>2.5</sub> concentrations downwind of the dairy ranged from 15.4  $\mu\text{g}/\text{m}^3$  to 56.0  $\mu\text{g}/\text{m}^3$ , with upwind levels ranging from 13.6  $\mu\text{g}/\text{m}^3$  to 31.4  $\mu\text{g}/\text{m}^3$ . Measured downwind PM<sub>10</sub> concentrations ranged from 59.2  $\mu\text{g}/\text{m}^3$  to 138.6  $\mu\text{g}/\text{m}^3$ , and upwind PM<sub>10</sub> levels ranged from 42.3  $\mu\text{g}/\text{m}^3$  to 104.5  $\mu\text{g}/\text{m}^3$ . Measured TSP concentrations downwind of the dairy ranged from 129.9  $\mu\text{g}/\text{m}^3$  to 246.4  $\mu\text{g}/\text{m}^3$ , with upwind levels ranging from 69.8  $\mu\text{g}/\text{m}^3$  to 188.4  $\mu\text{g}/\text{m}^3$ . In general, the highest downwind concentrations of all mass size fractions were measured at 2 m above ground level, with elevated measurements at 5 m and 9 m reporting slightly lower values. This same decreasing concentration with increasing measurement height trend was observed in OPC measurements. Filter samples with noted problems (dropped filter, sampler malfunction, insect on filter, etc.) were removed from further calculations.

MCF values were estimated for each of the MiniVol sample periods using data from sampler clusters that had both an OPC and MiniVols. Because the MCF can only be calculated during time periods when both the OPCs and MiniVols are operating, emission rates can only be determined from the lidar data during the filter sampler operational periods. An MCF for each sample period was calculated as the sum of the measured mass concentration values divided by the sum of the measured volume concentration values and is shown in Table 5.1, along with the average of all seven periods  $\pm 95\%$  confidence interval.

### 5.3.2 Aglite Measurements

The Aglite lidar was placed approximately 800 m due west of the southwest corner of the dairy. It was run continuously from noon on June 13<sup>th</sup> until 19:30 on June 19<sup>th</sup>, at which time the laser malfunctioned and prevented further measurements. The instrument ran in a continuous repeating scan pattern as described above. These measurements were converted to aerosol concentration profiles using an extended Kalman filter method [11] and the calculated MCFs for each period. As verification of the quality of the lidar data,

Table 5.1: Average calculated mass conversion factors ( $\pm 95\%$  CI) for each measurement period, June 2008.

MCF	13 <sup>th</sup>	14 <sup>th</sup>	15 <sup>th</sup>	16 <sup>th</sup>	17 <sup>th</sup>	18 <sup>th</sup>	20 <sup>th</sup>	Average
PM <sub>2.5</sub> /V <sub>2.5</sub>	5.56	2.71	2.67	2.03	1.89	1.96	4.83	3.09 $\pm$ 1.10
PM <sub>10</sub> /V <sub>10</sub>	1.43	1.28	1.27	1.24	1.13	1.17	1.58	1.30 $\pm$ 0.12
TSP/V <sub>TSP</sub>	0.90	0.90	0.94	0.85	0.87	0.89	1.29	0.95 $\pm$ 0.11

the PM concentrations measured by Aglite at 10 m above ground level were found to be consistent with those measured by point-sensor instruments during all measurement periods. Figure 5.2(a) is the average downwind vertical profile of the PM<sub>10</sub> concentration as measured by Aglite on the 13<sup>th</sup>, from 12:00 to 23:00. Figure 5.2(b) is the corresponding horizontal concentration map of period-average PM<sub>10</sub> concentrations as predicted using inverse modeling with AERMOD. The figure also shows the downwind profile lidar beam-paths used to construct fig. 5.2(a) and the footprint of the dairy. The dotted lines in fig. 5.2(b) show the position of downwind vertical lidar scans used to construct fig. 5.2(a). The range of maximum average concentration in fig. 5.2(a) matches somewhat with the location of maximum modeled aerosol concentration in fig. 5.2(b). Some of the discrepancy may be explained by the fact that during a portion of the measurement period the wind shifted to blowing due east, preventing the lidar from seeing the plume. Additionally, the lidar was unable to scan past a range of 1400 m due to obstruction by power lines.

### 5.3.3 Calculated Emission Rates

The size fractionated PM emission rates of the dairy were estimated for each measurement period using both inverse modeling coupled with the MiniVol sampler measurements and by application of a mass balance approach to the mass-calibrated lidar measurements. For inverse modeling, model predicted concentrations at each sample location were adjusted to best match measured facility-produced concentrations by minimizing the sum of the squares of the differences between the measured and modeled concentrations across all locations for each sample period as discussed previously. Facility-produced PM concentrations were calculated by taking the difference between each downwind sample and the average of

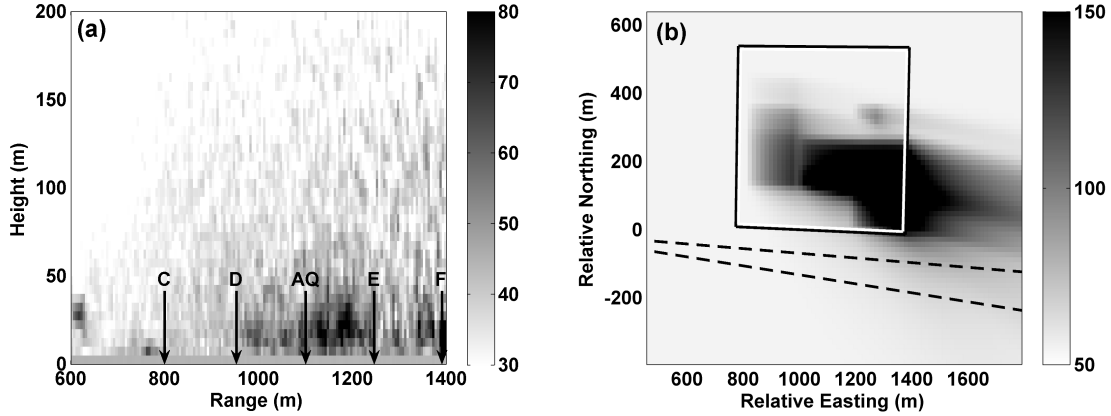


Fig. 5.2: Average PM<sub>10</sub> concentration ( $\mu\text{g}/\text{m}^3$ ) of (a) a vertical scan measured by lidar at 94 and 98 degrees azimuth, and (b) a horizontal map estimated by AERMOD, overlaid on the dairy footprint.

the upwind measurements. The emission rate input into the model that corresponded to the best fit between predicted and measured concentrations was the derived emission rate.

The net PM emissions of the dairy facility were also calculated from the mass-calibrated lidar data by taking the difference between downwind and upwind vertical scans. Using wind velocity measurements, these differences were then converted into individual measurements of the aerosol emission rate. Lidar scans were visually inspected for potential problems, such as aerosol-source activity in the upwind area or returns from solid objects; an observed example of a solid object returning the laser signal is a sampling tower or its guy wires. All scans with identified problems were removed from emission rate calculations, with impacted upwind scans also removing corresponding downwind scans.

The calculated emission values per sample period from inverse modeling and the average lidar measured emission rate  $\pm 95\%$  confidence interval are tabulated in Table 5.2. The overall averages, standard deviation, and 95% confidence intervals for each size fraction are shown at the bottom of the table. The determined emission rates from both techniques were of similar magnitude. There was significant variation in the estimated emission rates for the different measurement periods throughout the study.

While the overall mean values for each size fraction from the two emission rate calculation methods are very similar, day-to-day differences between the two were observed. These

Table 5.2: Average temperature, wind velocity, estimated emission rates, and  $\pm 95\%$  confidence interval (g/day/AU) for each period, estimated by inverse modeling and lidar.

Date (June 2008)		13 <sup>th</sup>	14 <sup>th</sup>	15 <sup>th</sup>	16 <sup>th</sup>	17 <sup>th</sup>	18 <sup>th</sup>	20 <sup>th</sup>
Temp. (°C)		33.0	27.2	27.1	26.7	25.4	21.9	34.8
Wind Speed @ 10 m (m/s)		2.9	2.4	2.3	2.6	3.1	2.1	1.4
Wind Dir. (degrees)		307	301	321	320	313	332	306
Sample period	Inverse model	Lidar	Inverse model	Lidar		Inverse model	Lidar	
June 13	9.3	$2.7 \pm 0.9$	25.5	$19.0 \pm 6.3$		47.7	$58.9 \pm 19.6$	
June 14	2.7	$1.6 \pm 0.5$	17.3	$19.0 \pm 5.4$		71.9	$54.1 \pm 15.4$	
June 15	1.3	$0.3 \pm 0.2$	9.8	$4.0 \pm 3.4$		42.1	$12.4 \pm 10.5$	
June 16	1.1	$0.8 \pm 0.5$	10.4	$14.9 \pm 8.7$		54.0	$45.0 \pm 26.3$	
June 17	0.7	$1.6 \pm 0.6$	8.7	$27.2 \pm 10.1$		32.6	$88.7 \pm 32.9$	
June 18	1.0	$0.6 \pm 0.3$	5.5	$6.3 \pm 3.7$		18.0	$19.1 \pm 11.1$	
June 20	3.5	-	44.6	-		110.0	-	
<b>Mean</b>	<b>2.8</b>	<b>1.3</b>	<b>17.4</b>	<b>15.1</b>		<b>53.8</b>	<b>46.4</b>	
<b>Std Dev</b>	<b>3.0</b>	<b>0.8</b>	<b>13.7</b>	<b>7.9</b>		<b>30.0</b>	<b>25.5</b>	
<b>95% CI</b>	<b>2.3</b>	<b>0.2</b>	<b>10.2</b>	<b>2.2</b>		<b>22.2</b>	<b>7.0</b>	

differences are likely due to different measurement and emission rate calculation techniques and their associated method uncertainties. This might also be attributed to variation in weather conditions or day-to-day variation in the facility operation. As previously stated, it is expected that the PM emission rate of a dairy may vary based on factors other than the number of animal units, such as soil type, management practices, and local climate. Furthermore, it is possible that there may be significant seasonal impacts that cause the emission rate of the facility to vary throughout the year.

#### 5.4 Conclusion

Particulate matter emissions from a free-stall and open lot dairy in the San Joaquin Valley of California were investigated over eight days in June 2008. The dairy milked 950 cows daily, with a total of 1885 animals in 13.7 hectares of pens. As a source of  $PM_{10}$  in the jurisdiction of the San Joaquin Valley Air Pollution Control District, the dairy was required to implement CMPs to reduce  $PM_{10}$  emissions and help the airshed reach attainment status. The selected CMPs were to reduce PM emissions from unpaved roads, unpaved storage areas,

manure handling, and feed mixing. Aerosol measurements were made using filter-based samplers, optical particle counters, and a scanning lidar system calibrated to provide mass concentration information. On-site meteorological measurements were combined with these PM measurements to calculate PM<sub>2.5</sub>, PM<sub>10</sub>, and TSP emission rates for the dairy using inverse modeling (with AERMOD) and a mass balance technique using lidar data.

The overall mean lidar- and inverse modeling-derived emission rates ± the 95% confidence intervals are shown in units of g/d/AU in Table 5.3, and are also shown in units of g/d/animal in Table 5.3. For comparison, also shown are the estimated emission values from previous studies [2–5].

Meteorology, soil type, soil moisture, housing type, bedding type, feed, manure handling and storage, associated vehicular traffic, and animal age and activity may all be significant factors affecting PM emissions from a dairy. Additionally, quantified PM emissions may vary depending on instrumentation and emission rate calculation techniques, as shown by the similar but not identical emission rates found by the two methods employed in this study. It is likely that the differences between all reported emission rates may be attributable to varying combinations of these factors. The study herein reported differs from Schmidt [3] and Martin [5] in climatic conditions or housing type. Goodrich reported similar emissions for open lot pens during the summer in the Texas panhandle, and lower values from free stall areas [3]. While Goodrich et al. also used an inverse modeling technique, the model employed was the Industrial Source Complex Short Term Model, Ver. 3 (ISCST3), whereas AERMOD was utilized in this study. Differences of maximum predicted concentrations from ISCST3 and AERMOD of up to a factor of two were reported by Faulkner et al. from a ground level area source with identical source, receptor, and meteorological inputs [13]. This difference would be carried into emission rate calculations. AERMOD replaced ISCST3 as the EPA recommended air dispersion model for regulatory purposes in December 2006. Based on the multiple potential factors affecting the quantification of emissions from dairies, the variation seen in the literature and herein reported are not unexpected.

It should be noted that emissions reported herein are not representative of the emissions

Table 5.3: Emission rates estimated by inverse modeling, lidar measurements, and previous studies.

Emission Rate (g/d/animal)	PM <sub>2.5</sub>	PM <sub>10</sub>	TSP
Inverse Modeling	3.5 ± 2.8	21.6 ± 12.6	66.6 ± 27.5
Lidar	1.6 ± 0.2	18.7 ± 2.7	57.5 ± 8.7
USDA [2]	-	1.8	-
Schmidt [3]	-	1.7 (winter) / 0.3 (summer)	-
Goodrich [4]	-	5 (free stall) / 15 (open lot)	-
Martin [5]	2.3	9.2	-

throughout the year, as measurements were taken under summer conditions (hot and dry) with relatively dry soil, and emissions during other seasons are expected to be lower due to emission suppression from precipitation events, among other factors. In order to determine suitable values for regulatory purposes, surveys of particulate emission rates should made at a variety of different dairies and pen types during different times of the year.

## References

- [1] EPA, “National pollutant discharge elimination system permit regulation and effluent limitation guidelines and standards for concentration animal feeding operations,” *Federal Register* 66(9), pp. 2960–3138, 2001.
- [2] USDA, “Quality research & technology transfer programs for concentrated animal feeding operations,” Washington, DC, 2001.
- [3] D. R. Schmidt, L. D. Jacobsen, and K. A. Janni, “Continuous monitoring of ammonia, hydrogen sulfide, and dust emissions from swine, dairy, and poultry barns,” in *ASAE Annual International Meeting / CIGR XVth World Congress*, p. 024060, 2002.
- [4] L. B. Goodrich, C. B. Parnell, S. Mukhtar, and S. C. Capereda, “A PM<sub>10</sub> emission factor for free stall dairies,” in *Proceedings of the Workshop on Agricultural Air Quality: State of the Science*, 2006.
- [5] R. S. Martin, K. D. Moore, and V. S. Doshi, Logan, UT, 2006, Unpublished data.
- [6] G. E. Bingham, C. C. Marchant, V. V. Zavyalov, D. Ahlstrom, K. D. Moore, D. Jones, T. D. Wilkerson, L. Hipps, R. S. Martin, J. L. Hatfield, J. H. Prueger, and R. L. Pfeiffer, “Lidar based emissions measurement at the whole facility scale: method and error analysis,” *Journal of Applied Remote Sensing*, vol. 3, p. 033510, 2009.

- [7] C. Cowherd, *Aerosol Measurement: Principles, Techniques and Applications, 2nd Edition*, ch. 28, pp. 845–858. Hoboken: John Wiley and Sons, 2005.
- [8] R. M. Measures, *Laser Remote Sensing: Fundamentals and Applications*. New York: John Wiley, Inc., 1984.
- [9] C. C. Marchant, T. D. Wilkerson, G. E. Bingham, V. V. Zavyalov, J. M. Andersen, C. B. Wright, S. S. Cornelsen, R. S. Martin, P. J. Silva, and J. L. Hatfield, “Aglite lidar: a portable elastic lidar system for investigating aerosol and wind motions at or around agricultural production facilities,” *Journal of Applied Remote Sensing*, vol. 3, p. 033511, 2009.
- [10] J. M. B. Dias, J. M. N. Leitao, and E. S. R. Fonseca, “Reconstruction of backscatter and extinction coefficients in lidar: a stochastic filtering approach,” *IEEE Transactions on Geoscience and Remote Sensing*, vol. 42, pp. 443–456, 2004.
- [11] C. C. Marchant, M. D. Wojcik, and W. J. Bradford, “Estimation of aerosol effective radius by multi-wavelength elastic lidar,” *IEEE Transactions on Geoscience and Remote Sensing*, p. submitted for publication, 2010.
- [12] V. V. Zavyalov, C. C. Marchant, G. E. Bingham, T. D. Wilkerson, J. L. Hatfield, R. S. Martin, P. J. Silva, K. D. Moore, J. Swasey, D. J. Ahlstrom, and T. L. Jones, “Aglite lidar: calibration and retrievals of well characterized aerosols from agricultural operations using a three-wavelength elastic lidar,” *Journal of Applied Remote Sensing*, vol. 3, p. 033522, 2009.
- [13] W. B. Faulkner, B. W. Shaw, and T. Grosch, “Sensitivity of two dispersion models (AERMOD and ISCST3) to input parameters for a rural ground-level area source,” *Journal of the Air & Waste Management Association*, vol. 58, pp. 1288–1296, 2008.

## Chapter 6

### Concluding Remarks

#### 6.1 Elastic Lidar Applications

Air quality issues have motivated the development of novel methods and technologies for investigating aerosols from agricultural and industrial sources. Elastic lidar is a technology that performs accurate measurement of aerosol concentration over large areas with high temporal and spatial resolution, enabling techniques for accurately characterizing and estimating aerosol emissions. Characterization of the properties, emission rates, and behavior of aerosols in the atmosphere are necessary for effective government regulation of air quality, determination of industrial and agricultural best practices, and homeland security issues.

Aglite's multiwavelength and scanning abilities have made it an appropriate platform for demonstrating lidar innovations in these types of applications. This dissertation has described the use of Aglite to image plume morphology, estimate wind speed, aerosol emission rate, mass concentration, and effective aerosol radius. Effective and practical algorithms have been described and demonstrated for estimating aerosol properties from lidar signals. The potential applications of a lidar instrument in conjunction with an effective algorithm are potentially innumerable.

Aglite's initial operation at a swine operation demonstrated the ability of elastic lidar to map aerosol concentration. By scanning the atmosphere around the facility, the lidar can image both emission plume from the facility and fugitive dust from bordering dirt roads and discriminate them by location. Additionally, Aglite proved the capability of a scanning multi-wavelength elastic lidar to estimate aerosol effective radius and also wind speed using characteristic plume morphology.

## 6.2 Lidar Design Tradeoffs

Lidar usefulness may be limited by hardware performance. In general, it is desirable for a lidar to have a high range resolution, many channels covering different wavelengths, polarization sensitivity, and have a high signal-to-noise ratio. It is also desirable for a lidar to be low-cost, durable, rugged, be eye-safe, have a fast scanning speed, and long range. Several of these characteristics are often at odds and good engineering practices require the selection of appropriate trade-offs between them.

There are certain design trade-offs that are particularly important in designing a lidar for aerosol detection. In particular, multiple channels with wavelengths well spaced in a range around the expected diameter of the target aerosol can enable estimation of particle effective radius or discrimination between aerosol types with different indices of refraction. Infrared wavelengths are often preferable to visible and ultra-violet wavelengths due to their insensitivity to Rayleigh scattering and the ability to select eye-safe channels. Outdoor use of lidar systems using typical power levels in the United States normally requires the obtainment of a special permit from the Federal Aviation Administration. The use of non-visible ( $>700$  nm) eye-safe channels (i.e. 1550 nm) can greatly ease the obtainment of such permits. The use of a linearly polarized transmitter, together with polarization sensitive channels, makes a lidar sensitive to aerosol asphericity. The addition of Raman scattering channels can improve the quality and stability of lidar aerosol estimates. However, Raman channels typically have significantly poorer SNR characteristics when compared to elastic channels and often can only be used during night operation. Differential absorption lidar systems are typically designed to detect gases, but are also sensitive to aerosols and such a lidar could potentially be used in conjunction with an elastic lidar system.

A high pulse-rate lidar can enable quick measurement of the atmosphere with high resolution, but have the disadvantage of increased solar background noise and having a shorter potential maximum range than a lower pulse-rate lidar. A high pulse-rate lidar can also allow the use of photon-counting detectors, which have lower dynamic range than current mode detectors, but have more convenient noise characteristics and are easier to

linearize. If the lidar scan speed is not significantly faster than the wind speed, this will induce morphological features in the lidar images. The use of a scanning mirror to steer the lidar beam may cause an azimuth dependency efficiency factor in the transmitter due to polarization effects. The receiver optics parameters determine the shape of the GFF. A narrow receiver field-of-view will reject solar background radiation, improving signal SNR, but will also increase near-range attenuation by the GFF. In practice, increased lidar complexity also leads to higher development and maintainance costs and decreased durability.

In general, lidar is effective at measuring aerosols' optical characteristics, however often it is the other characteristics that are of interest, such as mass concentration and chemical composition. It is a difficult problem to estimate these with lidar alone, however the usefulness of lidar can be greatly increased when used in conjunction with other significantly less-expensive instruments. For example, meteorological instruments could measure temperature, pressure, and humidity, to allow the estimation of Rayleigh scattering and its influence on the lidar signal, or aerosol point sensors could be used to measure aerosol chemical composition and particle size distribution, which can be used as constraints in the retrieval algorithm, improving its performance.

Often, absolute calibration of a lidar is a difficult task. It is desirable to make the lidar hardware isolated against vibration, temperature controlled, and to select robust hardware components, so that the lidar performance is stable over time. Additionally for field-use lidars, care should be taken to seal the instrument from intruding dust and insects. Even with careful hardware design, often the calibration coefficients of a lidar change over time. One strategy for compensating for this is to develop a calibration procedure that can be performed and repeated in the field. This may involve calibrating using a hard calibration target with known optical characteristics, calibrating using background atmospheric aerosols and aerosol point sensors, or calibrating using Rayleigh scattering from air molecules at high altitude.

### 6.3 Wavelength and Component Aerosol Selection

Much of the challenge in probing aerosols using lidar lies in the difficulty in tracking

spatial variability of aerosol properties. Two different lidar algorithms are described in this dissertation, both of which handle variation in aerosol characteristics by treating target aerosols as linear combinations of known basis aerosols. The choice of basis aerosols affects performance of a retrieval algorithm, so it is an important question how to appropriately select them. The backscatter vectors of the basis aerosols should be linearly independent. In addition, they should be selected so that the composite basis PSD functions accurately represent the true aerosol. Ultimately, whether a given basis is any good depends on whether using that basis results in good quality retrievals. There is a need for developing a method for correctly choosing a set of basis aerosols based on a lidar's wavelengths and the expected characteristics of the target aerosol.

On the flip-side of choosing basis aerosols, care should be taken when choosing lidar channel wavelengths. There can be significant engineering constraints on this choice, as affordable commodity lasers, detectors, and optical components are only available for certain wavelengths. The values in the backscatter vector of an aerosol depend on its PSD and index of refraction. If a lidar is purposed to measure variation in aerosol effective radius, the direction of the backscatter vector should be strongly related to changes in effective radius. A capability of important interest, especially in relation to homeland security, is the ability to differentiate two different aerosols. The channel wavelengths should be selected so that the backscatter vectors of the target aerosols are as close to orthogonal as possible. In general, lidars are designed as general multi-purpose instruments, meant to look at many different aerosols or an aerosol with unknown properties. The more wavelengths a lidar has, the more likely it is that the backscatter vectors of different aerosols will be close to orthogonal.

#### 6.4 Information Retrieval from Lidar Returns

Two methods have been presented in this dissertation for estimating aerosol concentration from measured lidar returns. Both of these methods were derived from an optimization perspective and approximate the target aerosol as a linear combination of basis aerosols. One of the these is an NLS estimator, which functions by representing the entire atmosphere

over the entire length of the measurement as a single state vector and then estimating the state vector by alternately linearizing and solving the lidar equation. The other algorithm is a form of the EKF, estimating the value of a much smaller state vector as a function of range. The EKF type is significantly more efficient than the NLS estimator.

Both of these operate along a single lidar measurement, however lidar data is often captured in the form of an image, with one axis corresponding to range and the other to measurement time. By applying either of these algorithms to a lidar image, image reconstruction and restoration are performed along the range axis of the image. Image quality could be further improved by performing image restoration along the time axis. Another Kalman filter could be applied to the time axis, using for the output of the first estimator as its input.

Depending on the intended application of a lidar instrument, it may be useful instead to develop efficient algorithms that treat the target aerosol as having a particle size distribution of known form but unknown parameters. Furthermore, an elastic lidar may be augmented with the addition of a Raman channel or a fluorescence channel. In this case, an algorithm should be formulated to take full advantage of the information contained in the inelastic channel.

## 6.5 Research Context

The goal of this research has been to expand understanding of aerosol emission processes from agricultural sources. In general, there is a lack of baseline data across the country on aerosol emission rates from agricultural operations. To this end, the Aglite lidar instrument was constructed and a suite of conventional point sensors was assembled especially for the purpose of gathering this data. Although elastic lidars have been previously applied to investigating agricultural aerosol emissions, the Aglite instrument system is a unique and useful addition to the very small field of research instruments, increasing the available capability of the scientific community to investigate aerosols using lidar. This research has described the construction, characteristics, and performance of this particular lidar instrument, with the hope that future aerosol lidars will improve upon the design decisions

made for Aglite.

Initial investigations with the Aglite lidar showed that conventional techniques for estimating aerosol concentration were inadequate, giving results that were unstable or had large error values. As a result, two new algorithms were developed for estimating aerosol concentration from elastic lidar data and demonstrated on measurements from real-world agricultural sources. These algorithms expand the choice of algorithms available to the aerosol lidar investigator and have useful advantages not available from other retrieval algorithms.

Furthermore, this research includes the pioneering work of the Aglite system to measure aerosol emission rates from agricultural facilities. The specific example of a dairy measurement campaign is the first time aerosol emission rates from a dairy were measured using a lidar. In addition to demonstrating the practicality of Aglite and its retrieval algorithm, this contributes additional data to the very small amount of available baseline data regarding dairy aerosol emissions. As illustrated by Table 5.3, there have been only four previous attempts to estimate the aerosol emission of dairies.

## 6.6 Future Work

Previous measurement campaigns by Aglite have all been “one-off” activities, a measurement event at a single location of duration never more than two weeks. In order to develop effective air-quality regulation or generalize scientific conclusions concerning any of these types of facilities, aerosol emission rates should be estimated for several different times of the year and over several different locations, and elastic lidar systems like Aglite are well suited to this task. Measurement sites should be selected that are broadly representative of the facility type and measurement campaigns should be conducted during different seasons, climate, and weather conditions.

For example, in order to determine the average aerosol emission rate of a generic dairy throughout the year, measurement campaigns should be conducted during all four seasons, under a variety of weather and temperature conditions. Dairies of different sizes and locations should be investigated in order to determine how factors such as facility size

and local climate affect the emission rate. The efficacy of conservation practices to mitigate aerosol emissions should be measured by comparing measurements taken at dairies that use different conservation practices. Effective government regulation of agricultural aerosol emissions will require knowledge of the average expected emission rate not only from dairies, but many other types of operations as well, of which a few examples are cattle feed-lots, soil tillage, crop harvest and processing.

To this end, there is a clear need to develop a simple, robust, and inexpensive methodology for estimating aerosol emissions and Aglite has proven that elastic lidar is a feasible technology for this task. Experience with Aglite has shown that a simpler and more durable lidar instrument would be needed for regularly monitoring facility compliance with aerosol emission regulations. Nevertheless, if a low-cost and durable aerosol elastic-lidar system were designed, then a number of capable and affordable lidar systems could be constructed for monitoring the effectiveness of conservation practices. Hopefully future investigators and lidars will follow in the footsteps of Aglite, improving on this research to cheaply and effectively measure aerosol emissions.

## Appendices

## Appendix A

### Construction of Lidar Equation Matrices

The function  $\hat{\mathbf{q}}(\mathbf{y})$  is defined by (3.16) and its component matrices can be expressed by (A.1) and (A.2).

$$\begin{aligned}
 A' &= \left[ \begin{array}{cccc} A'_1 & A'_2 & \cdots & A'_{\Lambda} \end{array} \right]^T \\
 A'_i &= -2 \left( Q \operatorname{diag} \left( \left[ \begin{array}{cccc} z_1 & z_2 & \cdots & z_L \end{array} \right] - z_m \right) \right) \otimes \mathbf{a}_i^T \\
 A &= \left[ \begin{array}{cccc} \mathbf{a}_1 & \mathbf{a}_2 & \cdots & \mathbf{a}_{\Lambda} \end{array} \right] \\
 Q &= \left[ \begin{array}{ccccccccc} 1 & 1 & \cdots & 1 & 0 & 0 & \cdots & 0 \\ 0 & 1 & & 1 & 0 & 0 & & \vdots \\ \vdots & & \ddots & & \vdots & & \ddots & \\ & & & & 1 & 0 & 0 & \\ & & & & 0 & 0 & 0 & \\ & & & & 0 & 0 & 1 & \\ & & & & \ddots & \vdots & \ddots & \vdots \\ \vdots & & & & 0 & 0 & 1 & 1 & 0 \\ 0 & \cdots & & 0 & 0 & 1 & \cdots & 1 & 1 \end{array} \right] \\
 \mathbf{a}_0 &= \left[ \begin{array}{cccc} \mathbf{a}_{0,1} & \mathbf{a}_{0,2} & \cdots & \mathbf{a}_{0,\Lambda} \end{array} \right]^T \\
 \mathbf{a}_{0,i} &= -2\alpha_{0,i} \left( \left[ \begin{array}{cccc} z_1 & z_2 & \cdots & z_L \end{array} \right] - z_m \right)
 \end{aligned} \tag{A.1}$$

$$\begin{aligned}
B' &= \begin{bmatrix} B'_1 & B'_2 & \cdots & B'_{\Lambda} \end{bmatrix}^T \\
B'_i &= (z_m^2 P_{m,i} / \beta_{m,i}) \operatorname{diag} \begin{bmatrix} \mathbf{b}_i^T / z_1^2 & \mathbf{b}_i^T / z_2^2 & \cdots & \mathbf{b}_i^T / z_L^2 \end{bmatrix} \\
B &= \begin{bmatrix} \mathbf{b}_1 & \mathbf{b}_2 & \cdots & \mathbf{b}_{\Lambda} \end{bmatrix}^T \\
\mathbf{b}_0 &= \begin{bmatrix} \mathbf{b}_{0,1} & \mathbf{b}_{0,2} & \cdots & \mathbf{b}_{0,\Lambda} \end{bmatrix}^T \\
\mathbf{b}_{0,i} &= (z_m^2 P_{m,i} \beta_{0,i} / \beta_{m,i}) \begin{bmatrix} z_1^{-2} & z_2^{-2} & \cdots & z_L^{-2} \end{bmatrix}^T \\
\hat{\mathbf{q}} &= \begin{bmatrix} P_{1,1} & P_{2,1} & \cdots & P_{L,1} & P_{1,2} & \cdots & P_{L,\Lambda} \end{bmatrix}^T \\
\hat{\mathbf{y}} &= \begin{bmatrix} n_{1,1} & n_{1,2} & \cdots & n_{1,S} & n_{2,1} & \cdots & n_{L,S} \end{bmatrix}^T
\end{aligned} \tag{A.2}$$

Matrices  $A'$  and  $B'$  are  $\Lambda L \times LS$ , vectors  $\mathbf{a}_0$  and  $\mathbf{b}_0$  are  $\Lambda L \times 1$ , matrices  $A'_i$  and  $B'_i$  are  $L \times LS$ , and the vectors  $\mathbf{a}_{0,i}$  and  $\mathbf{b}_{0,i}$  are  $L \times 1$ . The operator  $\otimes$  is the Kronecker product. The vector  $\mathbf{a}_{0,i}$  is a function of the expression  $a_{0,i}$ , the baseline extinction coefficient of the atmosphere at wavelength  $i$ . The vector  $\mathbf{b}_{0,i}$  is a function of  $\beta_{0,i}$ ,  $\beta_{m,i}$ , and  $P_{m,i}$ , which are the baseline backscatter coefficient, boundary point backscatter coefficient, and boundary point returned power respectively at wavelength  $i$ . The matrices  $A$  and  $B$  have been used previously in (3.7); their column vectors are defined as the extinction and backscatter vectors for each non-baseline aerosol component and can be calculated using Mie theory as described by (3.6).

A linear approximation of (3.16) around some point  $\mathbf{y}_0$  can be made by expanding it into a Taylor series and discarding all but the zero and first order terms. Consider the following Taylor series approximations of the expressions  $\mathbf{a} \cdot \exp(B\mathbf{x})$  and  $A\mathbf{x} \cdot \exp(B\mathbf{x})$  around the point  $\mathbf{x}_0$ .

$$\begin{aligned}
A\mathbf{x} \cdot \exp(B\mathbf{x}) &\approx \operatorname{diag} [\exp(B\mathbf{x}_0)] (A + \operatorname{diag}(A\mathbf{x}_0) B) \mathbf{x} \\
&\quad - \operatorname{diag} [\exp(B\mathbf{x}_0) \cdot A\mathbf{x}_0] B\mathbf{x}_0 \\
a \cdot \exp(B\mathbf{x}) &\approx \operatorname{diag}[a] \operatorname{diag} [\exp(B\mathbf{x}_0)] B\mathbf{x} \\
&\quad + \operatorname{diag}[a] \operatorname{diag} [\exp(B\mathbf{x}_0)] (1 - B\mathbf{x}_0)
\end{aligned} \tag{A.3}$$

One can rearrange (3.16) into a more convenient form and substitute the approximations given by (A.3) for the expressions  $\mathbf{b} \cdot \exp(A'\mathbf{y})$  and  $B'\mathbf{y} \cdot \exp(A'\mathbf{y})$ .

$$\begin{aligned}
\hat{\mathbf{q}} &= \text{diag}[\exp(\mathbf{d})] B' \hat{\mathbf{y}} \cdot \exp(A' \hat{\mathbf{y}}) + \text{diag}[\exp(\mathbf{d})] \mathbf{b} \cdot \exp(A' \hat{\mathbf{y}}) \\
\hat{\mathbf{q}} &\approx \text{diag}[\exp(\mathbf{d})] (\text{diag}[\exp(A \hat{\mathbf{y}}_0)] (B + \text{diag}(B \hat{\mathbf{y}}_0) A) \hat{\mathbf{y}} \\
&\quad - \text{diag}[\exp(A \hat{\mathbf{y}}_0) \cdot B \hat{\mathbf{y}}_0] A \hat{\mathbf{y}}_0) + \text{diag}[\exp(\mathbf{d})] (\text{diag}[\mathbf{b} \cdot \exp(A' \hat{\mathbf{y}}_0)] A' \hat{\mathbf{y}} \\
&\quad + \text{diag}[\mathbf{b} \cdot \exp(A' \hat{\mathbf{y}}_0)] (1 - A' \hat{\mathbf{y}}_0))
\end{aligned} \tag{A.4}$$

Combining terms in (A.4) and using the definitions given in (3.18) yields a linear approximation of the lidar equation.

## Appendix B

### Derivation of Covariance Matrices

If the observation noise is independent and zero-mean normally distributed, but the variance is range dependent, then the lidar equation can be written including a noise term.

$$\mathbf{p}(z)_{\text{meas}} = \mathbf{k} \cdot \mathbf{g}(z) \cdot \frac{\beta(z)}{z^2} \cdot \exp\left(-2 \int_0^z \boldsymbol{\alpha}(z'), dz'\right) + \boldsymbol{\nu}_z \quad \boldsymbol{\nu}_z \sim N(0, \Sigma_z) \quad (\text{B.1})$$

The expression  $\boldsymbol{\nu}_z$  is a zero-mean Gaussian distributed random noise vector [J] with covariance  $\Sigma_z$ . It is assumed that the elements of  $\boldsymbol{\nu}_z$  are uncorrelated, or in other words  $\Sigma_z$  is a diagonal matrix. In this case, noise at the reference point leads to error in estimating the lidar coefficient  $\mathbf{k}$ .

$$\mathbf{k} = \frac{(\mathbf{p}_m + \boldsymbol{\nu}_z) z_m^2}{\mathbf{g}_m \cdot \beta_m \cdot \exp\left[-2 \int_0^{z_m} \boldsymbol{\alpha}(z') dz'\right]} \quad (\text{B.2})$$

Disregarding the  $\mathbf{g}(z)$  and GFF, and applying the substitution of (B.2) into (B.1) yields a form of the lidar equation without the vector of calibration coefficients.

$$\mathbf{p}(z)_{\text{meas}} = (\mathbf{p} + \boldsymbol{\nu}_m) \cdot \frac{z_m^2 \beta(z)}{z^2 \beta_m} \cdot \exp\left(-2 \int_{z_m}^z \boldsymbol{\alpha}(z'), dz'\right) + \boldsymbol{\nu}_z \quad (\text{B.3})$$

From this it is apparent that in addition to the noise term that is independent with range, noise in the lidar coefficient estimation introduces a bias into the entire measurement. This bias can be minimized by choosing the reference point where the signal-to-noise ratio or  $P_m/\sigma_m$  is high. Care must be taken not to place the reference point in a part of the signal where the GFF is poorly known.

The form of the lidar equation found in (3.16) can be modified to show these noise terms as shown here.

$$\begin{aligned} \mathbf{q} &\approx (\text{diag}(\mathbf{d}_m) + I)(G\mathbf{y} + \mathbf{h}) + \boldsymbol{\nu}_B \\ \mathbf{d}_m &= \left[ \frac{\nu_{m,1}}{P_{m,1}} \mathbf{1}^T \quad \frac{\nu_{m,2}}{P_{m,2}} \mathbf{1}^T \quad \cdots \quad \frac{\nu_{m,\Lambda}}{P_{m,\Lambda}} \mathbf{1}^T \right]^T \\ \boldsymbol{\nu}_B &= \left[ \boldsymbol{\nu}_1 \quad \boldsymbol{\nu}_2 \quad \cdots \quad \boldsymbol{\nu}_\Lambda \right]^T \\ \boldsymbol{\nu}_i &= \left[ \nu_{1,i} \quad \nu_{2,i} \quad \cdots \quad \nu_{L,i} \right] \end{aligned} \quad (\text{B.4})$$

The matrix  $I$  is the identity matrix and the  $h$ th bin of the  $i$ th channel has observed signal variance  $[J^2]$  of  $\sigma_{h,i}^2$ . From here, it follows that the signal can be linearly approximated using (3.18).

$$\mathbf{q} \approx (\text{diag}(\mathbf{d}_m) + I)(G\mathbf{y} + \mathbf{h}) + \boldsymbol{\nu}_B \quad (\text{B.5})$$

In fact, if the lidar calibration coefficient is calculated using a given signal, the effect of the reference range noise is canceled by the lidar coefficient and the lidar solution at the reference range does not depend on either the bin noise or the lidar coefficient noise. If the lidar calibration coefficient is calculated separately from the current measurement, then this cancellation does not occur. The approximation (B.4) can be written as a linear equation plus two error terms, represented by the  $\boldsymbol{\nu}$  symbols covered by a brace.

$$\begin{aligned} \mathbf{q} &\approx G\mathbf{y} + \mathbf{h} + \overbrace{\boldsymbol{\nu}_m + \boldsymbol{\nu}_{yB}} \\ \boldsymbol{\nu}_m &= \text{diag}(\mathbf{d}_m)(G\mathbf{y} + \mathbf{h}) \end{aligned} \quad (\text{B.6})$$

If an estimate of  $\mathbf{y}$  exists, the entire term  $\text{diag}(\mathbf{d}_m)(G\mathbf{y} + \mathbf{h})$  can be approximated by the noise vector  $\boldsymbol{\nu}_m$ , which represents the error contribution at every range caused by noise in the lidar calibration coefficient. In order to compute the covariance of  $\mathbf{s}$ , and with a view to simplify the mathematics involved, let us approximate the term  $\boldsymbol{\nu}_m$ .

$$\boldsymbol{\nu}_m \approx \text{diag}(\mathbf{d}_m)\mathbf{h} \quad (\text{B.7})$$

By practical experiment, (B.7) is a reasonable approximation, taking into account that the expected value of  $\mathbf{y}$  is 0. Adding the two noise terms yields a zero-mean total-noise vector for each individual range.

$$\mathbf{s} = \boldsymbol{\nu}_m + \boldsymbol{\nu}_B \approx \text{diag}(\mathbf{d}_m) \mathbf{h} + \boldsymbol{\nu}_B \quad (\text{B.8})$$

The covariance of  $\mathbf{s}$  is given by (3.25).

## Appendix C

### Publication Release Forms



**RE: permission for dissertation**

Scott McNeill [scottm@spie.org]

**Sent:**Tuesday, October 26, 2010 9:18 AM

**To:** Christian Marchant

Dear Christian Marchant,

Thank you for seeking permission from SPIE to reprint an article from our publications. As an author of the paper, you retain co-owner rights to the material contained therein. Publisher's permission is hereby granted under the following conditions: (1) the material to be used has appeared in our publication without credit or acknowledgment to another source; and (2) you credit the original SPIE publication. Include the authors' names, title of paper, volume title, SPIE volume number, and year of publication in your credit statement.

Sincerely,

Mr. Scott McNeill for  
 Eric Pepper, Director of Publications  
 SPIE  
 P.O. Box 10, Bellingham WA 98227-0010 USA  
 360/676-3290 (Pacific Time) eric@spie.org

-----Original Message-----

**From:** Christian Marchant [<mailto:Christian.Marchant@energydynamicslab.com>]  
**Sent:** Friday, October 22, 2010 11:13 AM  
**To:** reprint\_permission  
**Subject:** permission for dissertation

To Permissions Editor:

I am preparing my dissertation in the Department of Electrical and Computer Engineering at Utah State University. I hope to complete my degree in the fall of this year (2010).

An article

C. C. Marchant, T. D. Wilkerson, G. E. Bingham, V. V. Zavyalov, J. M. Andersen, C. B. Wright, S. S. Cornelisen, R. S. Martin, P. J. Silva, and J. L. Hatfield "Aglite Lidar: A Portable Elastic Lidar System for Investigating Aerosol and Wind Motions at or around Agricultural Production Facilities," *J. Appl. Remote Sens.*, vol. 3, 033511, 2009.

of which I am first author, and which appeared in your journal, reports an essential part of my dissertation research. I would like permission to reprint it as a chapter in my dissertation. (Repinting the chapter may necessitate some revision.) Please note that USU sends dissertations to Bell & Howell Dissertation Services to be made available for reproduction.

I will include an acknowledgement to the article on the first page of the chapter, as shown below. Copyright and permission information will be included in a special appendix. If you would like a different acknowledgement, please so indicate.

"Reproduced by permission of SPIE Journal of Applied Remote Sensing, vol. 3, C. C. Marchant, T. D. Wilkerson, G. E. Bingham, V. V. Zavyalov, J. M. Andersen, C. B. Wright, S. S. Cornelisen, R. S. Martin, P. J. Silva, and J. L. Hatfield as: Aglite Lidar: A Portable Elastic Lidar System for Investigating Aerosol and Wind Motions at or around Agricultural Production Facilities, 033511 , 2009. with permission from SPIE"

**Re: permission for dissertation**

j.hansson@ieee.org

Sent: Friday, October 29, 2010 11:26 AM

To: Christian Marchant

Comments/Response to Case ID: 0062D4F0

ReplyTo: Copyrights@ieee.org

From: Jacqueline Hansson

Date: 10/29/2010

Subject: Re: permission for  
dissertation

Send To: Christian Marchant  
<Christian.Marchant@energydynamicslab.com>

cc:

Dear Christian Marchant:

We are happy to grant you this permission to reprint your below described IEEE copyrighted papers in your thesis and, if you wish, have your thesis placed on your university's website. We have only two requirements that must be satisfied before we can consider this permission final:

(1) The following copyright/credit notice must appear prominently either on the first page of the reprinted material or prominently in the references of the reprinted paper, with the appropriate details filled in: © [year] IEEE. Reprinted, with permission, from [IEEE publication title, paper title, and author names].

(2) Additionally, if your thesis is to appear on the university's website, the following message should be displayed either at the beginning of the credits or in an appropriate and prominent place on the website: This material is posted here with permission of the IEEE. Such permission of the IEEE does not in any way imply IEEE endorsement of any of Utah State University.'s products or services. Internal or personal use of this material is permitted. However, permission to reprint/republish this material for advertising or promotional purposes or for creating new collective works for resale or redistribution must be obtained from the IEEE by writing to pubs-permissions@ieee.org. By choosing to view this material, you agree to all provisions of the copyright laws protecting it.

USU may also send yours dissertations to Bell & Howell Dissertation Services to be made available for reproduction.

Sincerely,

Jacqueline Hansson

© © © © © © © © © © ©  
IEEE Intellectual Property Rights Office  
445 Hoes Lane  
Piscataway, NJ 08855-1331 USA  
+1 732 562 3966 (phone)  
+1 732 562 1746 (fax)

IEEE-- Fostering technological innovation  
and excellence for the benefit of humanity.  
© © © © © © © © © © ©

October 22, 2010

Christian Marchant  
1106 E Stadium Dr  
Logan, UT 84341  
(435) 213-2241  
chris@vitba.org

Thomas Wilkerson  
1695 N Research Park Way  
North Logan, UT 84341

Dear Dr. Wilkerson:

I am preparing my dissertation in the Department of Electrical and Computer Engineering at Utah State University. I hope to complete my degree in the fall of this year (2010).

I am requesting your permission to include the attached material as shown, titled "Aglite Lidar: A Portable Elastic Lidar System for Investigating Aerosol and Wind Motions at or around Agricultural Production Facilities," of which you are an author. I will include acknowledgements to your work.

Additionally, I am requesting your affirmation that I was the majority contributing author for this paper, as this is a requirement of Utah State University for the inclusion of this paper in my dissertation.

Please indicate your approval of this request by signing in the space provided. If you have any questions, please call me at the number above.

Thank you for your cooperation,

Christian Marchant

I hereby give permission to Christian Marchant to use the article shown below, of which I am a co-author, in his dissertation as he sees fit.

C. C. Marchant, T. D. Wilkerson, G. E. Bingham, V. V. Zavyalov, J. M. Andersen, C. B. Wright, S. S. Cornelsen, R. S. Martin, P. J. Silva, and J. L. Hatfield "Aglite Lidar: A Portable Elastic Lidar System for Investigating Aerosol and Wind Motions at or around Agricultural Production Facilities," *J. Appl. Remote Sens.*, vol. 3, 033511, 2009.

I furthermore affirm that Christian Marchant was the majority contributing author of this paper.

Signed T. D. Wilkerson

Thomas Wilkerson, Ph.D.

Date 10/26/2010

**Re: dissertation permission**

Jan Marie Andersen [janmarie@gmail.com]

Sent: Tuesday, October 26, 2010 5:50 PM

To: Christian Marchant

Chris,

Good to hear from you! Congratulations on finishing up your dissertation! Here's the legal stuff:

I hereby give permission to Christian Marchant to use the article shown below, of which I am a co-author, in his dissertation as he sees fit.

C. C. Marchant, T. D. Wilkerson, G. E. Bingham, V. V. Zavyalov, J. M. Andersen, C.  
B. Wright, S. S. Cornelsen, R. S. Martin, P. J. Silva, and J. L. Hatfield "Aglite Lidar: A Portable Elastic Lidar System for Investigating Aerosol and Wind Motions at or around Agricultural Production Facilities," *J. Appl. Remote Sens.*, vol. 3, 033511, 2009.

I furthermore affirm that Christian Marchant was the majority contributing author of this paper.

Sincerely,  
Jan Marie

---

Jan Marie Andersen  
Institute for Astrophysical Research  
Boston University  
725 Commonwealth Ave, CAS 508  
Boston, MA 02215

---

<http://people.bu.edu/janmarie/>  
janmarie@bu.edu

---

October 22, 2010

Christian Merchant  
1106 E Stadium Dr  
Logan, UT 84341  
(435) 213-2241  
chris@vitba.org

Scott Cornelsen  
588 W 1330 N  
Logan, UT 84341

Dear Mr. Cornelsen:

I am preparing my dissertation in the Department of Electrical and Computer Engineering at Utah State University. I hope to complete my degree in the fall of this year (2010).

I am requesting your permission to include the attached material as shown, titled "Aglite Lidar: A Portable Elastic Lidar System for Investigating Aerosol and Wind Motions at or around Agricultural Production Facilities," of which you are an author. I will include acknowledgements to your work.

Additionally, I am requesting your affirmation that I was the majority contributing author for this paper, as this is a requirement of Utah State University for the inclusion of this paper in my dissertation.

Please indicate your approval of this request by signing in the space provided. If you have any questions, please call me at the number above.

Thank you for your cooperation,

Christian Merchant

I hereby give permission to Christian Merchant to use the article shown below, of which I am a co-author, in his dissertation as he sees fit.

C. C. Marchant, T. D. Wilkerson, G. E. Bingham, V. V. Zavyalov, J. M. Andersen, C. B. Wright, S. S. Cornelsen, R. S. Martin, P. J. Silva, and J. L. Hatfield "Aglite Lidar: A Portable Elastic Lidar System for Investigating Aerosol and Wind Motions at or around Agricultural Production Facilities," *J. Appl. Remote Sens.*, vol. 3, 033511, 2009.

I furthermore affirm that Christian Merchant was the majority contributing author of this paper.

Signed \_\_\_\_\_

Scott Cornelsen

Date 10-22-10

October 22, 2010

Christian Merchant  
1106 E Stadium Dr  
Logan, UT 84341  
(435) 213-2241  
chris@vitba.org

Dr. Randal Martin  
ENGR 219, Utah State University

Dear Dr. Martin:

I am preparing my dissertation in the Department of Electrical and Computer Engineering at Utah State University. I hope to complete my degree in the fall of this year (2010).

I am requesting your permission to include the attached material as shown, titled "Aglite Lidar: A Portable Elastic Lidar System for Investigating Aerosol and Wind Motions at or around Agricultural Production Facilities" and "Estimation of Dairy Particulate Matter Emission Rates by Lidar and Inverse Modeling" of which you are an author. I will include acknowledgements to your work.

Additionally, I am requesting your affirmation that I was the majority contributing author for this paper, as this is a requirement of Utah State University for the inclusion of this paper in my dissertation.

Please indicate your approval of this request by signing in the space provided. If you have any questions, please call me at the number above.

Thank you for your cooperation,

Christian Merchant

I hereby give permission to Christian Merchant to use the articles shown below, of which I am a co-author, in his dissertation as he sees fit.

C. C. Marchant, T. D. Wilkerson, G. E. Bingham, V. V. Zavyalov, J. M. Andersen, C. B. Wright, S. S. Cornelsen, R. S. Martin, P. J. Silva, and J. L. Hatfield, "Aglite Lidar: A Portable Elastic Lidar System for Investigating Aerosol and Wind Motions at or around Agricultural Production Facilities," *J. Appl. Remote Sens.*, vol. 3, 033511, 2009.

C. C. Marchant, K. D. Moore, M. D. Wojcik, R. S. Martin, J. L. Hatfield, J. H. Prueger, and R. L. Pfeiffer, "Estimation of Dairy Particulate Matter Emission Rates by Lidar and Inverse Modeling," *Trans. ASAE*, submitted for publication.

I furthermore affirm that Christian Merchant was the majority contributing author of these papers.

Signed Randal A. Martin

Dr. Randal Martin, Ph.D.

Date 11-5-10

**RE: reprint permission**

Silva, Philip J. [Phil.Silva@ARS.USDA.GOV]

**Sent:** Friday, October 22, 2010 1:57 PM

**To:** Christian Marchant

I hereby give permission to Christian Marchant to use the article shown below, of which I am a co-author, in his dissertation as he sees fit.

C. C. Marchant, T. D. Wilkerson, G. E. Bingham, V. V. Zavyalov, J. M. Andersen, C. B. Wright, S. S. Cornelisen, R. S. Martin, P. J. Silva, and J. L. Hatfield "Aglite Lidar: A Portable Elastic Lidar System for Investigating Aerosol and Wind Motions at or around Agricultural Production Facilities," *J. Appl. Remote Sens.*, vol. 3, 033511, 2009.

I furthermore affirm that Christian Marchant was the majority contributing author of this paper.

Philip J. Silva, Ph.D.  
10/22/2010

--  
Philip J. Silva, Environmental Chemist  
USDA-ARS  
230 Bennett Lane  
Bowling Green, KY 42104  
(270) 781-2260 x246  
(270) 781-7994 (fax)  
phil.silva@ars.usda.gov

October 25, 2010

Christian Merchant  
1106 E Stadium Dr  
Logan, UT 84341  
(435) 213-2241  
chris@vitba.org

Dr. Jerry L. Hatfield  
2110 University Boulevard NLAE  
Ames, IA 50011-3120

Dear Dr. Hatfield:

I am preparing my dissertation in the Department of Electrical and Computer Engineering at Utah State University. I hope to complete my degree in the fall of this year (2010).

I am requesting your permission to include the attached material as shown, titled "Aglite Lidar: A Portable Elastic Lidar System for Investigating Aerosol and Wind Motions at or around Agricultural Production Facilities" and "Estimation of Dairy Particulate Matter Emission Rates by Lidar and Inverse Modeling" of which you are an author. I will include acknowledgements to your work.

Additionally, I am requesting your affirmation that I was the majority contributing author for this paper, as this is a requirement of Utah State University for the inclusion of this paper in my dissertation. Please indicate your approval of this request by signing in the space provided. If you have any questions, please call me at the number above.

Thank you for your cooperation,

Christian Merchant

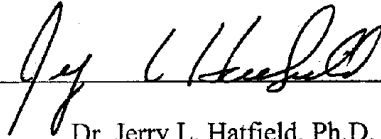
I hereby give permission to Christian Merchant to use the articles shown below, of which I am a co-author, in his dissertation as he sees fit.

C. C. Marchant, T. D. Wilkerson, G. E. Bingham, V. V. Zavyalov, J. M. Andersen, C. B. Wright, S. S. Cornelsen, R. S. Martin, P. J. Silva, and J. L. Hatfield, "Aglite Lidar: A Portable Elastic Lidar System for Investigating Aerosol and Wind Motions at or around Agricultural Production Facilities," *J. Appl. Remote Sens.*, vol. 3, 033511, 2009.

C. C. Marchant, K. D. Moore, M. D. Wojcik, R. S. Martin, J. L. Hatfield, J. H. Prueger, and R. L. Pfeiffer, "Estimation of Dairy Particulate Matter Emission Rates by Lidar and Inverse Modeling," *Trans. ASAE*, submitted for publication.

I furthermore affirm that Christian Merchant was the majority contributing author of these papers.

Signed



Dr. Jerry L. Hatfield, Ph.D.

Date 25-Oct-2010

October 22, 2010

Christian Merchant  
1106 E Stadium Dr  
Logan, UT 84341  
(435) 213-2241  
chris@vitba.org

Michael Wojcik  
1695 N Research Park Way  
North Logan, UT 84341

Dear Dr Wojcik:

I am preparing my dissertation in the Department of Electrical and Computer Engineering at Utah State University. I hope to complete my degree in the fall of this year (2010).

I am requesting your permission to include the attached material as shown, titled "Estimation of Aerosol Effective Radius by Multi-Wavelength Elastic Lidar" and "Estimation of Dairy Particulate Matter Emission Rates by Lidar and Inverse Modeling," of which you are an author. I will include acknowledgements to your work.

Additionally, I am requesting your affirmation that I was the majority contributing author for these papers, as this is a requirement of Utah State University for the inclusion of these papers in my dissertation. Please indicate your approval of this request by signing in the space provided. If you have any questions, please call me at the number above.

Thank you for your cooperation,

Christian Merchant

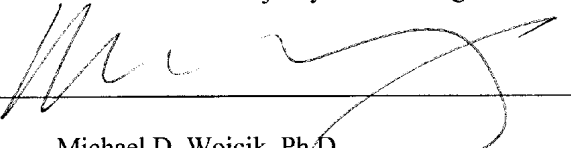
I hereby give permission to Christian Merchant to use the article shown below, of which I am a co-author, in his dissertation as he sees fit.

C. C. Marchant, M. D. Wojcik, and W. J. Bradford "An Iterative Least Squares Approach to Elastic-Lidar Retrievals for Well-Characterized Aerosols", *IEEE Trans. Geosci. Remote Sens.*, vol. 42, pp. 443-456, 2004.

C. C. Marchant, K. D. Moore, M. D. Wojcik, R. S. Martin, J. L. Hatfield, J. H. Prueger, and R. L. Pfeiffer, "Estimation of Dairy Particulate Matter Emission Rates by Lidar and Inverse Modeling," *Trans. ASAE*, submitted for publication.

I furthermore affirm that Christian Merchant was the majority contributing author of these papers.

Signed



Michael D. Wojcik, Ph.D.

Date 26 Oct - zero

October 22, 2010

Christian Merchant  
1106 E Stadium Dr  
Logan, UT 84341  
(435) 213-2241  
[chris@vitba.org](mailto:chris@vitba.org)

William Bradford  
1695 N Research Park Way  
North Logan, UT 84341

Dear Mr. Bradford:

I am preparing my dissertation in the Department of Electrical and Computer Engineering at Utah State University. I hope to complete my degree in the fall of this year (2010).

I am requesting your permission to include the attached material as shown, titled "Estimation of Aerosol Effective Radius by Multi-Wavelength Elastic Lidar," of which you are an author. I will include acknowledgements to your work.

Additionally, I am requesting your affirmation that I was the majority contributing author for this paper, as this is a requirement of Utah State University for the inclusion of this paper in my dissertation.

Please indicate your approval of this request by signing in the space provided. If you have any questions, please call me at the number above.

Thank you for your cooperation,

Christian Merchant

I hereby give permission to Christian Merchant to use the article shown below, of which I am a co-author, in his dissertation as he sees fit.

C. C. Marchant, M. D. Wojcik, and W. J. Bradford "An Iterative Least Squares Approach to Elastic-Lidar Retrievals for Well-Characterized Aerosols", *IEEE Trans. Geosci. Remote Sens.*, vol. 42, pp. 443-456, 2004.

I furthermore affirm that Christian Merchant was the majority contributing author of this paper.

Signed William J. Bradford

William J. Bradford

Date Nov. 3, 2010

October 25, 2010

Christian Marchant  
1106 E Stadium Dr  
Logan, UT 84341  
(435) 213-2241  
[chris@vitba.org](mailto:chris@vitba.org)

Dr. Richard L. Pfeiffer  
2110 University Boulevard NLAE  
Ames, IA 50011-3120

Dear Dr. Pfeiffer:

I am preparing my dissertation in the Department of Electrical and Computer Engineering at Utah State University. I hope to complete my degree in the fall of this year (2010).

I am requesting your permission to include the attached material as shown, titled "Estimation of Dairy Particulate Matter Emission Rates by Lidar and Inverse Modeling," of which you are an author. I will include acknowledgements to your work.

Additionally, I am requesting your affirmation that I was the majority contributing author for this paper, as this is a requirement of Utah State University for the inclusion of this paper in my dissertation. Please indicate your approval of this request by signing in the space provided. If you have any questions, please call me at the number above.

Thank you for your cooperation,

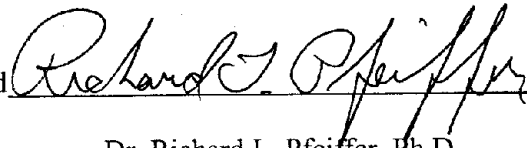
Christian Marchant

---

I hereby give permission to Christian Marchant to use the article shown below, of which I am a co-author, in his dissertation as he sees fit.

C. C. Marchant, K. D. Moore, M. D. Wojcik, R. S. Martin, J. L. Hatfield, J. H. Prueger, and R. L. Pfeiffer, "Estimation of Dairy Particulate Matter Emission Rates by Lidar and Inverse Modeling," *Trans. ASAE*, submitted for publication.

I furthermore affirm that Christian Marchant was the majority contributing author of this paper.

Signed 

Dr. Richard L. Pfeiffer, Ph.D.

Date 10/25/10

October 23, 2010

Christian Marchant  
1106 E Stadium Dr  
Logan, UT 84341  
(435) 213-2241  
[chris@vitba.org](mailto:chris@vitba.org)

Dr. John H. Prueger  
2110 University Boulevard NLAE  
Ames, IA 50011-3120

Dear Dr. Prueger:

I am preparing my dissertation in the Department of Electrical and Computer Engineering at Utah State University. I hope to complete my degree in the fall of this year (2010).

I am requesting your permission to include the attached material as shown, titled "Estimation of Dairy Particulate Matter Emission Rates by Lidar and Inverse Modeling" of which you are an author. I will include acknowledgements to your work.

Additionally, I am requesting your affirmation that I was the majority contributing author for this paper, as this is a requirement of Utah State University for the inclusion of this paper in my dissertation. Please indicate your approval of this request by signing in the space provided. If you have any questions, please call me at the number above.

Thank you for your cooperation,

Christian Marchant

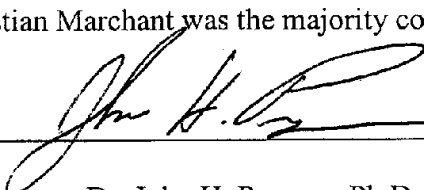
---

I hereby give permission to Christian Marchant to use the article shown below, of which I am a co-author, in his dissertation as he sees fit.

C. C. Marchant, K. D. Moore, M. D. Wojcik, R. S. Martin, J. L. Hatfield, J. H. Prueger, and R. L. Pfeiffer, "Estimation of Dairy Particulate Matter Emission Rates by Lidar and Inverse Modeling," *Trans. ASAE*, submitted for publication.

I furthermore affirm that Christian Marchant was the majority contributing author of this paper.

Signed

  
Dr. John H. Prueger, Ph.D.

Date 10/23/10

## Vita

Christian C. Marchant

### **Education**

BS in Electrical Engineering, Brigham Young University, Provo, Utah. (5/04) GPA: 3.6 (4.0=A) Recipient of Engineering Academic Scholarship (Micron Scholarship) and Office of Research and Creative Activities Scholarship. MS in Electrical Engineering, Utah State University, Logan, Utah. (4/08) GPA: 3.4. PhD in Electrical Engineering, Utah State University, Logan, Utah. (12/10) GPA: 3.9.

### **Experience**

GRADUATE RESEARCH ASSISTANT, Energy Dynamics Laboratory, Logan, Utah (9/04-Present).

SPACE SCHOLAR INTERN, USAF Research Lab, Space Vehicles Directorate, Kirtland Air Force Base, New Mexico (05/09-08/09).

### **Published Journal Articles**

- Aglite Lidar: A Portable Elastic Lidar System for Investigating Aerosol and Wind Motions at or around Agricultural Production Facilities, C. C. Marchant et al., *Journal of Applied Remote Sensing*, vol. 3, 033511, 2009.
- An Iterative Least Square Approach to Elastic-Lidar Retrievals for Well-Characterized Aerosols, C. C. Marchant et al., *IEEE Trans. Geosci. Remote Sens.*, vol. 48, pp. 2430-2444, 2010.